High Harmonic Generation With Focal Cone Geometry

by

John Matthew Gjevre

A thesis submitted in partial fulfillment of the requirements for the degree of

Master of Science

in

Photonics and Plasmas

Department of Electrical and Computer Engineering
University of Alberta

Abstract

High Harmonic Generation (HHG) is a convenient method of producing coherent extreme ultraviolet (XUV) radiation and is typically produced by focusing a laser onto a gas jet. The total intensity of XUV generated in this method is limited by the ionization threshold of the gas and absorption of XUV radiation in the gas. A new geometry of Focal Cone High Harmonic Generation (FCHHG) is examined. This geometry involves focusing the incoming cone of light through a gas sheet rather than placing a gas jet at laser focus. Such a focusing geometry generates a converging cone of XUV radiation producing a high intensity high harmonic hot spot (HHHS) at focus. Using 100 TW to 1 PW laser pulses, high energy, microjoule to millijoule, coherent XUV pulses should be achievable. An experiment to test this concept was carried out at the Centro de Láseres Pulsados (CLPU) in Salamanca Spain. For this a gas nozzle was designed to produce a rectangular gas sheet capable of providing a uniform density region over which the laser can interact. A number of diagnostics were used to characterize the XUV beam both spectrally and spatially. These included an Xray CCD camera and XUV photodiodes to observe the XUV and measure its intensity, spectral measurements using a transmission grating and knife edge diffraction, and divergence measurements using the knife edge and shadowgraphic imaging of perforated meshes. The conversion efficiency as a function of backing pressure, nozzle distance from laser focus and the laser axis, and intensity is also explored.

Acknowledgements

I would like to express my gratitude towards my supervisors Drs. Ying and Fedosejevs for their support and guidance through the course of my studies.

I would like to thank the staff of the Centro de Láseres Pulsados facility for their work during our experimental campaign at their facility, in particular Carlos Salgado-López for providing some of the interferometry data in this thesis.

I would like to thank Channprit Kaur, Talwinder Kaur Sraw, Nicholas Beier and the other members of our laser group for their assistance in my research and advice and feedback.

Table of Contents

List of Figures

List of Abbreviations

- HHG - High Harmonic Generation
- FCHHG - Focal Cone High Harmonic Generation
- HHHS - High Harmonic Hot Spot
- XUV - Extreme Ultraviolet
- TW - Terawatt
- CLPU - Centro de Láseres Pulsados
- FEL - Free Electron Laser
- STP - Standard Temperature and Pressure

Chapter 1

Introduction

Ultraviolet light is the part of the optical spectrum lying between visible light (380-700 nm) and x-rays (0.01-10nm). Most daily interactions with UV light are from the Sun which emits about 10% of its light in the ultraviolet. Short wavelength ultraviolet is absorbed by the atmosphere although longer wavelengths are able to pass through and are responsible for suntanning and sunburns. As light sources such as lasers, synchrotrons, and free electron lasers have developed, a demand for short wavelength light sources has grown. For tasks such as imaging [1-3] and lithography [4-5] these short wavelengths are particularly useful due to their ability to interact with targets over small spatial scales. This allows for imaging of nanometer-sized targets and smaller lithograph marks to be made which is very useful in microchip manufacturing. In particular the spectrum of light known as extreme ultraviolet (XUV), usually defined as having wavelengths between 10 and 121 nm, is useful in this regard.

XUV, like any other type of light, can be coherent or incoherent. The simplest way to produce incoherent XUV is to ionize a sample into a hot plasma so that it releases electrons with binding energies within the XUV regime. The electrons then recombine with the atom resulting in the release of photons with energy equal to the binding energy. This is often what is used for XUV lithography. Coherent XUV is much more useful for the purposes of imaging and can be produced through synchrotron radiation generated either by undulators in synchrotrons or by free electron lasers (FEL). It can also be produced through the process of high harmonic generation (HHG).

While synchrotrons and FELs are very useful for a variety of different purposes, they are quite expensive and require large facilities in order to operate. High harmonic generation on the other hand can be produced by relatively inexpensive lasers which makes it the preferred method for many XUV applications. High harmonic generation occurs when a sufficiently intense laser is focused through a medium (typically gas or plasma but recent research has also revealed this process occuring in solids [6-7]), interacting with it in such a way that some of the laser light is converted into high order harmonics of the driving

laser frequency. Given the correct conditions these high order harmonics can extend deep into the XUV (this will be explained more thoroughly in a later chapter). There is a downside however, the efficiency at which the laser light is converted into harmonics is very low. Additionally, HHG has to be done with laser intensities only a little below the level for ionizing the medium. If the medium is ionized, harmonics can still be generated but the conversion efficiency is decreased even further.

Since the discovery of the HHG process in the 1980's much work has been done to improve different aspects of this XUV source. [8] A particularly useful property of HHG is its capability to generate attosecond duration pulses thereby forming the basis for modern ultrafast science. Other research is done to reach ever higher order harmonics in order to obtain easily accessible coherent light sources at shorter wavelengths. Of particular interest are wavelengths between 4.37 nm and 2.33 nm as these are between the K absorption edges of carbon and oxygen respectively. This range of wavelengths is known as the water window where carbon absorbs more efficiently than water allowing for high contrast imaging of biological specimens. [9,10] In general it is desirable to determine a way to increase pulse output energies and, in fact, this is the main focus of our research.

Recent research [11] shows that conversion efficiencies from laser energy to XUV energy on the order of 10^{-3} are possible to achieve. In contrast, typical HHG conversion efficiencies are on the order of $10^{-8} - 10^{-5}$. These very high conversion efficiencies were achieved by using a dual gas jet system and fine tuning the length of the gas medium as well as the pressure. This result seems to mark the current upper limit for increasing conversion efficiency. However, by changing the geometry of the system in conjunction with utilizing these optimizing techniques it may be possible to increase the number of XUV photons generated even if conversion efficiency is not improved. To do this a focal cone high harmonic generation (FCHHG) technique is employed.

The focal cone technique is very straightforward. Typical HHG is performed by placing a gas jet at, or very close to, laser focus as seen in figure 1.1. FCHHG differs in that the gas jet is placed upstream from laser focus as seen in figure 1.2. By doing this the laser has a larger region of gas with which to interact. Naturally a higher energy laser pulse is required in order to achieve HHG here, but there will be overall a larger amount of high harmonics generated. In addition to this, the focusing aspect of the incoming laser pulse should be carried over to the HHG. This means that all the HHG created in this large region will be focused down into a high harmonic hot spot (HHHS) at laser focus with an intensity of XUV light far higher than what could be produced by simply placing the gas jet at laser focus.

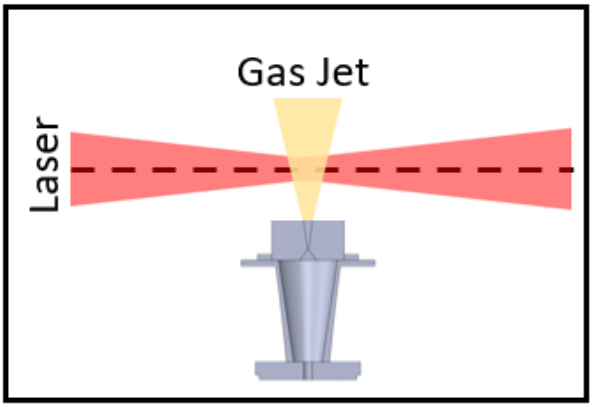

Figure 1.1: The traditional HHG technique of placing the gas jet at laser focus

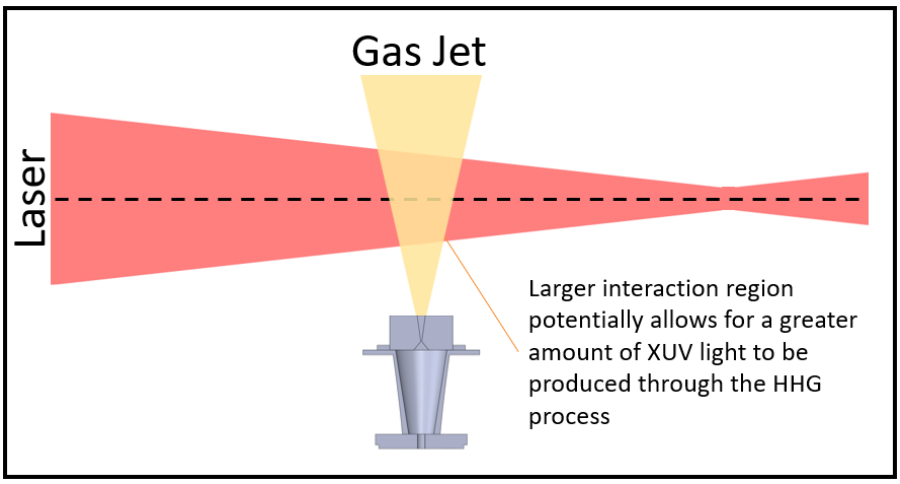

Figure 1.2: The focal cone high harmonic generation geometry where the gas jet is placed upstream from laser focus

In the present work this focal cone geometry is explored through an experiment conducted at the Centro De Láseres Pulsados (CLPU) in Salamanca, Spain. Chapter 2 introduces some of the relevant background theory of HHG and nozzle design. Chapter 3 discusses the gas jet design and verification for the experiment, and chapter 4 provides a detailed analysis of data conducted during the experiment at the CLPU. The spectral and spatial properties of the resulting data are examined to determine if HHG has been produced and determine whether it is focusing as expected. In chapter 5 conclusions from the experiment are discussed as well as future work that needs to be conducted to improve this technique.

Chapter 2

Background

2.1 High Harmonic Generation - Overview

High harmonic generation (HHG) is a process by which a laser passing through a medium can interact with the medium in such a way as to create high-order harmonics of its frequency.

2.1.1 Perturbative Non-Linear Optics

High harmonic generation is similar in concept to the more familiar second harmonic generation, a perturbative non-linear optical process (a process wherein the electric susceptibility and resulting properties vary with the strength of the electric field of the light moving through it) capable of transforming two photons of frequency ω into one photon of frequency 2ω. Second harmonic generation is typically done by passing light through certain types of crystals which respond in a non-linear manner leading to the generation of photons with frequency 2ω. For low intensity light the non-linear effects of these crystals are negligible, but lasers can be intense enough for the process to occur. [12] For a normal isotropic material with a linear response to the intensity of light the polarization density of the material is given by the equation 2.1.

$$P = \epsilon_0 \chi E \tag{2.1}$$

This is the full equation for polarization of the linear isotropic media, it can be seen that it depends linearly on the electric field of the laser E and the susceptibility χ. When considering a nonlinear material the polarization will take into account higher order terms and anisotropic susceptibility (susceptibility varying in different directions). The ith component of the polarization vector is expressed as a power series dependent on the electric field as shown in equation 2.2. This equation displays how the media is behaving in a nonlinear manner with respect to the electric field. The first order term

will dominate, however, and the effects from higher order terms will be small compared to it. The susceptibility tensors $\chi^1, \chi^2, ...$ determine how dependent the polarization is on each term of the power series. [12]

$$P_i = \epsilon_0 \chi^1_{ij} E_j + \epsilon_0 \chi^2_{ijk} E_j E_k + \epsilon_0 \chi^3_{ijkl} E_j E_k E_l + ... \tag{2.2}$$

Second harmonic generation makes use of the second order term of the nonlinear polarization: $P_i = \epsilon_0 \chi^2_{ijk} E_j E_k$ to create a photon with twice the frequency of the two photons needed to create it. Similarly, higher order terms in the polarization power series can create third, fourth, fifth, etc. harmonic generation. Third harmonic generation is governed by the third order term of the nonlinear polarization: $P_i = \epsilon_0 \chi^3_{ijkl} E_j E_k E_l$. For third harmonic generation within an isotropic medium, driven by a laser with an electric field given by $E(t) = Ecos(\omega t)$, the time dependent polarization is represented by equation 2.3. [12,13]

$$P(t) = \epsilon_0 \chi^3 Ecos(\omega t) Ecos(\omega t) Ecos(\omega t) = \epsilon_0 \chi^3 E^3 (\frac{1}{4} cos(3\omega t) + \frac{3}{4} cos(\omega t)) \tag{2.3}$$

As the harmonics increase, higher order polarization terms will be used. However, this process operates in a perturbative regime. This means that the first order will be the largest term, the second order smaller, the third order smaller than the second, and so on. As such the intensity of higher order harmonics rapidly decline, with most practical uses being relegated to the second or third harmonics before the intensity becomes too low to be used. [12,13]

2.1.2 High Harmonic Generation - Three Step Model

While there are similarities between HHG and SHG they both act on somewhat different principles. In the second harmonic regime the energy of the emitted photon is much less than the ionization potential of the atom. Therefore, the two photons which the atom absorbs will not ionize an electron but merely raise it to a virtual state before it falls back into its original position releasing a single photon with twice the frequency of the original photons. In HHG however the emitted photon has energy greater than or equal to the ionization potential therefore requiring that the electron leaves the atom in order to generate this photon.

High harmonic generation is also a non-perturbative process. At first the intensity of harmonics will rapidly fall off as might be expected from a perturbative process. At a certain point however, the harmonics will form a plateau where each of the harmonics is of similar intensity. This plateau will carry on until it reaches the cutoff energy determined

by the maximum energy of equation 2.4 as seen in figure 2.1 [15]. This can allow for photons hundreds of times more energetic than the starting light to be created.

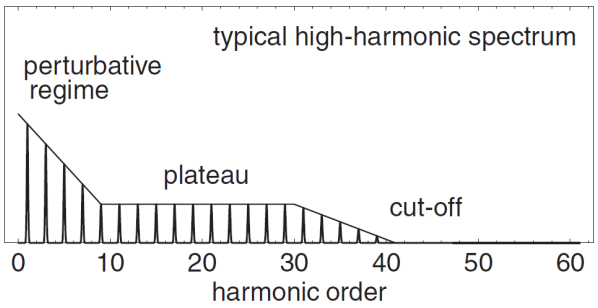

Figure 2.1: HHG Perturbative Regime, Plateau, and Cuttoff Region. Images used with permission from APS. [15]

The Single Atom Response

High harmonic generation can be modeled with a simple three step model shown in figure 2.2 [8]. These steps are i) Tunnel Ionization, ii) Free Acceleration, iii) Recollision. At the start the electron is held within the potential well of an atom. When a strong electric field from a laser propagates past the electron the potential well of the atom will become distorted. Close to the peak of the electric field the potential well will become low enough that the electron can escape through one side of it through quantum tunneling. After this has occurred the electron is free and within the laser field so it will be rapidly accelerated away from the atom. However, the electric field is oscillating and will oscillate faster than the time it takes for the electron to completely escape. As such the field will reverse itself and the force acting upon the electron will start to go in the opposite direction, back towards the atom. At this point the electron will fall back into the potential well and recollide with the atom releasing a photon in the process. The entire motion of the electron can be modeled using a simple classical mechanics model allowing for the maximum photon energy to be found in equation 2.4. This maximum energy is determined by the ionization potential of the atom (I_p) as well as the pondermotive energy of the electron accelerated in the laser's electric field (U_p) given by equation 2.5. This is equation is dependent on the charge of the electron e, the mass of the electron m, the magnitude of the electric field of the laser E, and the frequency of the laser ω. This is also proportional to the intensity of laser I multiplied by the square of the laser wavelength λ.

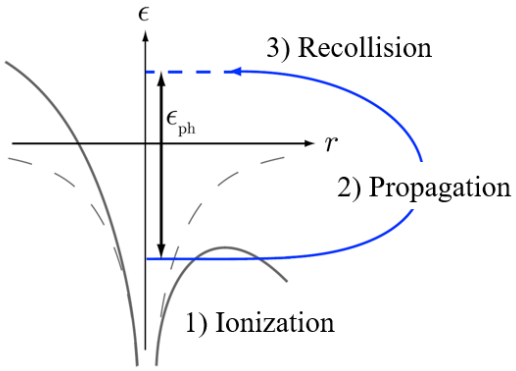

Figure 2.2: Three Step Recollision Model of HHG. [8] Images used with permission through Creative Commons Attribution 3.0 license, image modified from source.

$$E_{photon}^{max} = I_p + 3.17U_p \tag{2.4}$$

$$U_p = \frac{e^2E^2}{4m\omega^2} \propto I\lambda^2 \tag{2.5}$$

Due to the tunnel ionization process there are many points along the phase of the wave at which the electron can free itself. At what point it does so then affects the kinetic energy of the electron and the energy of the emitted photon, which in turn determines what order harmonic it will be. Figure 2.3 shows an assortment of different trajectories. The electrons start at the atomic core with zero velocity (0,0) and then can return to the core at position 0 or escape. The electron in trajectory "a" is ionized shortly before the phase of the laser reverses and is rapidly returned to the core. The electron in trajectory "c" on the other hand is ionized earlier in the phase and given a long time to propagate before recolliding. This results in trajectory "c" experiencing the start of another oscillation in the phase which slows it down. Both trajectory "a" and "c" end up with the same kinetic energy, as shown by their intersection on the y axis at position 0, and will therefore release photons with the same energy. Trajectory "b" is the cutoff energy, the trajectory which results in photons of the highest kinetic energy. This comes about when the electron is ionized at an optimal time in the phase so that the electron experiences a full half-period of the phase pushing it back to the atom before recolliding. In this trajectory the elctron is never slowed down after the initial reversal allowing it to achieve the maximum kinetic energy possible. Trajectory "d' represents the peak phase in the laser field and will therefore release the most electrons of any single phase but it makes no contribution to the creation of new photons since the kinetic energy of the electron in this trajectory is completely cancelled out. Trajectory "e" represents unfavourable phases where the electron does not return to the atomic core and no photons are produced. For most of the HHG spectra the contributing trajectories are of the "a" and "c" type,

accounting for all the harmonics except for the highest energy ones produced by "b". [15]

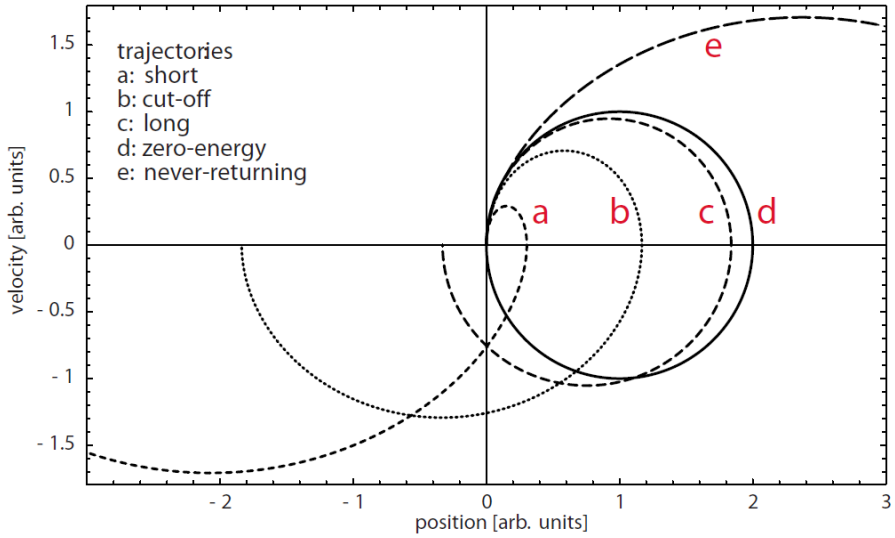

Figure 2.3: HHG Electron Trajectories. Image used with permission from APS. [15]

Since this process is occuring for a collection of atoms it can be assumed that roughly half the atoms will emit electrons near the positive maximum of the laser cycle while the rest will emit them near the negative maximum. This results in a series of coherent pulses separated by half the laser period. These two emissions cancel out the even harmonics leading to only odd-numbered harmonics being generated. Due to the effect of mutual coherence, the spectrum is determined by a fourier transform of this pulse train which will be a series of pulses separated by twice the laser frequency. This separation of twice the frequency leads to the formation of odd-numbered harmonics. [13]

2.1.3 HHG in Different Types of Gases

High harmonic generation can be performed in gases, plasmas, and solids. Gas is typically the most common medium for HHG and is also the focus of this thesis. Gases such as xenon, argon, helium, neon as well as nitrogen are often used in HHG experiments. This is because they are all in the gas phase both in STP as well as in vacuum conditions making them easy to use in gas jet / cell experiments. In addition to this all of them have reasonably high ionization potentials which, when applied to equation 2.4, allows for a longer reaching plateau region to be achieved. Xenon has an ionization potential of 12.13 eV, nitrogen a potential of 14.53 eV, argon a potential of 15.76 eV, neon a potential of 21.56 eV, and helium a potential of 24.59 eV. Based on this it is evident that gases like helium and neon can provide the highest order harmonics however, these gases generally have a lower conversion efficiency as shown in figure 2.4 [16]. In this figure xenon can be seen to have the highest conversion efficiency but falls off rapidly, argon has the second

highest but takes a longer time to fall off, and both the neon and helium have a long plateau but have rather low conversion efficiency. Similar results can be found elsewhere in the literature. [17]

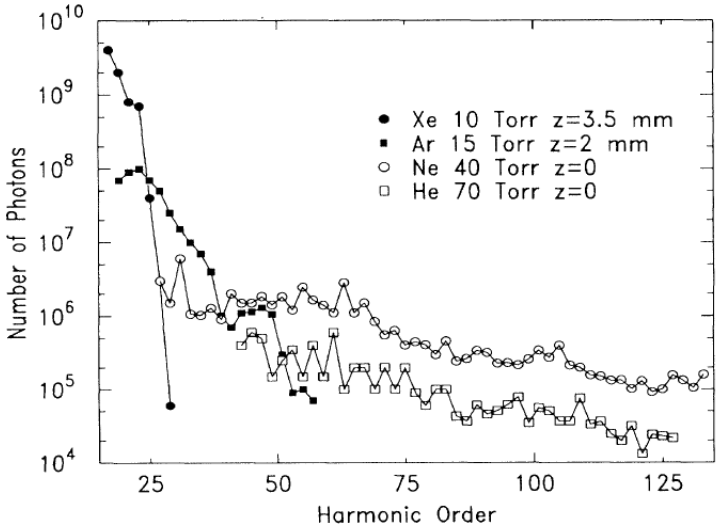

Figure 2.4: HHG in xenon, argon, nitrogen, and helium. Image used with permission from APS. [16]

2.1.4 Scaling of HHG in argon With Laser Intensity

The intensity of generated harmonics will increase with laser intensity until full ionization occurs. A good example of how the harmonics change with laser intensity is shown in figure 2.5 [18]. This shows the number of photons generated at the 15th harmonic of argon as a function of laser intensity. There are three regions, the ionization region where the gas starts to ionize rather than perform HHG, the plateau region as seen in figure 2.1, and the cutoff region where the intensity of HHG rapidly falls off as seen in figure 2.1. There is a rapid increase in the number of photons generated at this harmonic when it is still inside of the cutoff region, then a slower increase once inside of the plateau region. In the ionization region the number of photons generated at this harmonic still increase but much less than before showing that the gas is saturated with the plasma.

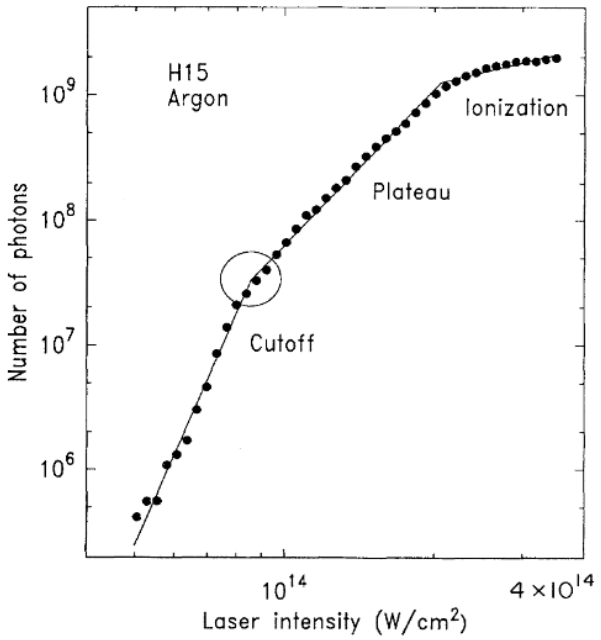

Figure 2.5: Scaling of the 15th harmonic of argon with laser intensity. The circled cutoff region indicates the 15th harmonic entering the plateau region, and the ionization region indicates when the laser begins to ionize the gas. Image used with permission from APS. [18]

2.1.5 Macroscopic Behaviour and Optimization of the High Harmonic Generation Process

In the case of a perfectly uniform beam and a perfectly uniform gas target the emitted extreme ultraviolet (XUV) radiation will be related in phase for different times / positions in the medium and therefore coherent. Provided that the phase of XUV stays constant in this way, the intensity of each harmonic is proportional to the number of atoms in the medium squared as shown in equation 2.6. [8]

$$S_q \propto \rho^2 S_{\Delta\phi} \tag{2.6}$$

In this equation S_q is the generated intensity of harmonic "q", ρ is the gas density, and $S_{\Delta\phi}$ is the phase matching condition neglecting re-absorption and varies between 0 and 1, where 1 refers to fully phase matched constructive interference and 0 is fully destructive interference.

Phase Matching

The concept of phase matching is most easily discussed for the case of SHG and is shown in figure 2.6. In this figure there is a phase mismatch of Δk between the wavevector of the second harmonic and the combined wavevectors of the two fundamental photons. When the fundamental is in phase with its harmonics, subsequent harmonics will add on top of each other forming a coherent beam. The larger the phase difference, however, the less coherent the harmonic beam will be reducing the overall intensity of the harmonics.

This difference in phase can have a very large impact on conversion efficiency as shown in figure 2.7. [19]

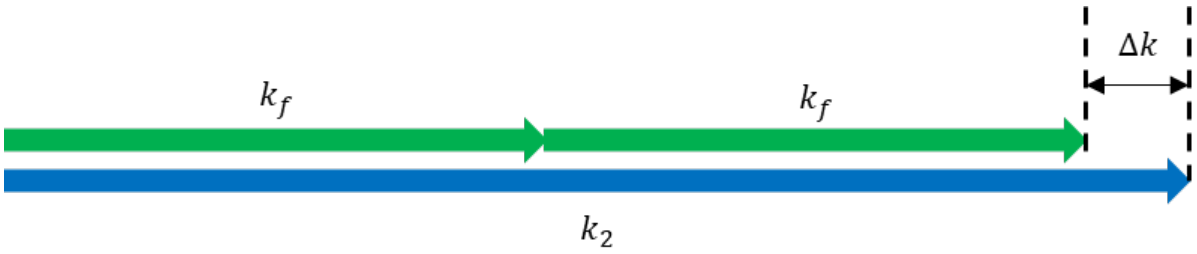

Figure 2.6: (left) Diagram showing a phase mismatch in the SHG process. (right) Effect of phase mismatch over several different atoms resulting in a lower magnitude field.

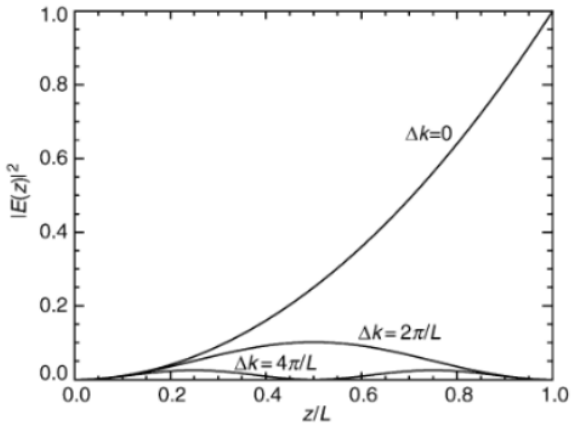

Figure 2.7: Plot of the intensity as a function of position for varying values of Δk. Image used with permission from Elsevier. [19]

Typically in HHG there are four main effects which can lead to phase mismatch. These are the Guoy phase (a phase shift resulting from the laser focusing) Δk_g, the dipole phase Δk_d (a phase shift resulting from the dipole moment of the ionized electron and the intensity of the laser), and dispersion of the laser in both the neutral gas and the plasma Δk_n, Δk_p respectively. [8] The phase shift resulting from the dispersion of the laser in either neutral gas or plasma is self explanatory but the Guoy and dipole phase shifts require slightly more explanantion. The Gouy phase shift is a very rapid phase shift that takes place over a small distance (of the order of the Rayleigh range, typically tens of micrometers) at laser focus. The phase goes from $-\pi/2$ to $\pi/2$ as the beam moves through the focus. In order to avoid the Gouy phase gas targets are often placed shortly before or after the laser focus. [8,15,20] This is of course technically the same geometry as FCHHG but with a much smaller distance (a few millimeters) and so does not compromise the study of FCHHG being performed in this thesis. The dipole phase results from the phase of the dipole moment from each electron that is ionized by the laser. As explained earlier, multiple electron trajectories may contribute to the generation of a harmonic in the plateau region. The longer a trajectory of an electron is,

the greater an impact the intensity of the laser will have on it. This will in turn have an impact on dipole moment resulting from that electron, and in turn the dipole phase from that moment. [8,15,20,21] Intensity is typically radially dependent for Gaussian beams so there will be a radial component to the phase but it is also dependent on the beam size and will naturally increase as the laser approaches focus leading to an axial component to the phase as well. Prior to focus the dipole phase shift is considered to have a negative phase contribution while after focus it is considered to have a positive phase contribution. [8] Therefore it can sometimes be ignored if the gas medium is placed perfectly at laser focus. Other possible sources of mismatch include that from a non-linear refractive index in the material which is neglected as its contribution is not very large in typical HHG experiments, and group velocity mismatch which is neglected as the phase mismatch is assumed to change very slowly with frequency. This leaves the total mismatch equation as:

$$\Delta \mathrm{k} = \Delta \mathrm{k}_g + \Delta \mathrm{k}_d + \Delta \mathrm{k}_n + \Delta \mathrm{k}_p \tag{2.7}$$

Assuming a Gaussian laser propagating along axis z these terms can be written as:

$$\Delta k_g = -q\frac{\partial}{\partial z}[\zeta(z) - \frac{kx^2}{2R(z)}] \tag{2.8}$$

$$\Delta k_d = \alpha(q)\frac{\partial I}{\partial z} \tag{2.9}$$

$$\Delta k_n = q\frac{\omega}{c}(n_1 - n_q) \tag{2.10}$$

$$\Delta k_n = q\frac{\omega}{c}(n_1^e - n_q^e) \tag{2.11}$$

$$R(z) = z(1 + (\frac{z_R}{z})^2) \tag{2.12}$$

$$z_R = \frac{1}{2}k\omega_0^2 \tag{2.13}$$

Here q is the harmonic being examined, z is the distance through the medium, x is the transverse position along the Gaussian beam, $\zeta = atan(\frac{z}{z_R})$ is the Guoy phase shift for the fundamental beam with Rayleigh length z_R and beam radius of curvature R(z). $\alpha(q)$ is a proportionality constant as it is common practice to approximate dipole phase as proportional to laser intensity. n_1 is the refractive index of the neutral gas for the

fundamental beam and n_q the refractive index of the neutral gas for the harmonic, and similarly n_1^e is the refractive index of the ionized plasma for the fundamental beam and n_q^e is the refractive index of the ionized plasma for the harmonic. Lastly, ω is the frequency of the driving laser, k the wavevector of the laser, and ω_0 is the beam waist.

Since the FCHHG geometry does not take place at laser focus the Gouy phase may be considered constant across the gas jet and its contribution to the overall phase shift may be neglected. The dipole phase and two dispersion terms must be considered however. As mentioned earlier the phase shift from the dipole is considered to be negative prior to laser focus, similarly the phase shift due to the plasma dispersion will also be negative. This leaves the neutral gas dispersion as the only positive contribution to the phase shift. [8] This leaves the control of phase matching as a question of optimization between the backing pressure (controlling the dispersion terms through gas density) and the laser intensity at the interaction region (controlling the dipole phase). Of course with FCHHG there will be a larger variation in gas density within the interaction region than is seen in traditional HHG which may lead to a larger spatial dependence on phase.

Absorption

With the concept of phase matching established, attention can now be turned to the effects of absorption. XUV light is strongly absorbed by most of the gases used to create HHG. For example the absorption of XUV in just 100 um of argon is shown in figure 2.8. [22]

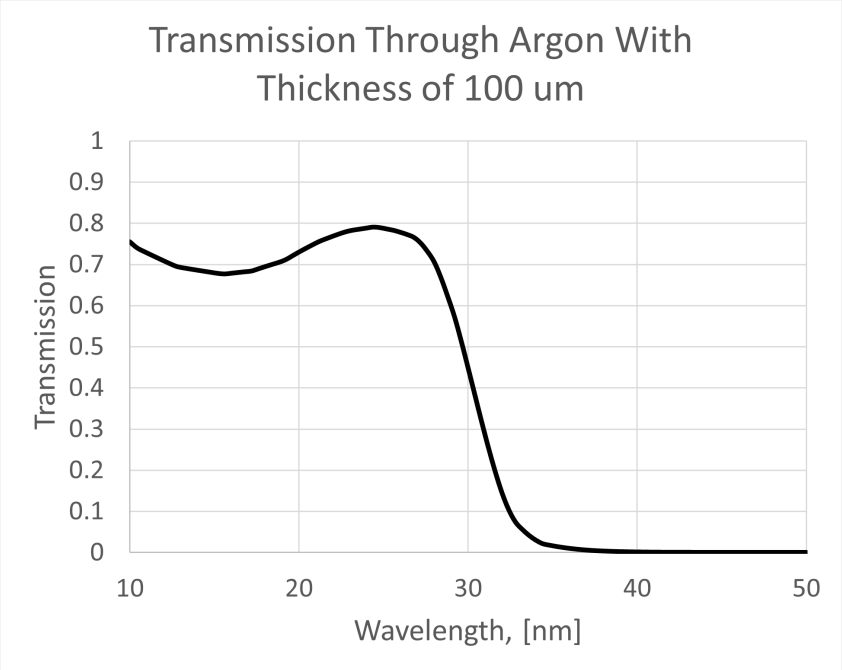

Figure 2.8: Plot of the transmission spectra of Argon for a 100 um gas sheet at a density of 0.00178 g/cm^3 for photon wavelengths of 10 to 50 nm. [22]

With this and the effect of phase matching in mind, equation 2.6 can be expanded to include these terms resulting in equation 2.14 [8].

$$S_q \propto |d_q \int_0^L exp[i(\Delta k + i\kappa_q)(L - z)]dz|^2 \tag{2.14}$$

Here L is the length of the medium, d_q and κ_q represents the dipole amplitude and absorption coefficient of the gas for the qth harmonic respectively. The phase difference Δk and absorption coefficient κ_q can be replaced by the coherence length ($L_{coh} = \frac{\pi}{\Delta k}$) and absorption length ($L_{abs} = \frac{1}{2\kappa_q}$) to put the equation in terms of gas jet length, coherence length, and absorption length. Figure 2.9 shows how the intensity scales based on the ratio of coherence length to absorption length, with the ideal case being a very large coherence length compared to a very small absorption length. This corresponds to a very small phase difference and absorption coefficient. Unfortunately, as was seen before in figure 2.8, the absorption coefficient of the media used in HHG is significant over much of the XUV region. The phase matching can be optimized to drastically reduce the phase difference, however, this is done by varying the gas density which will in turn have an effect on the absorption of XUV. Of course having a higher density also means having a greater number of atoms to become XUV emitters. Lastly, the length of the gas jet could be increased rather than increasing the density although this will have much the same effect. This creates a complicated relationship where the optimal density / length of the gas jet is not immediately clear. However, most of the terms for phase mismatch and absorption scale with density so the final dependence is on the product of density and the interaction length.

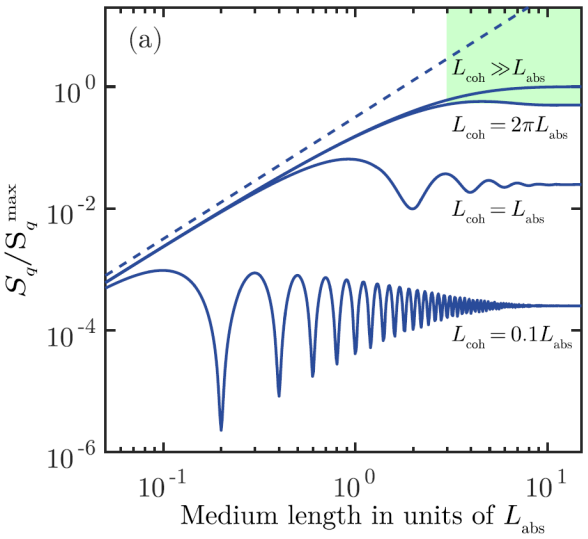

Figure 2.9: A plot showing the intensity resulting from different values of the coherence length in relation to the absorption length. Images used with permission through Creative Commons Attribution 3.0 license. [8]

Relevant HHG Research

Some research has been done using FCHHG but this has been done with the goal of studying other behaviour rather than FCHHG specifically. An example of this is a paper by Bom et.al. [23], this experiment splits the laser beam and has one part hit a solid target, ionizing it and creating a plasma. The other beam is then partially focused onto the plasma in order to create HHG. While this experiment does make use of FCHHG it does not examine the process in any detail.

Another paper by Nayak et.al. [11] is also useful to examine, both in terms of its relevance to FCHHG and its determination of ideal pressure-distance conditions for HHG. Nayaks experiment made use of two separate gas jets, one placed at laser focus and one with a variable position. In order to carry out these studies a weak focusing mirror with a 9 m focal length was used to extend the Rayleigh range of the focused beam. This increased transverse beam area allowed for a greater number of XUV emitters to be created without passing the ionization intensity and creating a hot plasma. The use of two gas jets was for the purposes of quasi-phase matching. [11,24,25] Quasi-phase matching is a technique to introduce periodic modulation of the local strength / phase into the medium which can counteract some of the destructive interference between locally generated fields. Varying the position of the second nozzle showed that energy of the XUV could be increased by a factor of $\tilde{1}.7$ with the second gas jet placed at a position of $\pm 5cm$ from laser focus as shown in figure 2.10. The ultimate result of Nayaks paper is achieving XUV energies of approximately $30\mu J$ and $10\mu J$ for each of the 11th, 13th, and 15th harmonics of xenon and argon respectively. This translated to conversion efficiencies of 2×10^{-3} and 3×10^{-4} for each of the 11th, 13th, and 15th harmonics of xenon and argon respectively with enhancement from the dual jet. Without the dual jet configuration the result is still quite high at 1×10^{-3} and 2×10^{-4}. This conversion efficiency is extremely high as HHG will typically have conversion efficiencies on the order of 10^{-8} to 10^{-5}. The second nozzle by itself is using the FCHHG geometry, but the paper does not examine HHG process when only the second nozzle is used and does not make use of the focusing behaviour of the XUV light. The result in this paper is, as far as I am aware, the highest conversion effiiciency achieved for HHG. However, with the use of FCHHG and a more powerful laser it may be possible to achieve an even higher output energy for the harmonics.

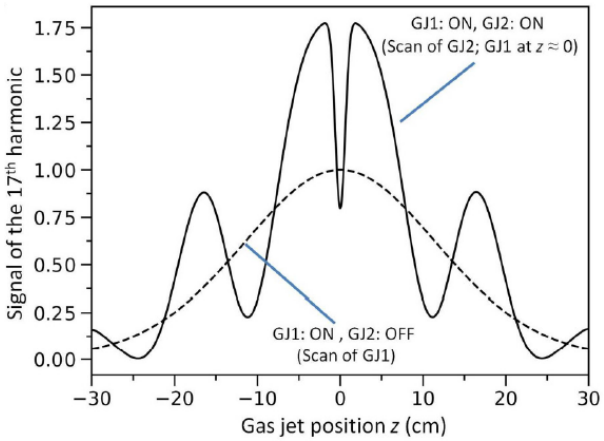

Figure 2.10: Nayak et. al. calculated harmonic yield in Ar gas as a function of gas pressure and medium length. Images used with permission from APS. [11]

The paper also models the dependency on the pressure-length product in order to achieve maximum conversion effiiciency. A contour plot of the calculated efficiency for a single gas jet with varying pressure and medium length is shown in figure 2.11. This was derived from the equations shown in several other papers [25-27] which determined the conversion efficiency under optimal phase matching conditions. The plot shows that a product of $\tilde{3}7.5$ mm-mbar is ideal for HHG in a single gas jet and balances out the competing variables well. It should be noted that this is for a gas jet placed at laser focus and may not be the ideal case for the FCHHG geometry but it provides a general idea of the anticipated pressure-length product.

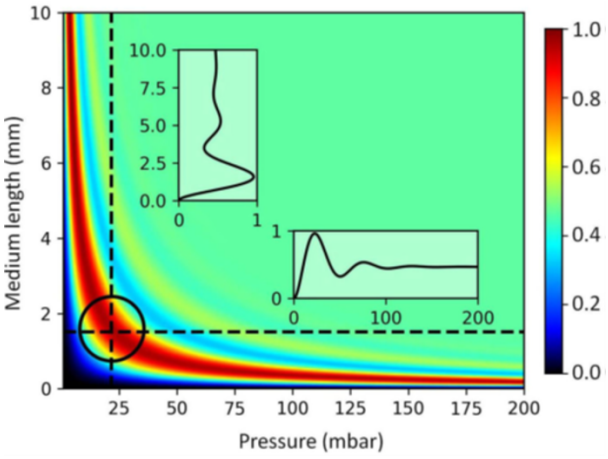

Figure 2.11: Nayak et. al. calculated harmonic yield in Ar gas as a function of gas pressure and medium length. Images used with permission from APS. [11]

2.2 Nozzle Design

As outlined in the previous section, the gas density profile which the laser passes through can have a large impact on HHG. In order to create ideal conditions for HHG it is desirable to have a uniform gas density profile across the entire width of the beam. Equations

2.10 and 2.11 rely on the refractive index and therefore the density of the gas jet for the contributions to the phase mismatch due to dispersion. Having density variations across the width of the beam would lead to spatial phase variations which would decrease the overall coherence of the focused XUV and therefore the intensity. For the purpose of analyzing whether the FCHHG geometry behaves as expected spatial variations in density are also a disadvantage as they could lead to hot spots of XUV in regions with high density making it more difficult to interpret data. Density variations along the beam path will have less of an impact but may lead to variations in dispersion, and therefore phase matching, as the beam propagates through. Since the FCHHG geometry takes place some distance away from focus the beam width can be quite large. As such a wide gas nozzle is employed to produce a wide, uniform gas jet which the beam can pass through. Outlined here are a few of the important considerations when designing such a nozzle.

2.2.1 de Laval Nozzle

A de Laval nozzle is a type of nozzle that achieves supersonic gas velocities through the use of a converging-diverging design (provided that there is a relatively high pressure before the converging section and a relatively low pressure after the diverging section). Equation 2.15 [28] relates the nozzle cross-sectional area (A) divided by the cross sectional area of the narrow nozzle throat (A_{throat}), to the Mach number (M) of a gas with specific heat ratio (γ). Similarly, equation 2.16 can be used to determine the density of gas as a function of Mach number. Mach number itself is defined in equation 2.17 showing that it is dependent on the velocity of the gas (v) and the speed of sound in the medium (v_{sound}). The speed of sound (assuming an ideal gas) is then given by the square root of the specific heat ratio of the gas, the ideal gas constant (R), the temperature of the gas (T), and the molar mass of the gas (M_m). [28]

$$\frac{A}{A_{throat}} = \frac{1}{M}\left[\frac{2}{\gamma+1}\left(1+\frac{\gamma-1}{2}M^2\right)\right]^{\frac{\gamma+1}{2(\gamma-1)}} \tag{2.15}$$

$$\frac{\rho}{\rho_0} = \left(1+\frac{\gamma-1}{2}M^2\right)^{\frac{-1}{\gamma-1}} \tag{2.16}$$

$$M = \frac{v}{v_{sound}} \tag{2.17}$$

$$v_{sound} = \sqrt{\frac{\gamma RT}{M_m}} \tag{2.18}$$

Equation 2.15 shows that for subsonic flow speeds (M < 1) the flow speed will increase for a decreasing cross section, and for supersonic flow speeds (M > 1) the flow speed will increase for an increasing cross section. This is the justification behind the design of de Laval nozzles. A purely converging nozzle cannot reach velocities greater than the speed of sound. [29] However, in de Laval nozzles, the gas is initially forced into a compression region where the cross sectional area of the nozzle decreases, accelerating the gas up to Mach 1. After this point the gas flows into an expansion region where it is accelerated to velocities greater than Mach 1. For the purposes of creating a uniform gas field achieving higher velocities is desired since it will result in the gas traveling farther before it has the chance to spread out.

The relation between the Mach number and the speed of sound in an ideal gas shows that a low speed of sound will lead to a higher Mach number. Since the speed of sound in an ideal gas is related to temperature a lower temperature can also result in a higher Mach number.

These equations can be used to make design decisions regarding the general shape of the nozzle. They also make the assumption that the fluid flow through the nozzles is perfectly isentropic and can be reversed without expending energy. For the most part this is true but it does not account for the generation of shocks in the system which cause the process to become non-isentropic.

2.2.2 Prandtl-Meyer expansion fan

Within supersonic flow, small regions in a gas where properties such as pressure, temperature, density, and velocity change by a large amount can be created. [30-32] These regions propagate through the gas as waves moving at or faster than the speed of sound in the local material. Waves which move at or faster than the speed of sound are called shock waves. Those that move at the speed of sound are known as Mach waves and, unlike regular shock waves, remain isentropic. [31] While shock waves can take on a number of different forms, of particular interest to nozzle design are those resulting from supersonic flow encountering a corner. When supersonic flow moving alongside a wall encounters a corner on the wall there can be two reactions. If the corner is concave the gas flow will be compressed by it and lead to the creation of an oblique shock wave (pictured on the right of figure 2.12). This type of shock is of the sort seen when supersonic aircraft break the sound barrier. Depending on the nozzle design this type of shock may be important but with the simple converging diverging geometry all supersonic flow will occur in the expansion region after the throat and so no concave corners will be encountered. On the other hand, if the corner is convex, a Prandtl-Meyer expansion fan will be created (pictured on the left of figure 2.12). A Prandtl-Meyer expansion fan can be understood as an infinite series of Mach waves propagating from supersonic flow passing a convex

corner. Flow that passes through these Mach waves is turned by an infintesimal amount until, at the end of the fan, the flow is now moving in the direction of the wall after the corner. [31]

The Prandtl-Meyer expansion fan, while similar to shock waves, is not technically a shock wave and is in fact an isentropic process since it is composed entirely of isentropic Mach waves. However, a rapid turn around a corner can still result in the creation of a shock wave. Therefore, in practice, simple de-Laval nozzles can still experience shocks in the expansion region unless a gradual curved corner is used.

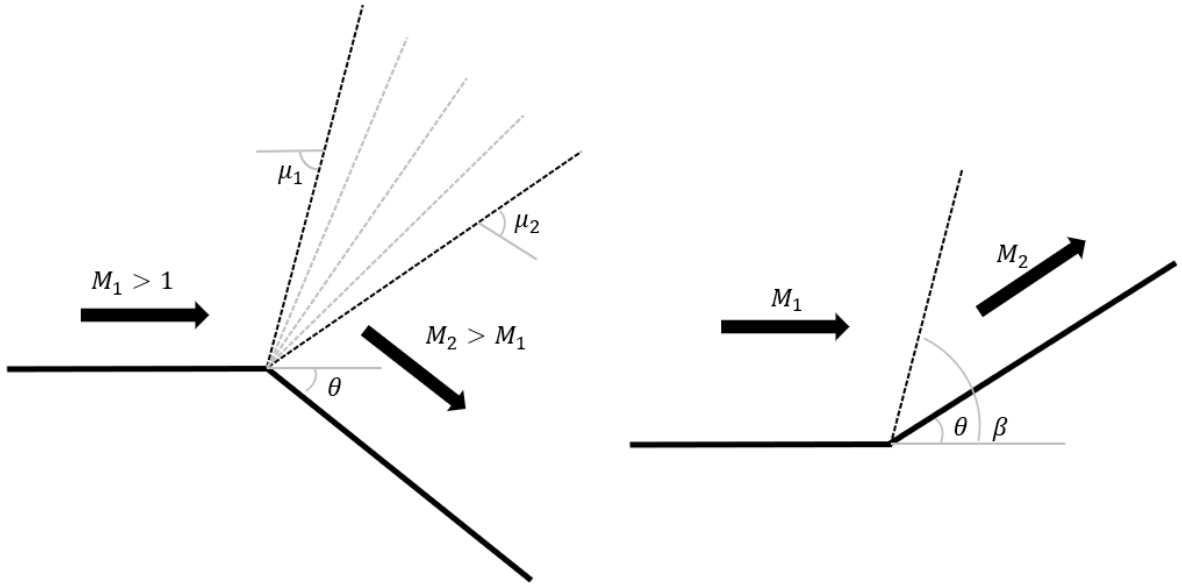

Figure 2.12: Prandtl-Meyer Expansion Fan (left), Oblique Shock (right)

The Prandtl-Meyer function (ν) is given in equation 2.19. The function by itself is not very useful but combined with equation 2.20 it allows for the angle of the corner (θ) to be found if both the Mach number before (M_1) and the Mach number after (M_2) the corner are known. Alternatively, it can be used to find the Prandtl-Meyer function of either of these Mach numbers based on knowning the other Mach number and the angle of the corner, although this requires a more complicated technique [33]. The left part of figure 2.12 shows off the behaviour of the Prandtl-Meyer expansion fan. It also shows that the two extreme angles of the expansion fan are given by the local Mach angles μ_1 and μ_2. The equations for calculating both of these angles are given in equation 2.21, it is important to note that while μ_1 is based off of the wall angle before the corner μ_2 is instead based off the wall angle after the corner. Rather than attempting to consider the entire expansion fan and all it's various angles it is more practical to consider a single characteristic line in the center of the expansion fan. The angle of this characteristic line is simply derived from the average of the local Mach angles and wall angles.

$$\nu(M) = \sqrt{\frac{\gamma+1}{\gamma-1}} \cdot arctan\sqrt{\frac{\gamma-1}{\gamma+1}(M^2-1)} - arctan\sqrt{M^2-1} \tag{2.19}$$

$$\nu(M_2) = \nu(M_1) + \theta \tag{2.20}$$

$$\mu_1 = arcsin\left(\frac{1}{M_1}\right), \mu_2 = arcsin\left(\frac{1}{M_2}\right) \tag{2.21}$$

$$\mu_c = \frac{1}{2}\left(arcsin(\frac{1}{\mu_1}) - \theta_1 + arcsin(\frac{1}{\mu_2}) - \theta_2\right) \tag{2.22}$$

Maximum Turn Angle

The Prandtl-Meyer expansion fan also allows for the maximum angle over which the flow can turn to be found as seen in equations 2.23 and 2.24. [31] Generally within the nozzle itself angles will be kept below this maximum, however, these equations can give insight into how the gas spreads out after it exits the nozzle. The change in wall angle after the exit of the nozzle is typically larger than the maximum turn angle, and so the expansion is based on the maximum turn angle rather than the wall angle. Since ν increases for a larger mach number, and since ν_{max} is a constant dervied from the adiabatic heat index of the gas, it can be seen that higher mach numbers lead to slower divergence after the gas leaves the nozzle.

$$\nu_{max} = \frac{\pi}{2}\left(\sqrt{\frac{\gamma+1}{\gamma-1}} - 1\right) \tag{2.23}$$

$$\theta_{max} = \nu_{max} - \nu(M_1) \tag{2.24}$$

Many applications for nozzles both in the field of HHG as well as other areas such as rocketry would prefer to have the gas flow diverge as little as possible after leaving the nozzle. Therefore it would seem that increasing the Mach number arbitrarily high would be the solution. However, equation 2.15 shows that as the Mach number increases so too must the nozzle exit area which will be a drawback for most applications. Another solution would be to decrease the throat area of the nozzle. This however decreases the overall mass flow of the nozzle and can lead to choking of the nozzle which can be disadvantageous. In this sense nozzle design is a balancing act between having an acceptable Mach number, an acceptably sized nozzle exit, and a throat large enough for an acceptable mass flow rate.

2.2.3 Boundary Layers

After the nozzle throat, in the supersonic expansion region, viscosity starts to play a large role along the nozzle throat. The effects of viscosity and friction result in the gas velocity becoming 0 at the wall and necessitates the existance of a thin boundary layer where the velocity transitions from the high velocity in the center of the nozzle to 0 at the wall. [30] Moving further from the throat the velocity will increase and, as a result, the boundary layer must expand to accommodate this increase. Because the boundary layer increases for increasing velocity it will effectively decrease the size of the nozzle which will in turn decrease the maximum velocity. [30] Depending on the purpose of the nozzle, boundary layers can have a large impact on performance but in the case of this thesis a large enough nozzle is used making boundary layers less important but worth noting. An example of boundary layer is shown in 2.13. The region covered by contour lines on the edge is the boundary layer and can be seen to increase further down the nozzle.

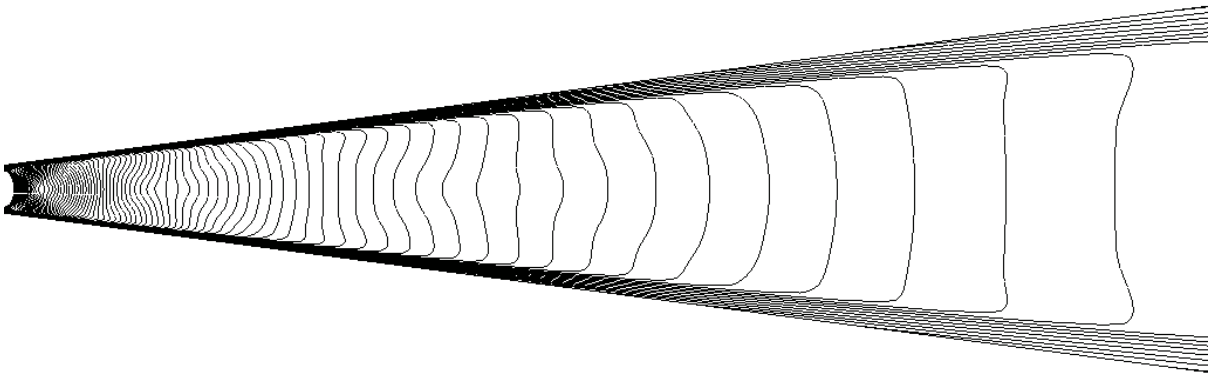

Figure 2.13: Boundary layers forming in a gas jet as shown by contour lines of density, simulated in ANSYS: FLUENT [34].

The size of the boundary layer will also play a role in determining the steepness of the gradient from high to low pressure immediately after the gas exits the nozzle. [30] For large boundary layers (i.e. high Mach numbers) the slope will be more gradual and the density profile less flat-top as a result. This is an important consideration for experiments occuring very close to the nozzle exit. For experiments occuring further from the nozzle exit the impact of the boundary layers on the gradient is relatively minimal compared to the overall spread of the gas. While the flat-top nature of the density profile at the nozzle exit is hindered by high Mach numbers due to boundary layers, the profile further away is helped by high Mach numbers due to the maximum turn angle of the Prandtl-Meyer expansion fan although, as mentioned earlier, there are other factors to consider when designing the nozzle.

2.3 Discussion

In this chapter the general background of high harmonic generation and supersonic nozzle design has been introduced. In the following chapters a detailed characterization of the supersonic nozzle used for experiments will be presented and the results of the HHG experiment conducted at the CLPU will be presented.

Chapter 3

Nozzle Design and Analysis

This chapter discusses the development and modelling of the rectangular sheet nozzle used for focal cone high harmonic generation (FCHHG). A brass nozzle was manufactured for use in the CLPU experiment. This nozzle was based on a design in reference [35] which was a parabolically shaped nozzle. A 3D printed version of this exact nozzle was created but due to the high inlet pressures employed (often 50 bar or higher) this nozzle was not used in the CLPU experiment. The brass nozzle was designed to have many of the same characteristics as the 3D printed nozzle. It was designed with the same throat diameter (0.42 mm) and overall length (14.47 mm) as the 3D printed nozzle but had a straight 15° opening angle and a slightly smaller outlet width of 3.28 mm (3.78 mm on the 3D printed nozzle). The length of the outlet was kept the same as the 3D printed nozzle at 20.4 mm. The rest of the nozzle was designed for ease of manufacturing and therefore broken into several pieces which would be screwed together. These included two sides containing the nozzle contour, another two sides to act as ends to the nozzle, and a large single piece which connected the nozzle itself to the solenoid valve. In addition to the screw holes to hold the nozzle together another 8 screw holes were made on the top of the nozzle which could be used for attaching a blade to focus the gas jet, although no such attachment was made during the CLPU experiment. The nozzle itself is pictured in figure 3.1 along with a cutaway showing the internal workings of the nozzle, and an image of the nozzle contour.

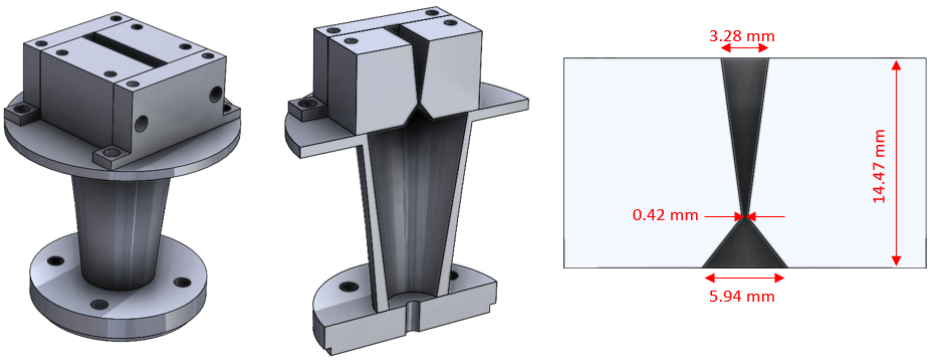

Figure 3.1: Picture of the Solidworks model for the nozzle, a cutaway of this model, and an image of the expansion nozzle contour with dimensions

3.1 2D Fluid Dynamic Simulations

In order to characterize the density profile produced by the gas jets and determine an optimal design for creating a gas sheet of roughly uniform density for the laser to pass through, fluid dynamic simulations were carried out using the program ANSYS: FLUENT [34] (hereafter referred to as Fluent). Fluent is a leading fluid simulation software widely used in industrial and research applications. It uses a finite volume method, a numerical method of solving partial differential equations using volume integrals in a partitioned domain, to perform simulations and provides many customization options to allow the simulation of different types of fluid flow. The methods by which the simulation was run are outlined in appendix 1.

Simulations were run with argon gas at 50 bar. The top image in figure 3.2 is a 2D cut-out of the density contour along the narrow cross section of the nozzle (as shown on the right of figure 3.1) resulting from the 2D Fluent simulation, while the lower image is of the Mach number contour lines across the same cross section. From these plots it can be seen that shocks which form at the nozzle throat due to the sharp corner propagate through to the nozzle exit creating fluctuations in density and Mach number throughout the nozzle. At the nozzle outlet these shocks lead to the creation of a higher density region on the edges of the nozzle which propagates out into the chamber. As the gas propagates out of the nozzle the high density peaks on the edges converge inward, eventually joining together to form a single peak before falling off further. This effect helps to focus the gas jet to some extent and decrease the rate at which the gas spreads out.

Once the gas exits the nozzle it has more freedom to spread out but will be limited by the maximum turning angle as discussed in relation to the Prandtl-Meyer expansion fan in Chapter 2. At the nozzle outlet the gas achieves a Mach number of around 4.5 and the wall angle is almost 90 degrees. As such the maximum turning angle is much smaller than the wall angle so the gas expansion is then limited by the maximum turning angle. As the Mach number increases this maximum turning angle will decrease as shown in equations

2.19, 2.23, 2.24 allowing for the gas moving at high Mach numbers to be projected further from the nozzle before it spreads out. The Mach number continues to increase outside of the nozzle since the vacuum surrounding the nozzle allows for continual expansion of the gas.

Equation 2.15 can be applied to investigate the accuracy of the simulation with regard to the Mach number. When using the area-ratio equation the length of the nozzle is the same at both the nozzle throat and exit simplifying the equation to a width ratio equation as only the width of the nozzle factors in to the calculation. For argon this results in a Mach number of 4.6 which is what the Fluent simulation predicts as well, for diatomic gases like nitrogen the Mach number should be 3.7.

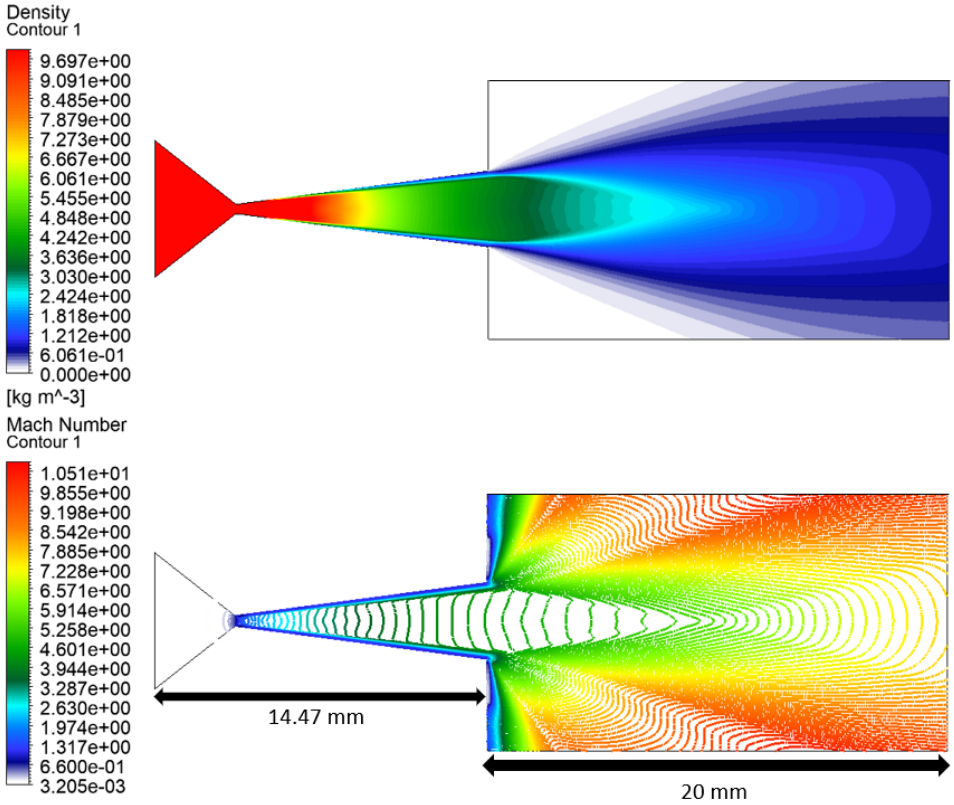

Figure 3.2: Density contour plot (top) and Mach number contour line plot (bottom) of the nozzle. The backing pressure is 50 bar.

Figure 3.3 shows lineouts along the nozzle axis for Mach number, density, pressure, and temperature. There are a few bumps and ripples in the plots due to the effect of shock waves. As expected from an converging - diverging nozzle the Mach number reaches 1 at the nozzle throat and increases further in the expansion section. The pressure, density, and temperature are close to steady state in the converging section until just before the throat is reached at which point there is a rapid decline in all three.

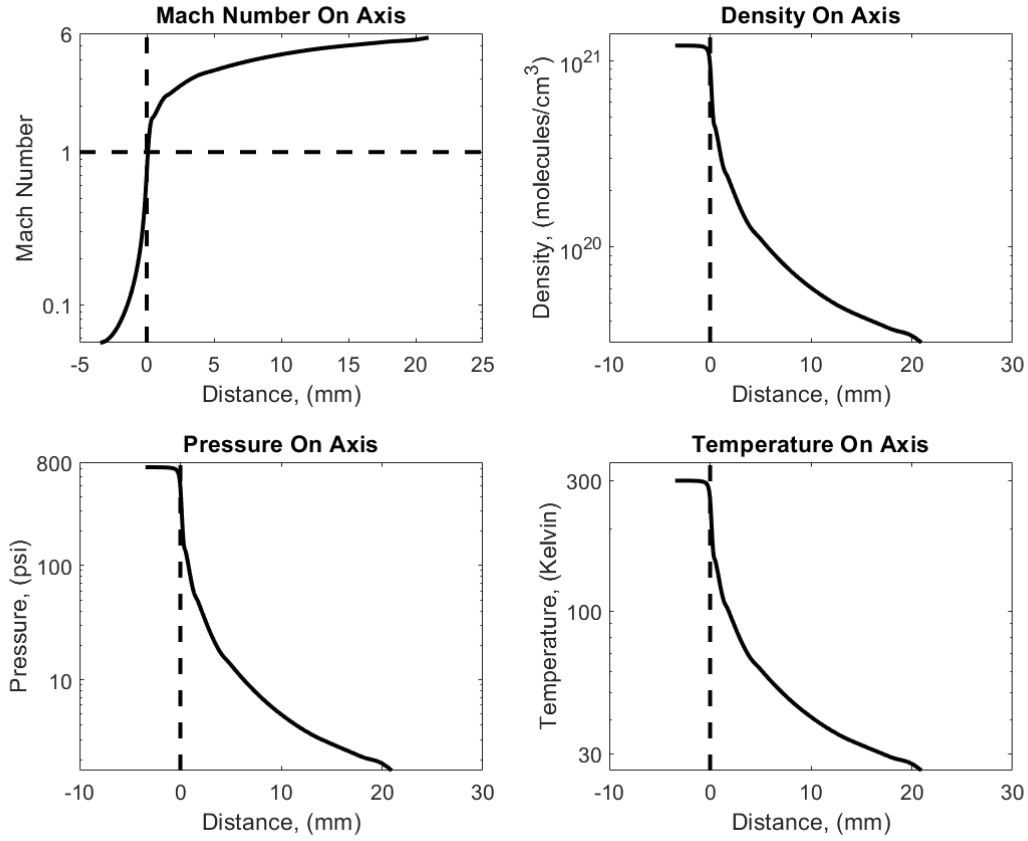

Figure 3.3: Logarithmic plots along the nozzle axis of Mach Number, Density, Pressure, and Temperature as a function of position relative to the nozzle throat. Vertical dashed lines represent the location of the nozzle throat while the horizontal dashed line in the Mach number plot represents Mach 1. The backing pressure is 50 bar.

Figure 3.4 shows the transverse density profiles across the nozzle for varying distances from the nozzle exit. At the exit (0 mm) the density profile is a very clean, relatively flat topped profile. It still retains the peaks on the edges as mentioned earlier but the relative variation between the center and these edges is rather small. As the distance from the nozzle increases the density begins to spread out with the peak density dropping and a larger spread of wings on the side. The remaining density eventually forms a single round peak which continues to fall off further until the gas is spread thin across the entire profile.

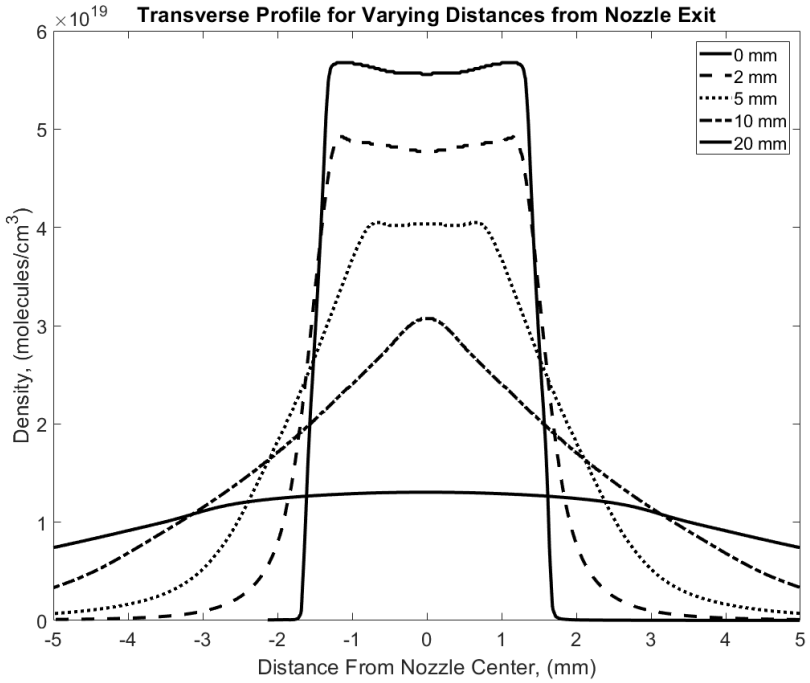

Figure 3.4: Transverse plots of density at varying distances above the nozzle exit. The first solid line with the larger peak is the 0 mm lineout, the dashed line is the lineout at 2mm, the dotted line is the lineout at 5 mm, the dotted and dashed line is the lineout at 10 mm, and the second broader solid line is the 20 mm lineout. The backing pressure is 50 bar.

3.2 Manufacturing

The manufacturing of the nozzle was done by the machine shop at the University of Alberta. Brass was used as the medium as it is soft enough to easily cut while being strong enough to withstand high gas pressures. Unlike plastic, brass does not experience strong outgassing which was important due to the high vacuum used at the CLPU. The more complicated components were cut using a CNC machine with more traditional techniques used for the simpler pieces. A picture of the assembled nozzle is shown in figure 3.5.

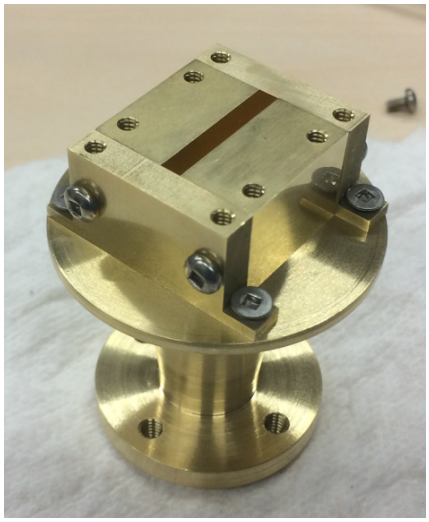

Figure 3.5: Picture of the assembled brass nozzle.

3.3 Interferometry

Interferometry is a useful method to evaluate the gas density coming from a nozzle. Regions with higher gas density will have a higher refractive index leading to a noticeable shift in the interference fringes. [35,36] Two separate interferometry tests were conducted on the nozzle in order to ascertain the gas density profile. One of these was at the CLPU prior to the start of the experiment, the other was at the University of Alberta after the experiment.

At the CLPU the gas jet was attached to a high speed pulse valve, Parker 009-1643-900, with an orifice size of 0.99 mm. The valve was set to be open for 7 ms. At the University of Alberta a similar valve, Parker 009-1669-900, was used. This also had an orifice size of 0.99 mm and an opening time of 20 ms was used.

3.3.1 CLPU Interferometry

Carlos Salgado-López headed up the interferometry efforts at the CLPU both by building and testing the interferometer as well as analyzing the data. Full credit goes to him for the results shown in this section. Carlos used a Mach-Zehnder interferometer design. Due to the orientation of the nozzle this had to be made in a vertical setup, unfortunately, this left it somewhat more susceptible to vibrations from the gas jet than it otherwise may have been and so some of the interferograms are blurred in regions. An example interferogram of the nozzle with gas on and off is shown in figure 3.6, based on this result there appears to be a fringe shift of approximately half a fringe immediately after the nozzle exit. The gas used for these tests was argon and the backing pressure used for the density plots was 50 bar.

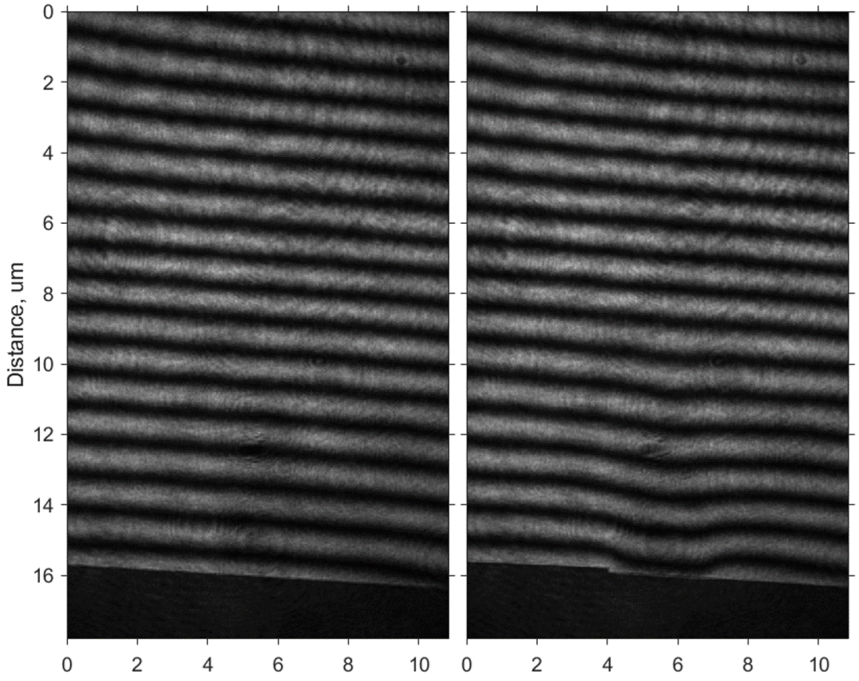

Figure 3.6: Interferogram of Argon gas off (left) and gas on at 50 bar (right).

In the case of gas nozzles, interferometry is used to determine the change in the refractive index that the light sees which, in turn, provides the density of the gas at that location. The equations used by Carlos for this are:

$$\delta\phi = \frac{2\pi}{\lambda}(n-1)L \tag{3.1}$$

$$\rho = \frac{2\epsilon_0}{\alpha}(n-1) \tag{3.2}$$

Where $\delta\phi$ is the phase shift, λ the laser wavelength (in this case 632.8 nm from a HeNe laser), n the refractive index, and L the length of the medium. For the second equation ρ is the density of the gas, ϵ_0 is the permittivity of free space, and α is a factor comprised of the refractive index at STP and the density of the gas at STP. For simplicity it was assumed that L was the length of the gas jet and that there was a uniform density across this whole region. Carlos had written his own program in order to extract the phase shift, a similar program is developed for the next section and will be elaborated on there.

The results after this analysis can be seen in figures 3.7a and 3.7b. Figure 3.7a shows contour plots of the density for varying times after the solenoid valve leading into the nozzle has opened. The horizontal bands that are present in some pictures are the result of blurring discussed earlier. These are not too important for the shots taken a short time after the valve has opened but become more impactful as time goes on. In particular the images at 8 and 9 ms experience a great deal of vibration which throws the results

of these images into question. The solenoid was open for 7 ms but due to the large connector section of the gas nozzle it is expected that gas will continue to flow for several milliseconds after the solenoid is closed which is what is seen in these images. Figure 3.7b shows a plot of the peak density measured at each timestep. The density appears to increase until about 3 ms before leveling off between 1.3 and 1.5×10^{18} molecules/cm^3 until about 7 ms. After this there is a large spike in the data, this is likely due to the increase in vibrations rather than a real increase in density. Overall, these plots are more or less what is expected based on the simulations as shown in figure 3.2.

The simulations also predict an overall higher density, as figure 3.4 shows with densities on the order of 10^{19} molecules/cm^3 . This is for two reasons, first because as the gas flows through the solenoid and into the nozzle there will be a difference between the measured backing pressure and the actual pressure which reaches the entrance of the nozzle and the simulation does not model this. The large adaptor chamber before the nozzle will also affect this as it will take some time to fill which will reduce the pressure coming out of the nozzle. Second, the 2D simulation predicts that the entire backing pressure is within the 2D plane of the simulation whereas in 3D the backing pressure is spread out across the length of the nozzle and the backing pressure in a single slice would be significantly lower. Thus it is not expected that the simulation will have a correct prediction of the absolute density but the general shape of the profile will be correct. Scaling factors will be derived from comparison to the interferometry performed at the University of Alberta so that the simulations may be used as an estimate of absolute density in the CLPU experiment.

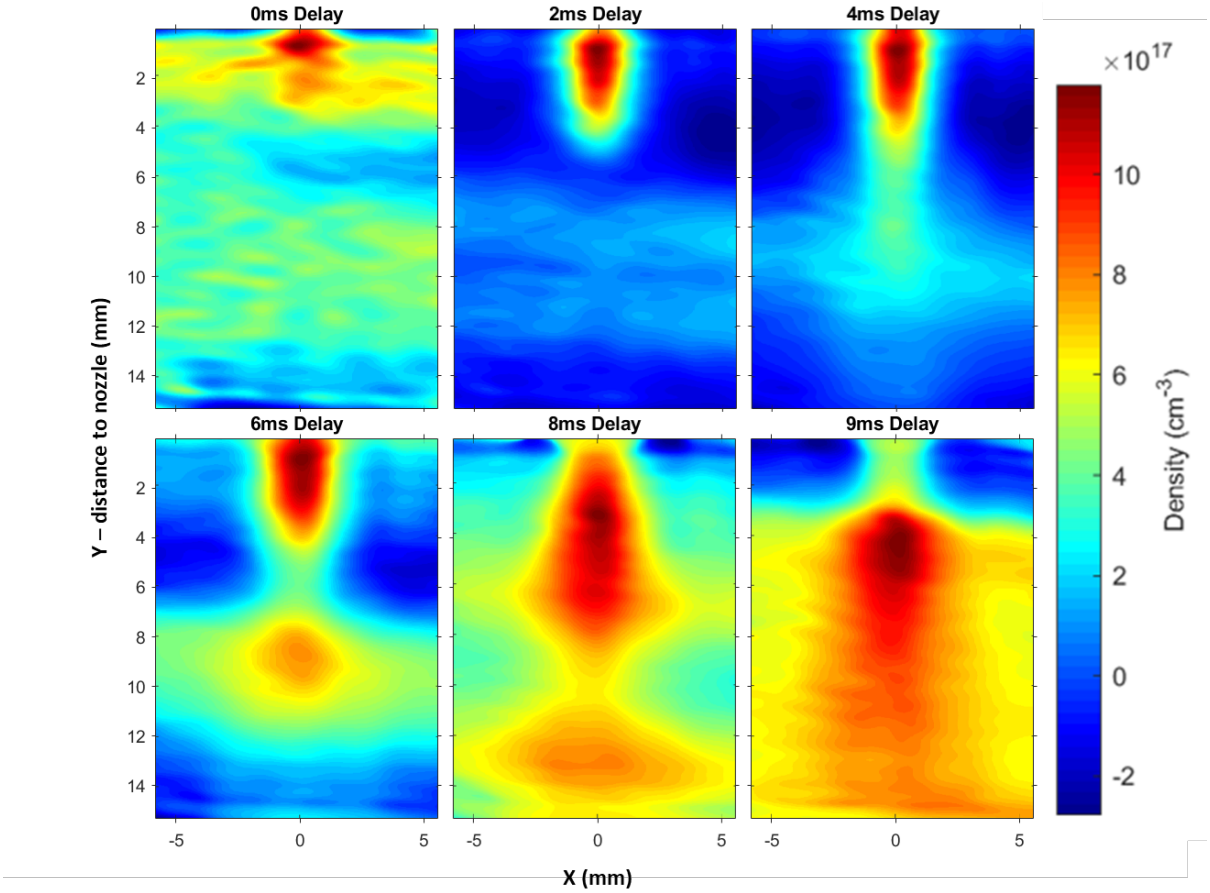

(a) Density contours for varying times after the solenoid has opened. Backing pressure of 50 bar.

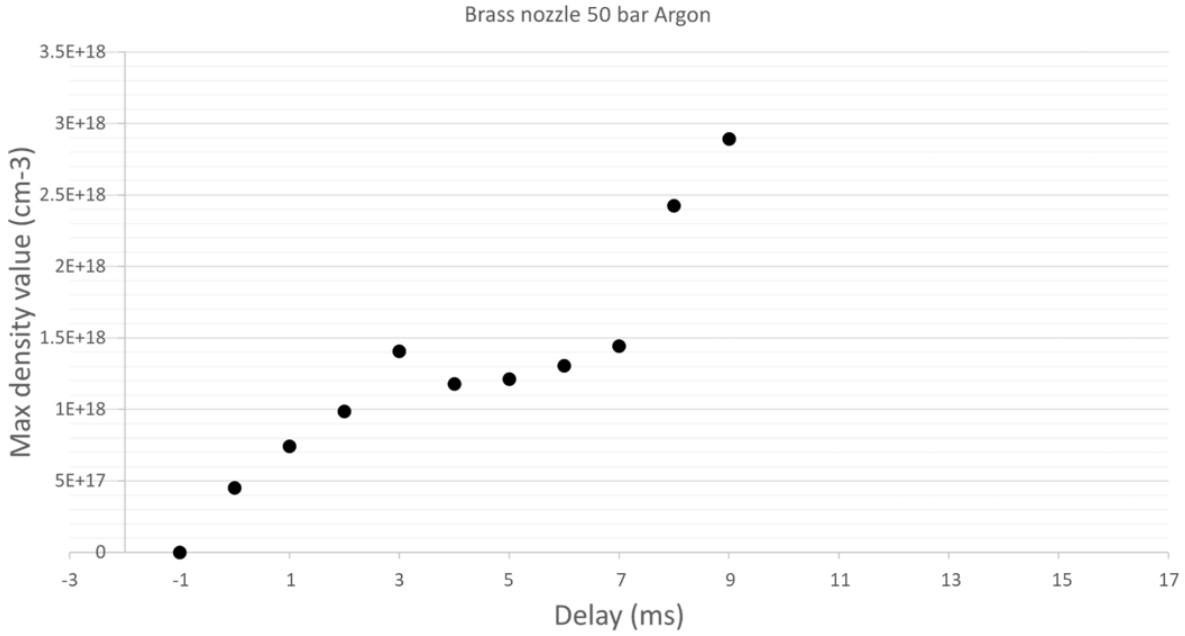

(b) Graph of peak density recorded. Vibrations in the later times may be responsible for some error in these measurements. Backing pressure of 50 bar.

Figure 3.7: CLPU Interferometry Results

Error in the Gas Jet

During the interferometry conducted at the CLPU the gas was able to displace one of the sides of the nozzle by approximately 0.35 mm. This is visible in figure 3.9. This displacement was unnoticed during the CLPU experiment and was left unfixed during the Univeristy of Alberta interferometry so as to better understand the gas density profile used during the experiment. This is discussed further in appendix 2 but based on the interferometry profiles seen later it does not seem to have had a large impact on the gas density profiles.

3.3.2 University of Alberta Interferometry

A Mach-Zehnder interferometer was built at the University of Alberta for use with a 260 nm UV laser. This laser was chosen in order to obtain larger phase shifts. As can be inferred from equation 3.1 the shorter wavelength of the UV results in a larger phase shift compared to that from a visible or infrared laser. The layout of the interferometer is shown in figure 3.8

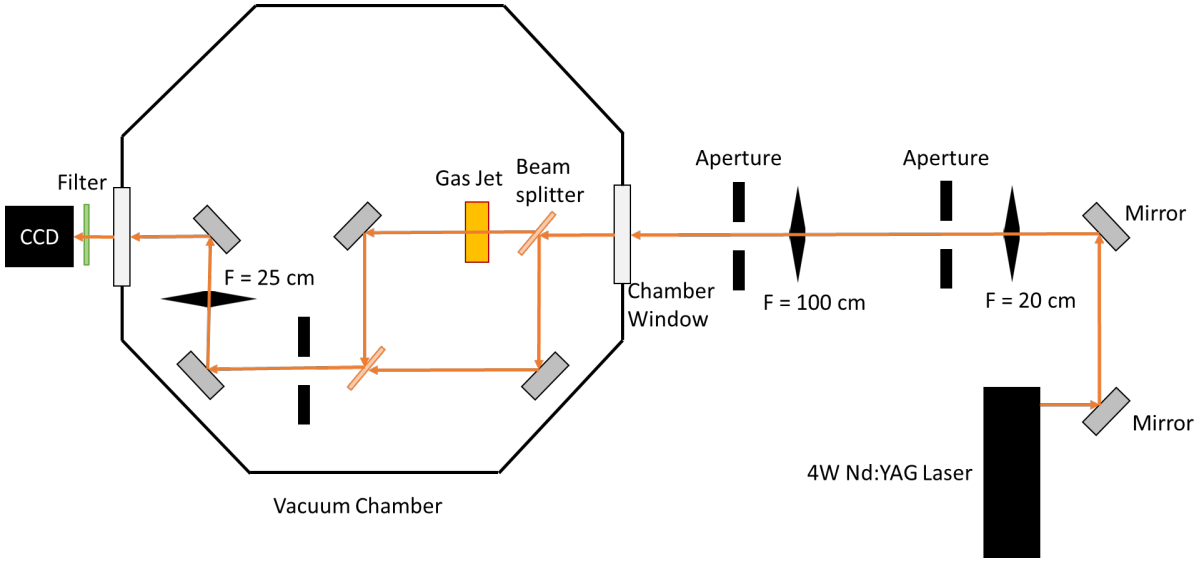

Figure 3.8: Layout for the Mach-Zehnder interferometer used at the University of Alberta to measure the gas jet profile (not to scale).

A Q-switched Nd:YAG laser [37] was used to generate a 10 ns probe pulse which was frequency converted to the 4th harmonic at 266 nm wavelength in order to generate the UV light which was used to probe the gas jet. The beam is initially expanded using a 200 mm lens and then collimated using a 1000 mm lens to obtain a spot size of 1.5 cm. After this the beam passes into the vacuum chamber where it encounters the first beamsplitter. One part of the beam is reflected onto a mirror and from there onto the second beamsplitter, the other part of the beam passes through the first beam splitter and the gas jet before reaching a mirror and then reflecting to the second beamsplitter.

After this the beams are recombined and are then focused onto the CCD. Two 25 x 36 mm UVFS 50:50 beamsplitters were used to split and recombine the beam, and a UV reflective neutral density filter was used to protect the camera from an excessive amount of light.

Shots with the gas on, gas off, and laser off were taken at varying delays in order to examine the time-dependent relationship of the gas jet. The solenoid valve leading into the nozzle was turned on for 20 ms. Examples of the gas on and gas off for argon gas are shown in figure 3.9. The backing pressure used here was 657 psia or 45.3 bar. The error in the nozzle can be seen on the left hand side of the image, there may also be a very small error on the right hand side but it is unclear when that developed. Based on visual analysis the fringe shifts appear to be a little bit more than 1 fringe immediately after the nozzle exit.

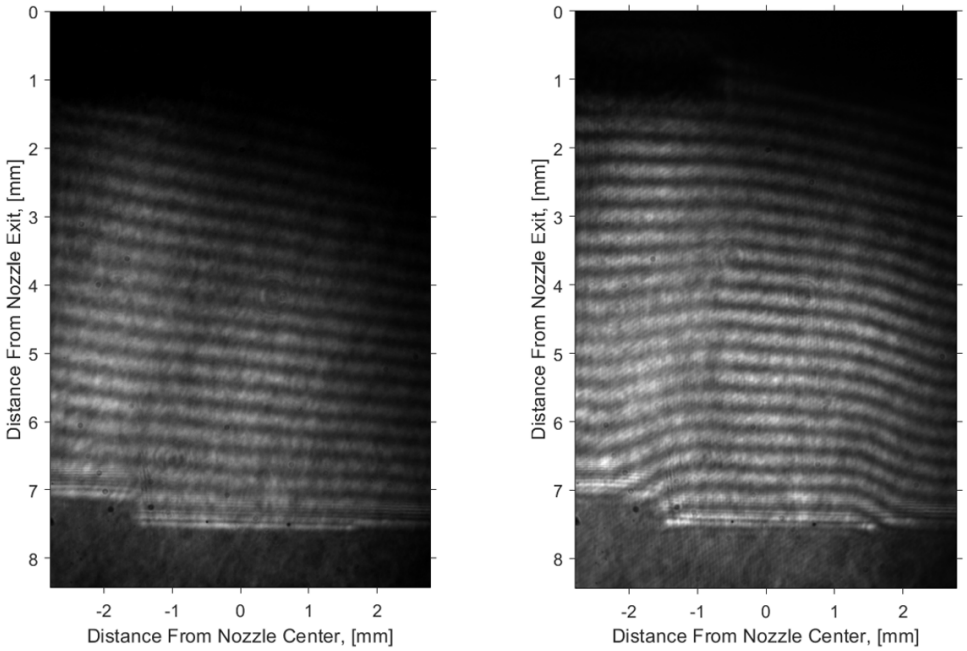

Figure 3.9: Interferogram of gas off (left) and gas on at 657 psia (45.3 bar) backing pressure using argon gas (right).

After obtaining a series of shots they were transformed into phase maps using a fourier transform technique outlined in a paper by Takeda et.al. [38]. This method assumes that the interference fringes have the form of equation 3.3, where a is the amplitude variation, f_0 is the spatial carrier frequency, and c is represented by equation 3.4. Where b and ϕ are the amplitude variation and phase of c respectively.

$$g(x,y) = a(x,y) + c(x,y)exp(2\pi i f_o x) + c^*(x,y)exp(-2\pi i f_o x) \tag{3.3}$$

$$c(x,y) = \frac{1}{2}b(x,y)exp(i\phi(x,y)) \tag{3.4}$$

The fourier transform of equation 3.3 is then shown in equation 3.5. Here the zeroth order term occurs at f (where f is the spatial frequency in the x direction) and is represented by A while the two side terms C and its complex conjugate C^* are at $f - f_0$ and $f + f_0$ respectively.

$$G(f, y) = A(f, y) + C(f - f_0, y) + C^*(f + f_0, y) \tag{3.5}$$

Eliminating all terms but C, translating it so it is centered on f, and then taking the inverse fourier transform gives the c term from equation 3.4 by itself. The phase is then isolated by taking the complex logarithm as shown in equation 3.6. As can be seen, the phase is the only imaginary term in this expression and so taking only the imaginary component allows for the phase to be isolated. It should be briefly mentioned that centering C on f is only required to get the absolute phase map. This is not necessary to know however, what is needed is the phase map of gas on in relation to gas off which can be found by subtracting two separate phase maps and so the choice of frequency f will not have any real effect.

$$log[c(x, y)] = log[\frac{1}{2}b(x, y)] + i\phi(x, y) \tag{3.6}$$

This process was accomplished by importing the images into Matlab and using many of the built-in functions there. The only thing lacking from this is the wrapping of 2π phase shifts but this can be dealt with easily by using Matlabs built-in "unwrap" function. However, since each of the columns is evaluated individually, there can be discontinuities in phase between each column of the phase map so a simple algorithm is also used to bring each column into line. After this the phase maps for both the gas on and gas off can be obtained as shown in figure 3.10. Outside of the region with fringes these phase maps are naturally unrealiable and have seeming random values, but inside the contours match up well with that of the raw interferograms.

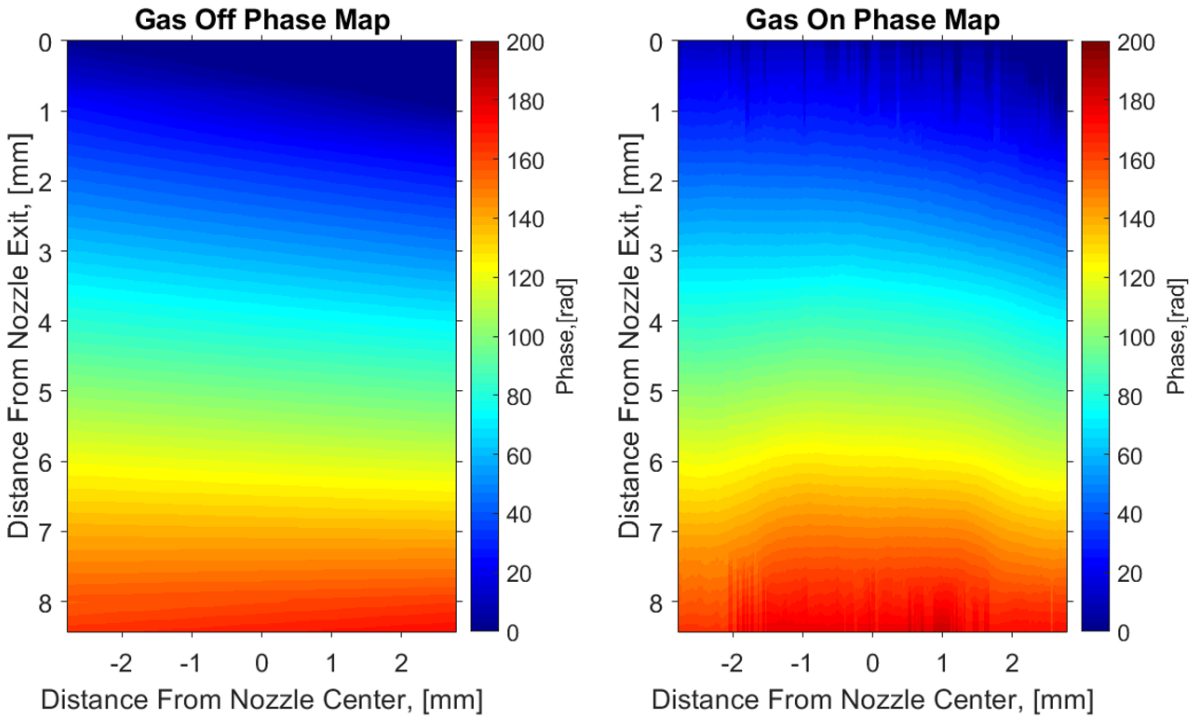

Figure 3.10: Phase map of gas on at 657 psia (45.3 bar) backing pressure, 20 ms delay using argon gas (right), and calculated gas off phase map (left).

The phase maps are then subtracted from each other to determine the phase shift. Unfortunately, a similar issue to the vibrations seen with the CLPU interferometry has occurred. Instead of creating blurring, vibrations have led to a slight change in the fringes after the nozzle has puffed. To work around this the gas on image is taken by itself and the gas off image ignored. Lineouts along either edge of the gas on image are taken and adjusted based on simulated values. Linear plots between these lineouts are then used to create an effective gas off map. While this may introduce some error, this method should provide reasonably accurate values to compare with the simulations.

With a map of the phase shift established the refractive index can simply be calculated from the phase shift through equation 3.7. Here n is the refractive index, $\Delta\phi$ the phase shift, λ the laser wavelength, and L the length of the medium taken to be 20.4 mm exactly for simplicity. After the refractive index is obtained, the density is simply found by equation 3.8. Here ρ is the measured density in the gas jet while ρ_0 and n_0 are the density and refractive index of the gas at STP.

$$n = \Delta\phi * (\frac{\lambda}{2\pi})/L + 1 \tag{3.7}$$

$$\rho = \rho_0 \frac{n-1}{n_0 - 1} \tag{3.8}$$

Argon

A figure of the density contours with argon at 657 psia backing pressure for varying times after the solenoid has opended is shown in figure 3.11. From this it can be seen that at 0 ms there is no noticeable density change. This makes sense as the solenoid has only just opened and the gas will not have had enough time to reach the nozzle exit. At 1 ms a small amount of gas starts to leak out but very little, it is not until 5 ms that the main portion of the gas begins. At 10 and 20 ms the gas continues to increase in density until the solenoid closes at 20 ms. During this portion the density profle can be seen to exhibit the focusing effect predicted by the simulations with lower density wings on the sides, further helping to validate the simulations. At 21 ms, 1 ms after the solenoid has closed, there is already a drop off but the density remains high. The nozzle comes with a rather large resevoir region so it will take some time before the density drops significantly. By 23 ms the density is about the same as it was at 5 ms and continues to drop until 30 ms when there is only a small amount of gas left.

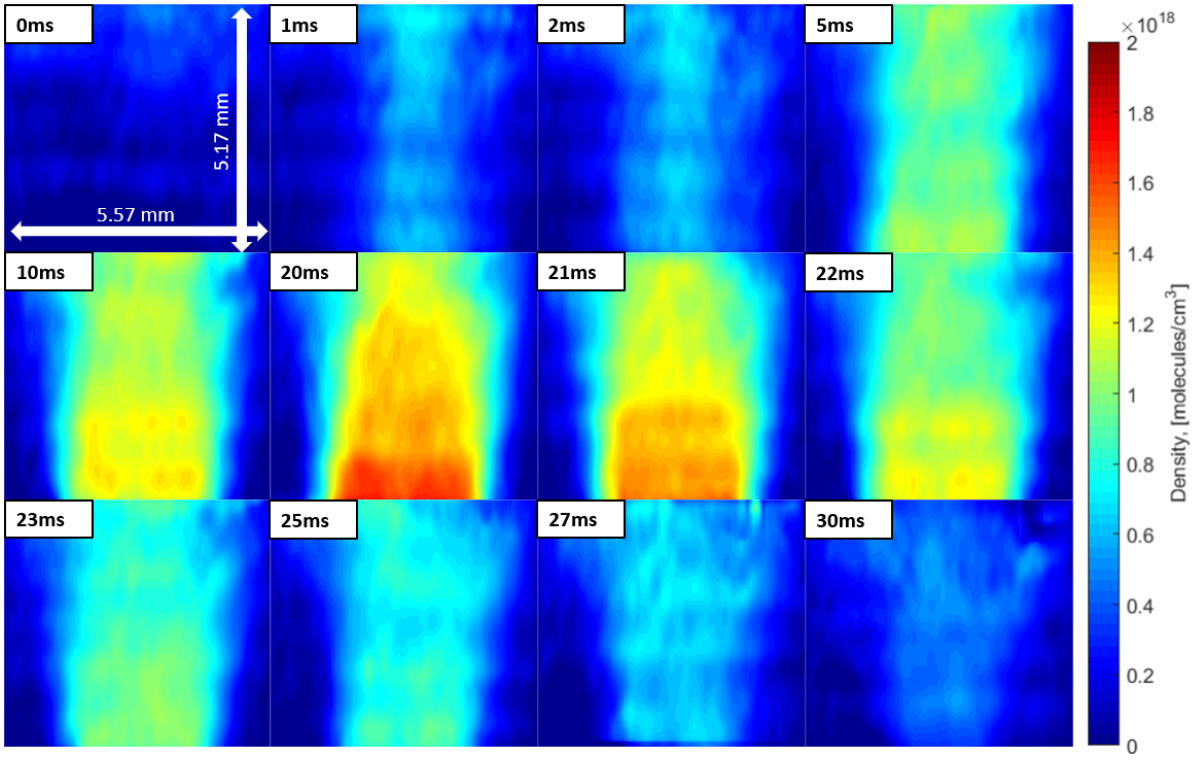

Figure 3.11: Density contours for varying times after the solenoid has opened with 657 psia backing pressure, argon.

Figure 3.12 shows the peak density 0.5 mm above the nozzle from the interferometry in figure 3.11 as a function of time. This shows that the density initially has a rapid increase but then slows down, still increasing but at a slower pace. Eventually the density appears to plateau with a value around 1.7×10^{18} molecules/cm^3 between 15 and 20 ms. After the nozzle closes at 20 ms the density falls off much more rapidly than it initially rose.

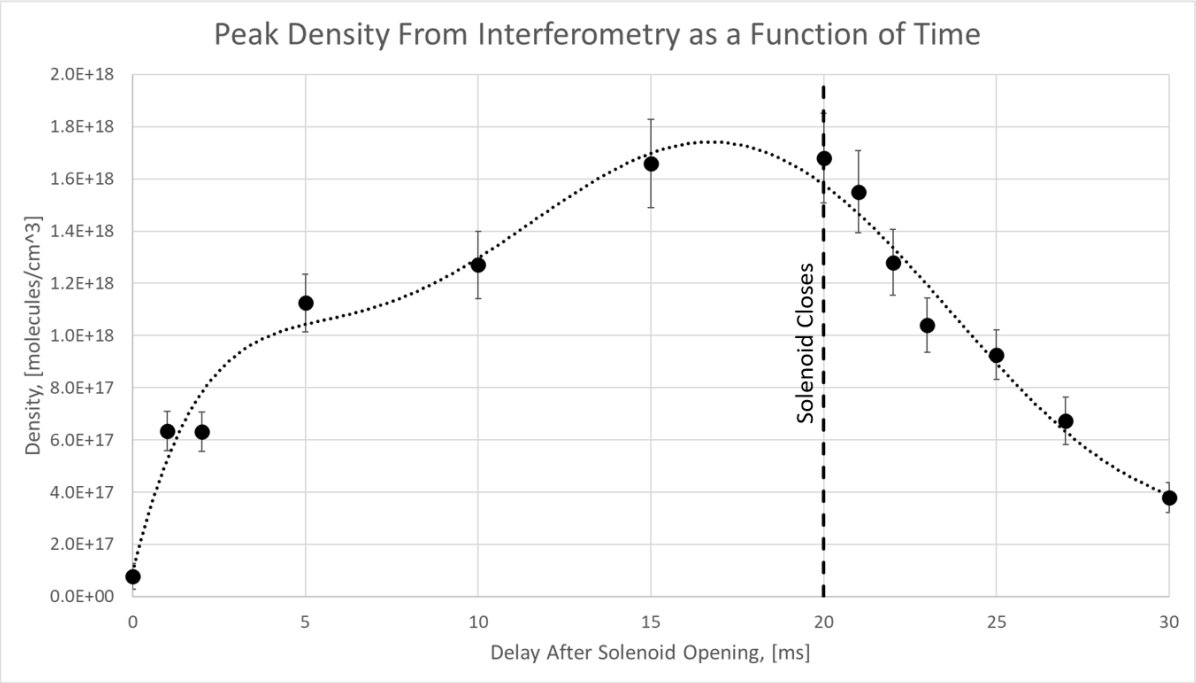

Figure 3.12: Peak density as a function of delay time from solenoid opening. Backing pressure 657 psia. An error of 10% of the peak density is assumed and a trendline is shown to display the general behaviour of the data.

Lineouts taken at 20 ms after the solenoid opens are shown in figure 3.13 with both the interferometry data and the simulated data. A scaling factor of 30 has been applied to the simulated data which was run with a backing pressure of 660 psia. For distances close to the nozzle, particularly 0.5 and 1 mm, the simulations fall off much more rapidly than the interferometry which predicts a more gentle slope, but the size of the flat top region agrees well. The distances at 2 - 5 mm are much closer in agreement on the sides than the smaller heights showing very good agreement in shape. The peak density at 0.5 mm above the nozzle exit is 1.68×10^{18} molecules/cm^3.

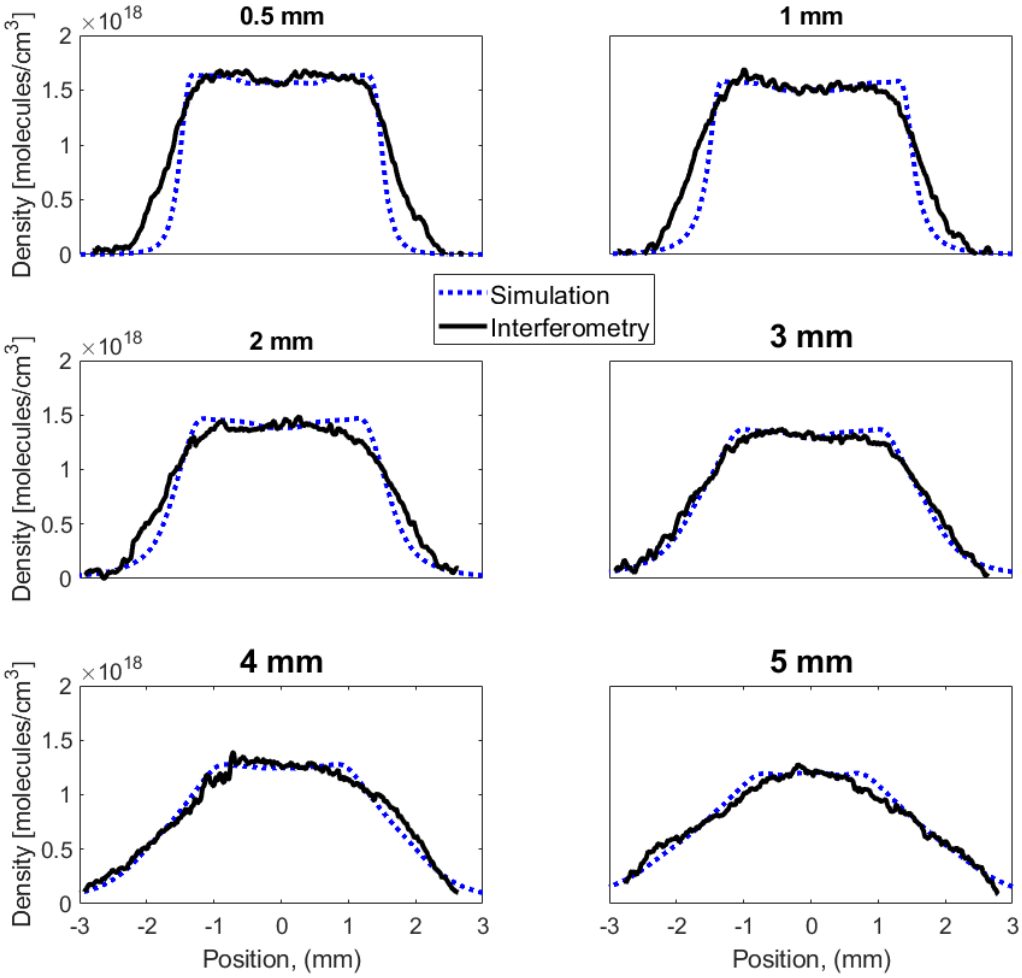

Figure 3.13: Comparison between simulated and interferometry of transverse lineouts for varying distances above the nozzle exit. Interferometry at the 20 ms delay and 657 psia backing pressure, simulation at 660 psia scaled to 657 psia and then scaled by 30 to match interferometry data. The solid black line is the measured interferometry data and the dotted blue line is the simulation.

Figure 3.14 shows the density contours of argon for varying backing pressures. A constant 20 ms delay is selected as that has provided the highest density plots. The results are as expected, with increasing density as the backing pressure increases.

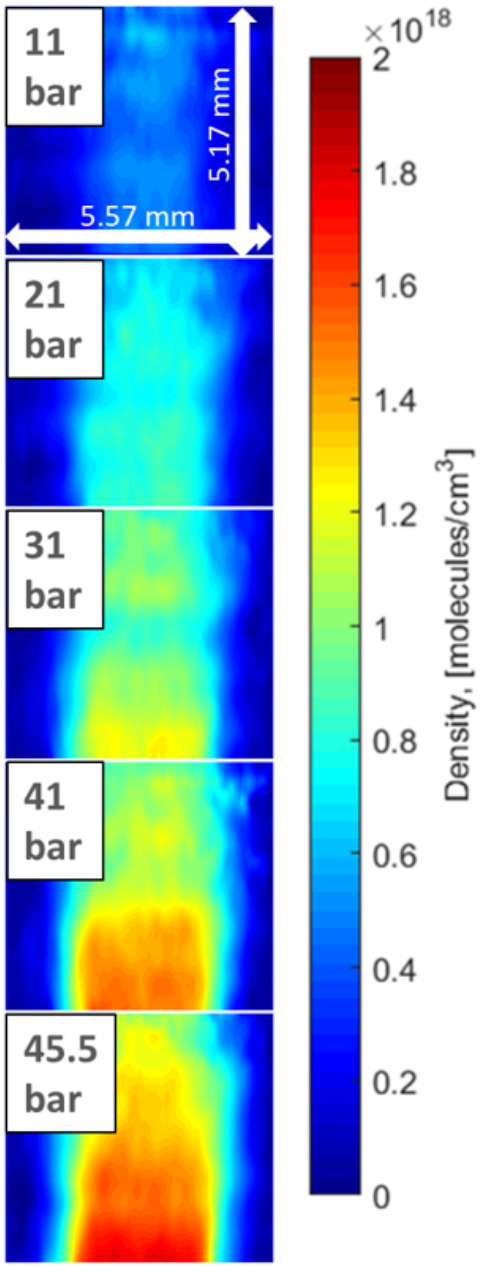

Figure 3.14: Interferometry density contours for varying backing pressures with 20ms delay, argon.

From equation 2.16, it would seem that the gas density at nozzle exit would scale linearly with the density (and therefore backing pressure) at the inlet. The measurements here can be used to examine this.

Figure 3.15 is derived from the data shown in figure 3.14. Lineouts taken at 0.5, 1, 2, 3, 4, and 5 mm above the nozzle exit are taken for each of the contour plots of figure 3.14. The density reading at the center of each lineout from each contour plot is then taken as a representative of that lineouts density. Since the scaling of the density with varying backing pressure is what is of interest here each of the density readings was then divided by the density at 660 psia backing pressure for each of the lineouts thereby normalizing the data.

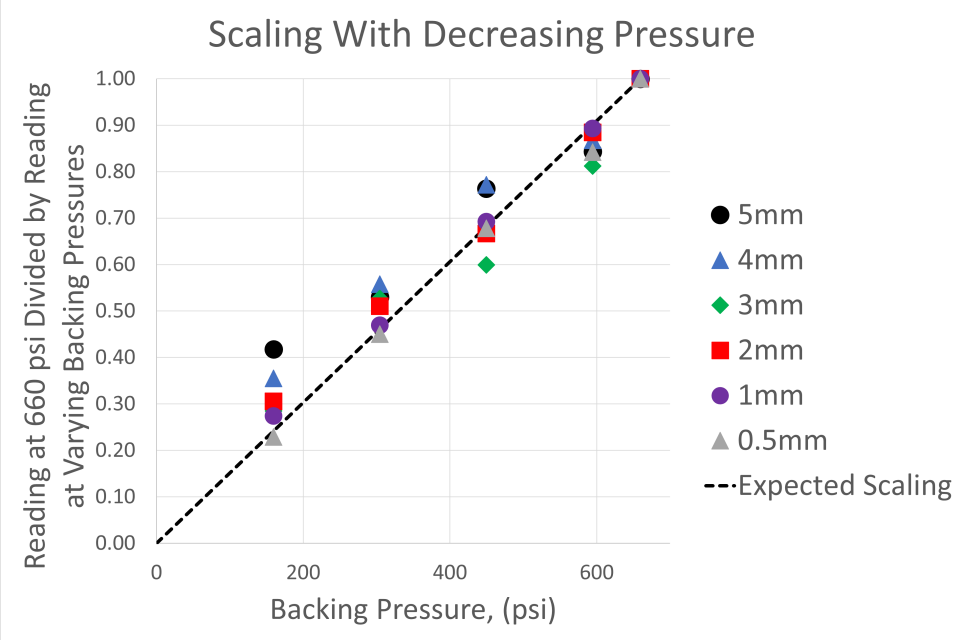

Figure 3.15: Comparison between 660 psia divided by varying pressures and the interferometry reading at 660 psia divided by the reading at varying pressures. The dotted line is the expected scaling and the individual data points are from the central point of different lineouts.

The lineouts at 0.5 mm are in close agreement with linear scaling, with some divergence at the 580 psia point. Other points however diverge from the calculated value more, with the points further from the nozzle diverging the most. This shows that linear scaling is accurate when close to the nozzle but further from the nozzle more differences in the flow emerge.

3.4 Comparison Between CLPU and University of Alberta Interferometry

Interferometry at the CLPU was conducted with a larger field of view than the interferometry at the University of Alberta but provides similar data. Similar density contours were seen in both figures 3.7a and 3.11 when the vibration effects were ignored, but there is some difference in peak density. Figure 3.7b shows a plot of the peak density at the CLPU, with values between 1.3 and 1.5×10^{18} molecules/cm^3 for a backing pressure of 50 bar. Meanwhile figure 3.13 obtains a peak density 0.5 mm above the nozzle exit of 1.68×10^{18} molecules/cm^3 for a backing pressure of 44 bar. The interferometry conducted at the University of Alberta is therefore achieving a slightly higher peak density despite having a slightly lower backing pressure when compared with the CLPU interferometry. This discrepancy may be due to several factors including different algorithmic techniques used to analyze the data, vibrations during the interferometry, and the use of an ultraviolet laser lending higher accuracy to the University of Alberta interferometry. Regardless, the difference between the two sets of data is not especially large. This pro-

vides confidence that the interferometry of both studies are correct and that matching the simulation data to the University of Alberta interferometry provides a reasonable estimate of the actual gas density during the CLPU experiment.

3.5 3D Fluent Simulation

The 2D simulations shown so far are useful for matching with the interferometry. However, during experiments, the beam will be passing transversely through the nozzle rather than longitudinally which is what the interferometry/simulations have examined thus far. In order to obtain an understanding of the gas profile seen by the beam, 3D simulations must be run instead. The volume plot of the 3D simulation is shown in figure 3.16. The memory requirements for a 3D mesh in Fluent are quite high so the 3D simulation used a more coarse mesh and took advantage of symmetry to reduce the simulation size. The converging section was also removed in the 3D model as Fluent had difficulty running the simulation with this section. Instead the throat was treated as an inlet with the full backing pressure of 740 psia and a velocity of Mach 1. Doing so caused the density profile to be much greater than it should be so scaling of the resultant density was used to correct for this.

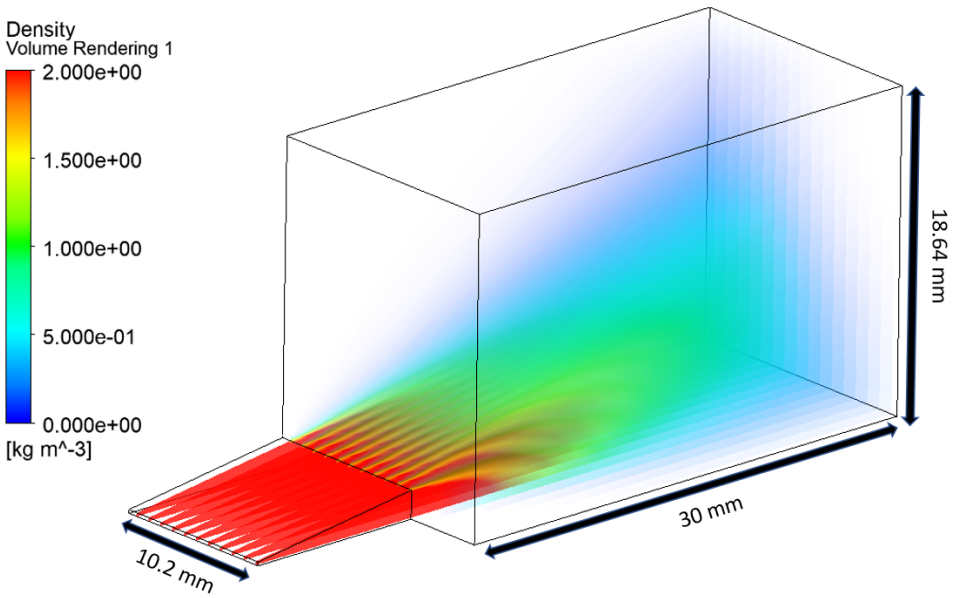

Figure 3.16: Pressure profile of the 3D nozzle model calculated for argon gas. Backing pressure of 740 psia used for the simulation.

3.5.1 3D Model Scaling

Since the 2D simulation is able to match up well with the interferometry data when given a scaling factor, the 3D model can be similarly scaled to give an estimate of the gas density profile seen by the beam. Because the 2D model has already been scaled to the interferometry data, scaling the 3D model to the 2D model will also scale the 3D model

to the interferometry data. First the density integrated across the length of the 3D nozzle must be taken so that it can be compared to the 2D simulation and interferometry data. This gives the result seen on the left of figure 3.17. While it shares the same general shape as the 2D simulation, much of the fine detail has been lost due to the coarseness of the mesh as can be seen in the comparison on the right. The image on the right shows lineouts of the gas density 0.5 mm above the nozzle for the interferometry, the 2D and the 3D simulation. The 3D lineout here has been scaled down by a factor of 50 to match the 2D model which itself is scaled to the interferometry data at 657 psia, 20 ms delay. As mentioned before, the lack of a converging section allows for a higher density to be achieved in the simulation which is why a larger scaling factor is required.

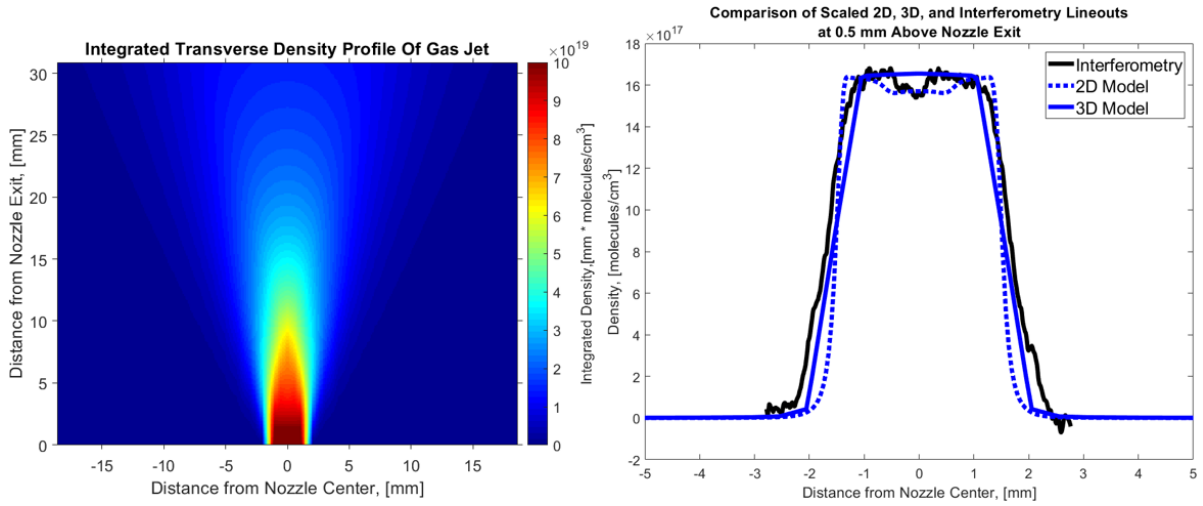

Figure 3.17: Simulated 3D model density profile along the length of the nozzle (left), and lineouts of the interferometry, 2D and 3D models 0.5 mm above the nozzle exit (right). For the plot on the right the solid black line is from the interferometry, the dashed blue line is from the 2D simulation and the solid blue line is from the 3D simulation. 2D and 3D models were linearly scaled to the interferometry backing pressure of 657 psia before applying further scaling factors. The lineout of the 3D model on the right is scaled down by 50 to match the lineout of the 2D model which itself is scaled by 30 to the interferometry data (at 20 ms 657 psia).

While the unscaled density in figure 3.17 (left) achieves densities on the order of 10^{19} (molecules/cm^3), applying the scaling factor and then integrating transversely (along the beam direction) provides the plot shown on the left of figure 3.18 showing integrated densities on the order of 10^{18} mm$*$(molecules/cm^3). The plot on the right of figure 3.18 shows an example of the beam-path alone integrated through the gas jet. Isolating this region allows the average integrated density experienced by the beam to be determined. This will be used when estimating the gas density profile seen by the beam in chapter 4.

The coarseness of the mesh obscures much of the fine detail here but the left image of figure 3.18 shows that there is a high density region being generated on the edges of the gas jet in the gas density profile seen by the beam. This leads to a relative plateau of density in the center, a high density rise on either edge, and then a sharp fall off as the gas enters a low density region. As distance from the nozzle exit increases the gas spreads out more and the high density regions move inward but due to the size of the gas

jet in this direction, the plateau region is maintained for much longer than it is on the other profile.

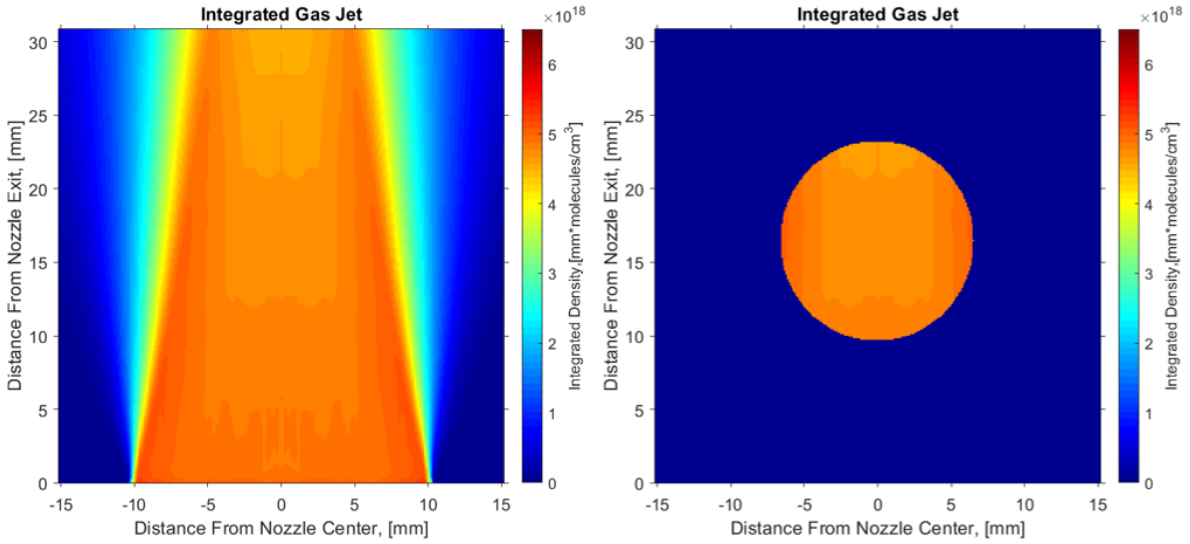

Figure 3.18: Simulated 3D model density profile integrated transversely in the beam direction for the full gas jet (left) and the beam only (right). 3D data scaled to 657 psia backing pressure, 20 ms delay with a nozzle distance from laser axis of 16 mm, and nozzle distance from laser focus of 150 mm.

From the 3D simulation the beam can be integrated through the simulated gas jet to obtain the density-distance product for the measurements. Taking the average density-distance product within the beam from figure 3.18 for varying different backing pressures provides the result shown on the right of figure 3.19. The simulations and interferometry predict a linear increase in operating pressure with an increase in backing pressure which is why this plot is a perfectly straight line. While the density distance product is useful it is not immediately clear what effect it will have on the HHG generation. Instead it is useful to compare it to figure 2.11, which predicts maximum conversion efficiency for a distance-pressure product of 37.5 mm-mbar [11]. This plot is given in terms of pressure but is derived from the phase matching equations which are dependent on density rather than pressure. However, when taking pressure directly from the simulation the changes in temperature will also affect the pressure. To avoid this issue the system can be taken as isothermal at 300 K and the density can be converted directly to pressure. This results in the image on the left of figure 3.19 and will be compared to experimental data in section 4.8.2.

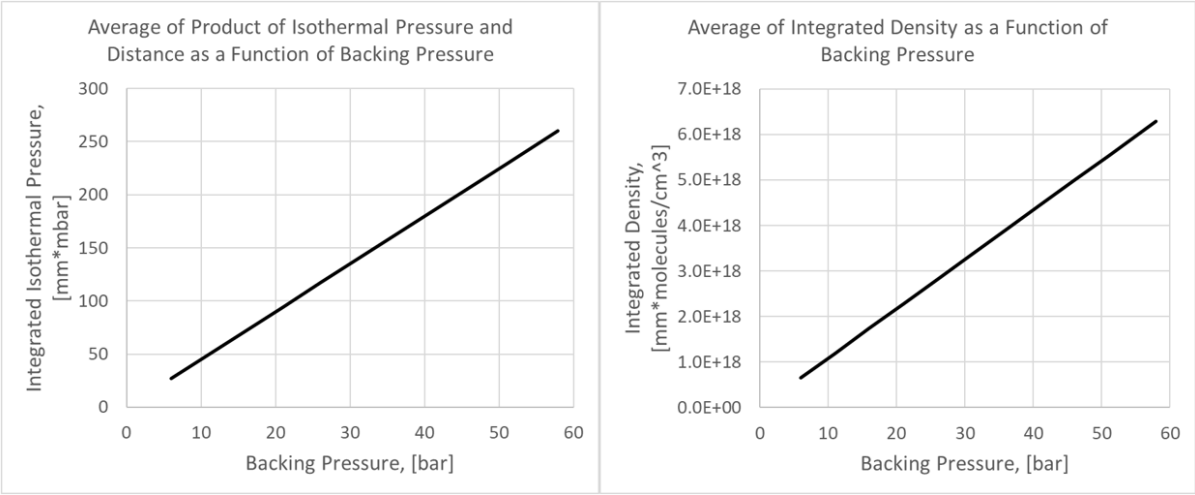

Figure 3.19: 3D simulation, average integrated density seen by the beam for varying different backing pressures (left), and average integrated isothermal pressure seen by the beam for varying different backing pressures (right). With a nozzle distance from laser axis of 10 mm and a nozzle distance from laser focus of 90 mm. 3D simulation scaled to interferomery with 657 psia backing pressure, 20 ms delay.

3.5.2 Discussion

In this chapter the gas nozzle used during the CLPU experiment was introduced. Simulations of this nozzle were run in ANSYS: FLUENT, validating that supersonic velocities were achieved and providing both 2D and later 3D density profiles. Interferometry tests of the nozzle were conducted at both the CLPU and the University of Alberta. While there was some variation between the two sets of interferometry, they were still in reasonable agreement predicting peak densities on the order of 10^{18} (molecules/cm^3). With reasonable confidence in the accuracy of the interferometry, the data from the University of Alberta was then compared to 2D Fluent simulations scaled by a factor of 30 to match the amplitude of the interferometry data at 657 psia, 20 ms delay. The simulations matched up well with the interferometry, providing confidence in the accuracy of the 2D simulations. With the 2D simulations grounded in reality, 3D simulations were then run and scaled down by a factor of 50 to match the scaled 2D simulations and interferometry. Due to the high memory requirement of 3D simulations in Fluent a rather coarse mesh was used for these simulations resulting in the loss of much of the fine data. However, the 3D simulation was able to provide a reasonable estimate for what the beam will see as it moves through the gas jet which will be used in chapter 4 when analyzing the CLPU data.

Chapter 4

CLPU Experiment

In order to test the concept of FCHHG an experiment was conducted using the VEGA laser at the Centro De Láseres Pulsados (CLPU) in Salamanca, Spain. This is a 1 Petawatt laser faciliy, among the most powerful in the world. Since the focal cone geometry of FCHHG requires a more powerful laser than typical HHG this facility was perfect in order to attempt to obtain high energy harmonics.

A detailed analysis of the data is carried out in this chapter including examining the spatial profile of the laser beam (section 4.3), the spectral characterization of the XUV (sections 4.4, 4.5, and 4.7), spatial characteristics of the XUV (4.5 and 4.6), and the conversion efficiency for varying parameters (section 4.8).

A number of different parameters including nozzle position (in three directions), gas pressure, laser energy, etc. can be changed between shots. These parameters will be listed as: [Day, Shot Number(s), Laser Energy, Dazzler Setting, Pulse Length, Laser Intensity, Gas Type, Gas Pressure, Gas Jet Delay, Nozzle Offset From Laser Axis, Nozzle Distance From Laser Focus, Nozzle Transverse Position, Object In Beam] with any other factors listed separately.

4.1 Experiment Layout

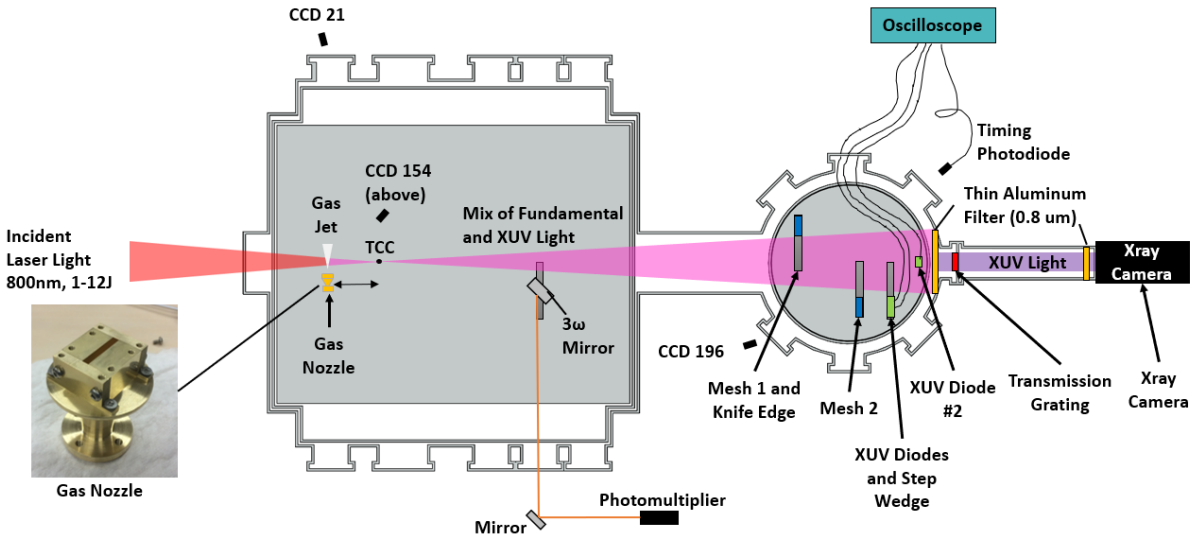

Figure 4.1: Layout of the CLPU Experiment. (not to scale)

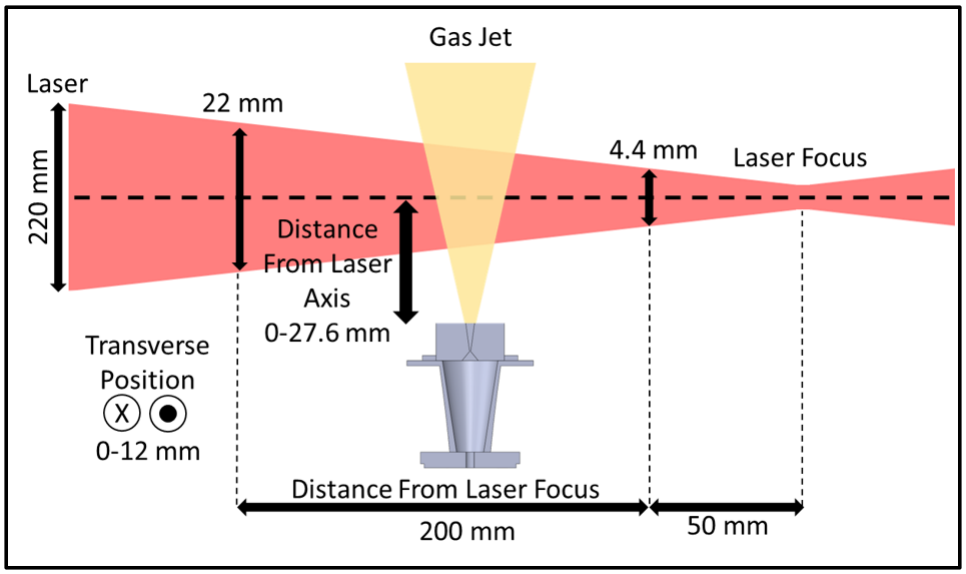

Figure 4.2: Layout of Nozzle movements

The experiment was layed out as shown in figure 4.1. The experiment was setup in the VEGA-3 vacuum chamber however, due to concerns about the intensity of the beam, most of the diagnostics were placed in a secondary chamber further away from laser focus. There were two main types of detectors for the XUV. Three XUV diodes [39] and an X-ray camera (A Sophia XO camera from Teledyne Princeton Instruments with pixel sizes of 15 um) [40] which was placed even further away down an extended channel. Thin aluminum filters were used to block the intense laser light and prevent it from entering the diagnostics such as the XUV diodes and X-ray camera. Al filters allow for some transmission at the shorter wavelengths of XUV (17-70 nm) which HHG would produce

but completely block the fundamental laser light and much of the lower energy harmonics. The camera and XUV diodes had Al filters placed just in front of their sensors and another Al filter was placed in the chamber blocking the entrance to the camera mounting tube. In the VEGA-3 chamber the laser enters, from an OAP mirror, and focuses down onto target chamber center (TCC). Our nozzle is placed prior to focus so that the partially focused beam is able to interact with our gas jet to produce the focal cone harmonics. The nozzle has three translation stages allowing three dimensional movement, as shown in figure 4.2. These three dimensions were nozzle distance from the beam axis (0-27.6 mm), nozzle distance from laser focus (50-200 mm), and the transverse direction to move the beam across the length of the nozzle (0-12 mm). Moving the nozzle in relation to the laser focus will in turn affect the size of the beam at the position of the nozzle as shown in figure 4.3. Two CCD cameras, viewing the nozzle from above and to the side, are used to record what occurs at the gas jet. After focus a pick-off mirror on a motorized mount can be moved into the beampath in order to steer light into a photomultiplier [41] set for detecting the third harmonic. This is used as a diagnostic for the gas jet in order to characterize the interaction region. In the secondary chamber perforated meshes, a knife edge, XUV diodes, and a step wedge are located. The perforated meshes are for use in shadowgraphic imaging onto the X-ray camera in order to determine the size and divergence of the beam and, by back projection, determine where it is originating from. Fresnel diffraction can also be used with the knife edge in order to determine the size of the beam source and the wavelength. The step wedge consists of a region with 0, 1, and 2 layers of 0.8 um Al filter and is used as a check on the spectrum of generated light. The XUV diodes are in special mounts and protected with aluminum filters to only allow XUV light in and are used as a metric for the intensity of XUV light from the HHG process. Before entering into the extension holding the x-ray camera the light will pass through a larger aluminum filter so that only XUV light reaches the camera. There is also a small slit transmission grating which can be placed just after the large filter in order to examine the spectral characteristics of the XUV light.

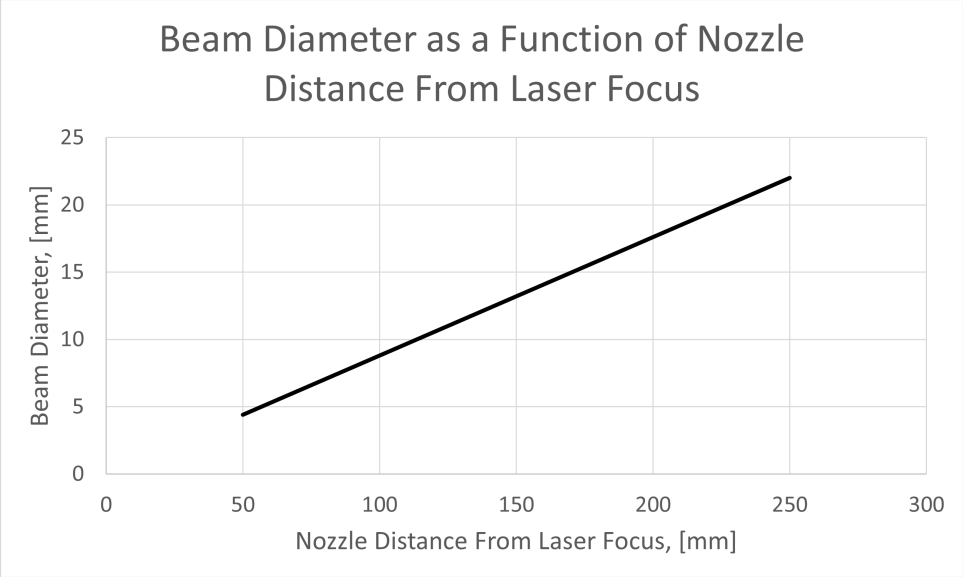

Figure 4.3: Relationship between beam diameter and distance from the nozzle to laser focus.

4.2 Third Harmonic Generation

Third harmonic generation was used as a means of verifying that non-linear interaction between the gas jet and laser was occuring. The process of third harmonic generation is much like second harmonic generation except it requires three photons of frequency ω to produce one photon of frequency 3ω. In this experiment third harmonic generation was used primarily as a diagnostic of the gas jet conditions. The fundamental frequency of the laser used at the CLPU is 800 nm therefore the third harmonic should be 267 nm. Two mirrors were placed after the gas jet in order to redirect the beam into a Hamamatsu solar blind photomultiplier (Model R2078) [41] connected to an oscilloscope. A 10 nm bandpass filter tuned to allow 267 nm through but not 800 nm was placed in front of the photomultiplier.

A typical example of the signal on the photomultiplier for both the gas on and the gas off is shown in figure 4.4. This data was recorded on an oscilloscope set to trigger with the laser pulse at zero seconds. The photomultiplier has virtually no response for when the gas is off reaching $<$1 mV. When the gas is on there is a noticeably larger response reaching $\sim$35 mV followed by a decay in the signal over the course of several microseconds. Due to the large difference in response between the gas on and gas off data, it can be reasonably concluded that the third harmonic is being generated.

It is also of interest to examine how the third harmonic is affected by changes in the gas jet. This was done by changing the distance between the nozzle and the beam axis as well as moving the nozzle transversely across the beam. The raw data from the photomultiplier was extremely noisy immediately after the pulse but becomes more uniform shortly after.

Therefore, the average between 3 and 4 microseconds after the laser pulse, a region outside of the noise but before the signal falls off, was chosen to represent the reading. This data was plotted for varying distances between the nozzle and the beam (figure 4.5), and for varying positions of the nozzle in the transverse direction (figure 4.6). Varying the distances between the nozzle and the beam shows that the signal oscillates back and forth quite a bit but overall has a slow downward trend. As the nozzle draws further away from the beam, the gas will expand further and further. Since the integrated density that the beam sees will stay largely the same a very steep slope is not expected. There should be some slope however since some of the gas will expand outside of the region where it will interact with the beam therefore reducing the integrated density. Therefore, the general trends seen here match up with expected data. Even without moving the nozzle there are noticeable difference between shots at the same position, these may have added up to create these oscillations.

Varying the position of the nozzle in the transverse direction shows that the third harmonic generation falls off rapidly as it approaches the edge of the nozzle. There are two plots included, one where the nozzle is 4 mm from the beam axis and one where the nozzle is 10 mm from the beam axis. The nozzle is centered at a vertical position of 4mm, although most shots were done at 8mm. Based on the results seen in this plot however, it is believed that this was slightly misaligned and the actual center is somewhere between 8 and 12mm. It is expected based on simulations that there will be a shock coming from the sides of the nozzle which results in a high density region along the edge of the density profile. The decrease in the center points further from the nozzle and the edge points being higher is consistent with the gas spreading out more and more as the distance between the nozzle and the beam increases.

The third harmonic was able to verify that the beam is hitting the gas jet and has provided limited data on the gas density profile generated by the gas jet.

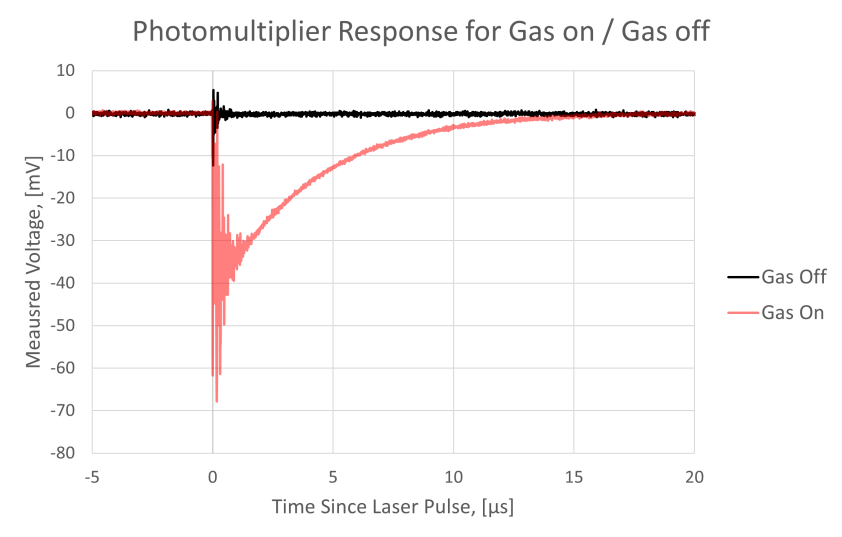

Figure 4.4: Comparison of photomultiplier response for gas on and gas off. The red line is for gas on: [2022-02-07, Shots 60-62, 1 J, 790 fs^2, Not Recorded, Not Recorded, Argon, 21 bar, 24 ms, 8 mm, 50 mm, 8 mm, 3w mirror], and the black line is for gas off: [2022-02-07, Shots 15-17, 1 J, 390 fs^2, Not Recorded, Not Recorded, Argon, off, 5.1 ms, 4 mm, 50 mm, 8 mm, 3w mirror]

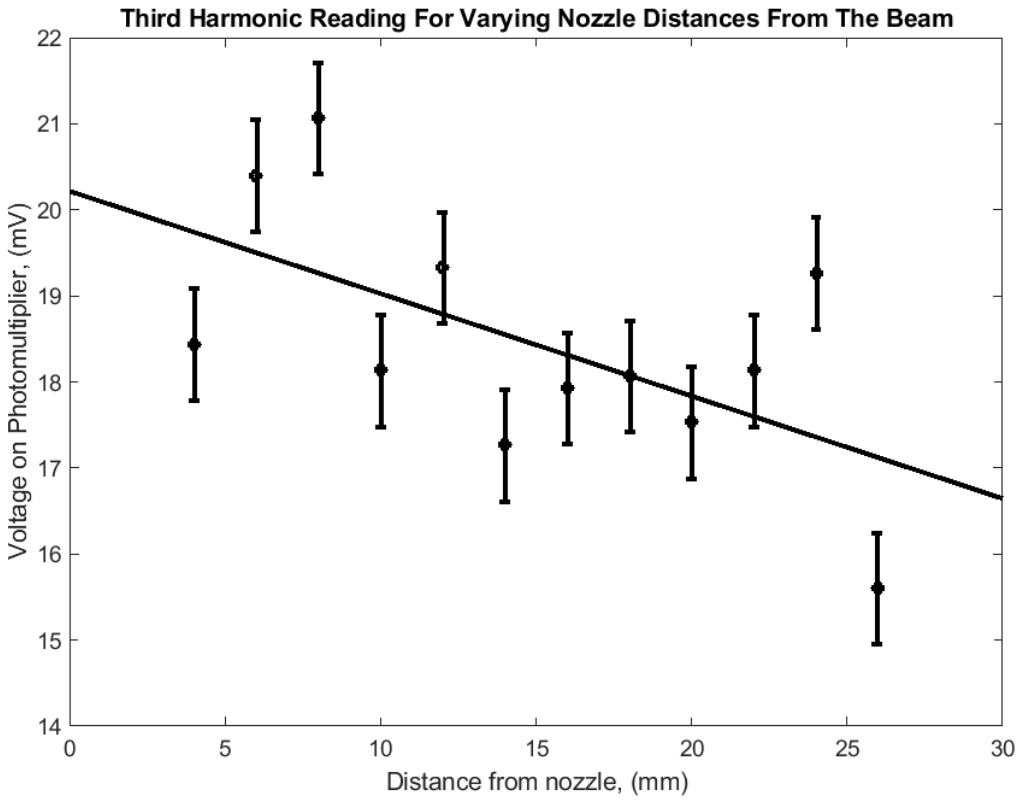

Figure 4.5: Photomultiplier reading for varying distances between nozzle and beam. The solid line is a linear fit to the data. [2022-02-07, Shots 54-85 and 89-91 and 104-106 with background 14-16, 1 J, 790 fs^2, Not Recorded, Not Recorded, Argon, 21 bar, 24 ms, Varying, 50 mm, 8 mm, 3w mirror]

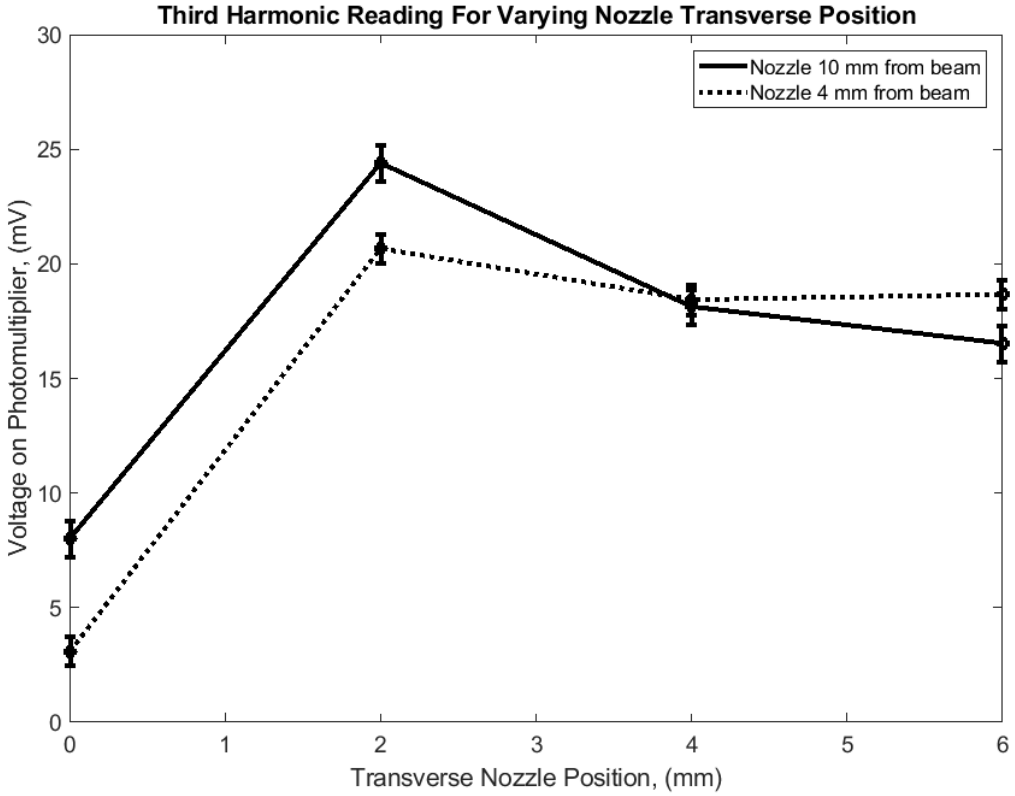

Figure 4.6: Photomultiplier reading for varying the position of the nozzle in the vertical direction while the distance between the nozzle and the beam is 4 mm and 10 mm. The solid line is when the nozzle is 10 mm from the beam axis and the dotted line is when the nozzle is 4 mm from the beam. [2022-02-07, Shots 54-55 and 62-64 and 89-112, 1 J, 790 fs^2, Not Recorded, Not Recorded, Argon, 21 bar, 24 ms, 4 and 10 mm, 50 mm, Varying, 3w mirror]

4.3 Beam Profile Modulations

Examples of the XUV images recorded by the X-ray camera are shown in figure 4.7. The beam passes through an aluminum filter held in place by a circular frame resulting in the cut-circle shape on the two sides. There is also some debris on the camera resulting in a few darker spots within the image itself. Beyond that however the beam appears to consist of many bright and dark spots. Moreover, there appears to be interference patterns between the bright spots suggesting that each of these beams is its own coherent light source. The right of figure 4.7 is the average of five shots and shows that the shape remains quite consistent even to the point where the interference patterns are well preserved when averaging. The source of these bright spots was not immediately clear and was theorized to have come from several different sources. It was first theorized that damage on the camera or variations in the aluminum filter could have caused this. Another explanation was that this was due variations in the gas density profile produced by the gas jet, or that it was modulation in the beam intensity profile due to something further upstream in the beam.

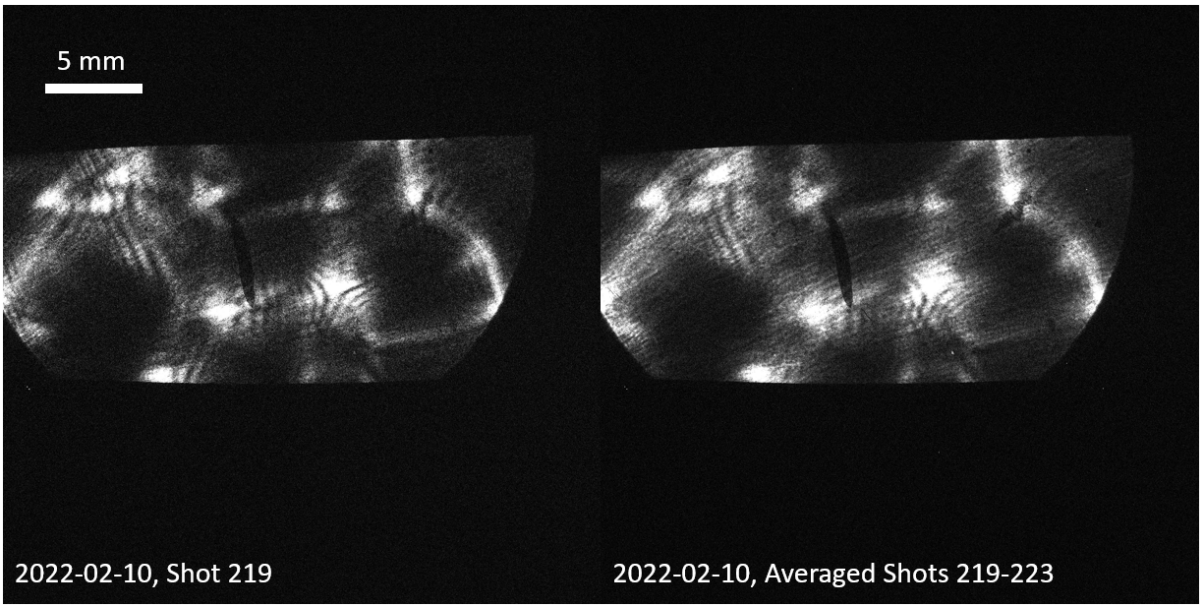

Figure 4.7: Modulated beam profile for shot 219 on 2022-02-10 on Sophia X-ray camera (left), and Averaged of shots 219-223 on 2022-02-10 on Sophia X-ray camera (right) [2022-02-10, Shots 219-223, 4 J, 800 fs^2, 41.1 fs, $2.2 \times 10^{14} W/cm^2$, Argon, 31 bar, 22 ms, 10 mm, 90 mm, 8 mm, Nothing]

In order to investigate this the Sophia X-ray camera was replaced with an Andor X-ray camera and the aluminum filter replaced with a new one. Figure 4.8 shows that this did not change the image and that the spotty beam modulation was still present. After this the Sophia X-ray camera was reinstalled. A camera mounted to look at the gas nozzle from the top imaged striations occuring through the gas jet as shown in figure 4.9. This indicates that beam modulation is present at the gas jet likely due to intensity modulations in the laser beam itself. These could lead to non-uniformities observed in the XUV.

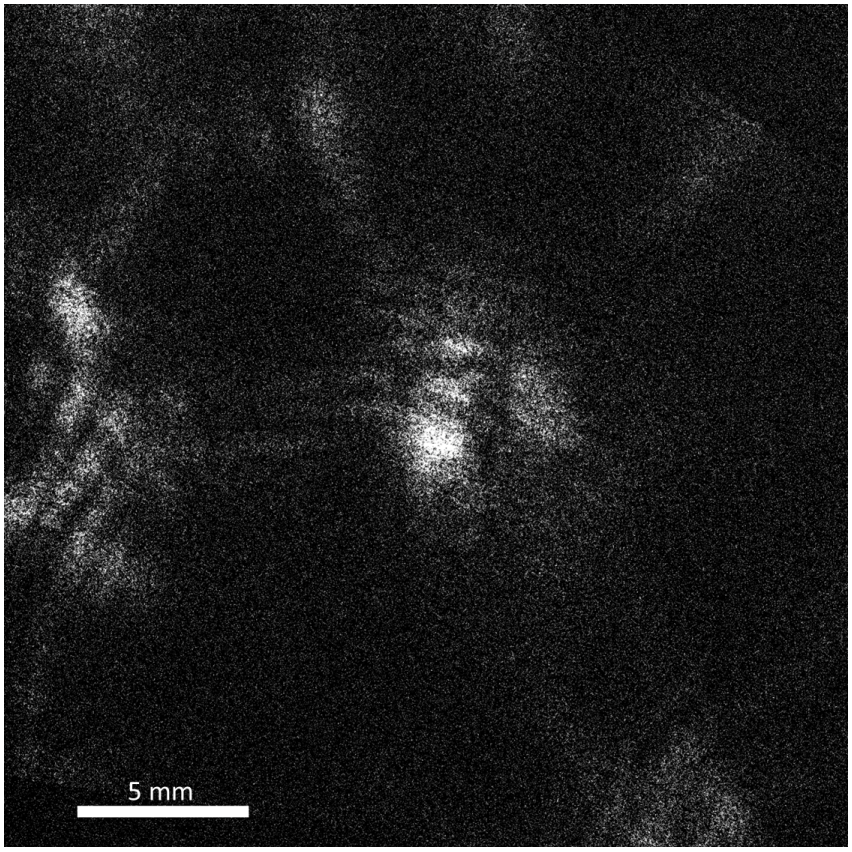

Figure 4.8: Modulated beam profile on Andor Camera. [2022-02-14, Shot 37, 4.22 J, 1000 fs^2, 85.1 fs, $1.27 \times 10^{14} W/cm^2$, Argon, 31 bar, 22 ms, 5 mm, 80 mm, 8 mm, Nothing]

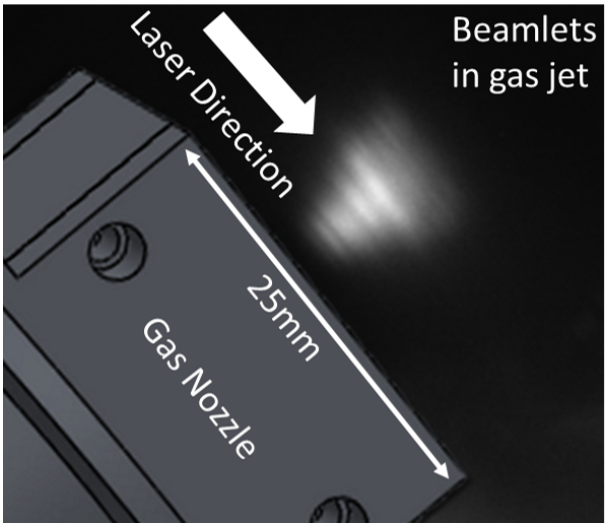

Figure 4.9: Striations occuring in the plasma formed at the gas jet, a Solidworks model is used to represent the gas jet due to poor lighting. [2022-02-23, Shot 9, 12.05 J, 600 fs^2, 61.7 fs, $1.9 \times 10^{14} W/cm^2$, Argon, 46 bar, 22 ms, 8 mm, 130 mm, 8 mm, Grating]

The gas nozzle was also moved in relation to the beam axis. If the modulations occuring in the beam profile were due to modulations in the gas density profile they should change as the gas nozzle is moved. The results are shown in the upper half of figure 4.10. While this did affect the intensity of light reaching the CCD the overall

profile remained largely unchanged indicating that this modulation was not due to the gas jet. In a similar fashion the dependency on the nozzle distance from laser focus was studied. The results are shown in the lower half of figure 4.10 indicating that varying the nozzle distance from laser focus does affect the presence of beam modulation. The results are consistent with the modulation coming from further upstream in the beam, as the existing modulation in the beam would interact with the gas jet at different positions resulting in the modulation of the XUV light.

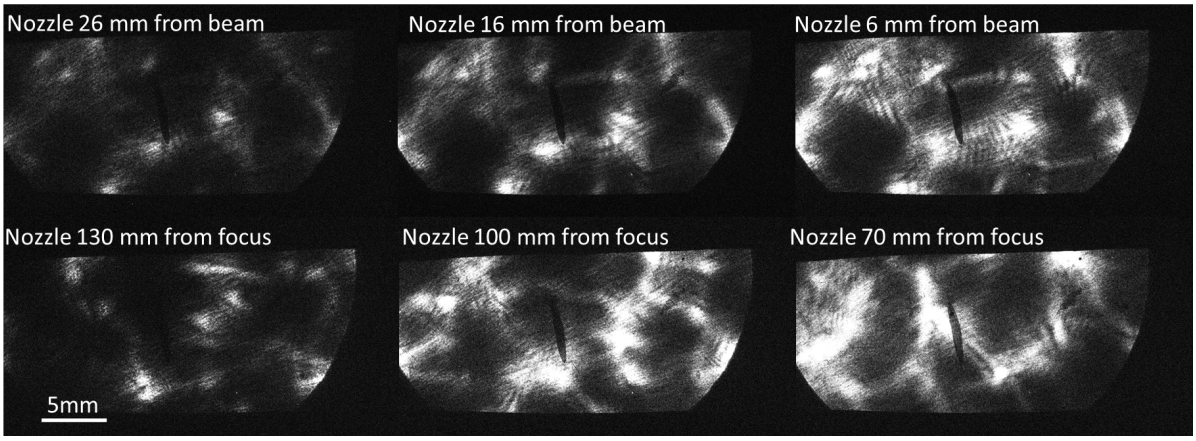

Figure 4.10: Comparison of averaged beam profiles for nozzle distances from beam of 26 mm, 16 mm, and 6 mm from the beam (top) [2022-02-10, Shots 190-218, 4 J, 800 fs^2, Ave 43.5 fs, Ave $2.2 \times 10^{14} W/cm^2$, Argon, 31 bar, 22 ms, Varying, 90 mm, 8 mm, Nothing], and comparison of averaged beam profiles for nozzle distances from focus of 130 mm, 100 mm, and 180 mm from focus (bottom) [2022-02-10, Shots 129-147, 4 J, 800 fs^2, Ave 39 fs, Ave $1.8 \times 10^{14} W/cm^2$, Argon, 31 bar, 22 ms, 10 mm, Varying, 8 mm, Nothing]

Since all signs were pointing towards the modulation occuring further upstream in the laser the off axis parabola used to focus the beam had its angle changed with the results shown in figure 4.11. From this it can be seen that the patterns of the beam modulation move as the angle is changed in both a vertical and horizontal direction allowing us to conclude that this beam modulation is occuring further upstream in the laser. Additionally, a metal plate used in a previous experiment to block the beam was found to have a similar modulation pattern as seen in figure 4.12.

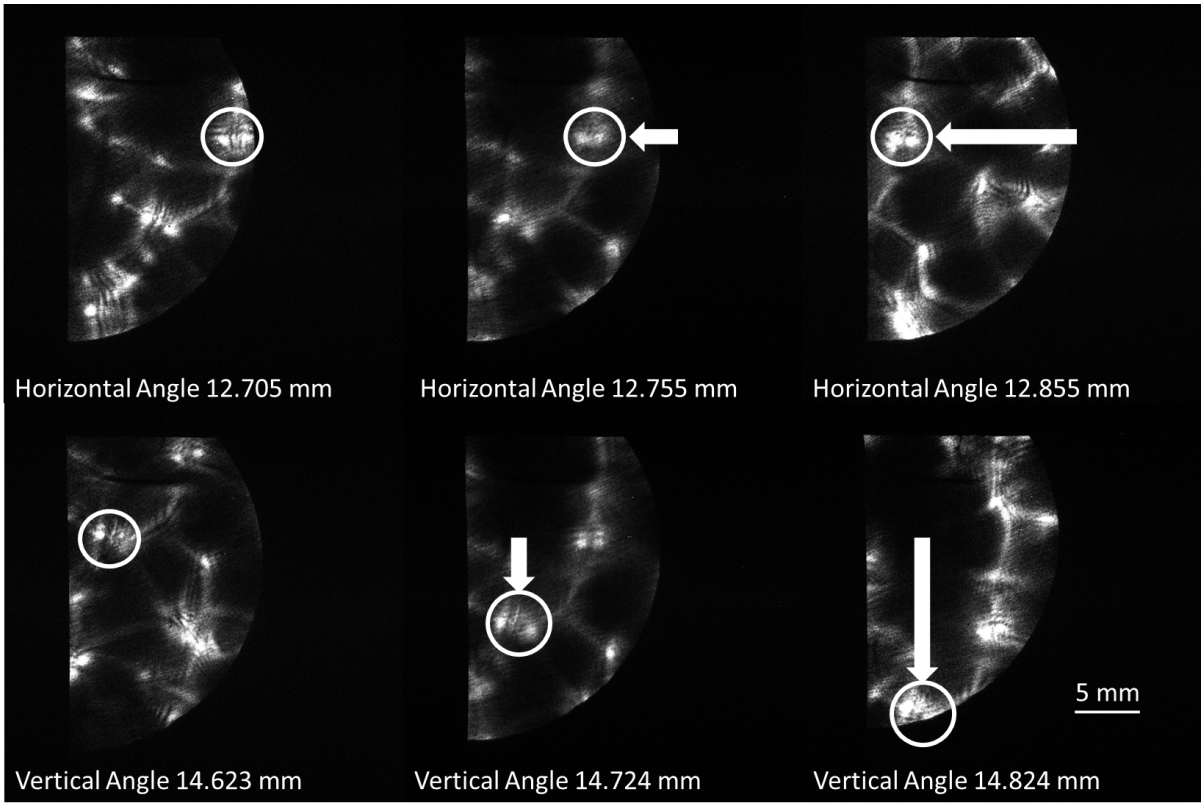

Figure 4.11: Varying the horizontal angle on the off axis parabola (top) [2022-02-15, Shots 63-78, 8 J, 1000 fs^2, Ave 50 fs, Ave $1.8 \times 10^{14} W/cm^2$, Argon, 36 bar, 22 ms, 8 mm, 130 mm, 8 mm, Nothing], and varying the vertical angle on the off axis parabola (bottom) [2022-02-15, Shots 49-64, 8 J, 1000 fs^2, Ave 54 fs, Ave $1.5 \times 10^{14} W/cm^2$, Argon, 36 bar, 22 ms, 8 mm, 130 mm, 8 mm, Nothing]

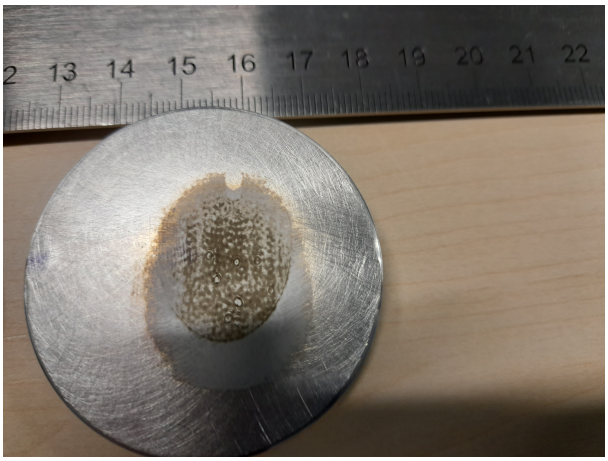

Figure 4.12: Burns on a metal plate used in a previous experiment to block the beam. Modulation of the pattern can be seen.

It is not ideal for this much modulation to be occuring. However, due to it's reproducibility, the data collected can still be used for analysis.

4.4 Spectral Characterization

Since some radiation is able to pass through the aluminum filters placed in front of the diodes and camera it is clear that XUV light is being generated. However, it is not yet known if this is due to HHG or simply plasma emission. In order to determine whether high-order harmonics were being generated a transmission grating with 500 lines/mm was placed $69.25 \pm 1cm$ from the camera, just past the aluminum filter at the exit of the second chamber. This distance allowed for enough angular separation that individual harmonics should be visible. Only the zeroth and M+1 orders were visible on the camera resulting in the image seen in figure 4.13. In order to ensure adequate brightness in the spectra measured the grating used was quite wide. This combined with the distance between the grating and the camera means that there will be overlap in the spectra of harmonics which are generated. However, the spatial modulation of the beam in some shots is helpful in this respect. Figure 4.15 shows a beam modulation with a bright spot lined right up along the edge of the grating creating a single bright line. This bright line then goes on to create a series of bright lines for the resulting spectra (brightness adjusted) that can be distinguished from one another. If the entire grating spot had been filled with bright light the resulting spectra would overlap with each other and have become difficult to distinguish. Thus the modulation helps to distinguish one spectral line from another greatly aiding in analysis.

On the left of this figure the bright zeroth order spectral line can be seen. To the right, after a dark region, is then a second bright line followed by a spread of less bright lines which make up the M+1 spectra. This initial dark region is due to the harmonics reaching the cutoff energy in conjunction with absorption by the aluminum filter at these higher wavelengths (discussed more later). The single bright line at the shortest wavelength is very interesting. In figure 4.14 where the laser has a lower intensity, the line is entirely gone. What can be assumed from this is that part of the argon gas has been fully ionized leading to the formation of a plasma with weak emission. Additionally, the line consists of regions where it is much brighter than others indicating that the beam modulation is having an effect on the formation of this plasma. The spread of less bright light then has the characteristics of typical high harmonic generation. In several places there appear to be peaks and valleys consistent with a series of harmonics. In fact these also occur on the bright line and, using figure 4.14 as a reference, it appears that the bright line is helping to significantly expand the harmonic series. Moving further past the spread of what appear to be harmonics is a large dark region but after this very faint patches of light can be seen in certain places indicating that there is some spectra at longer wavelengths as well.

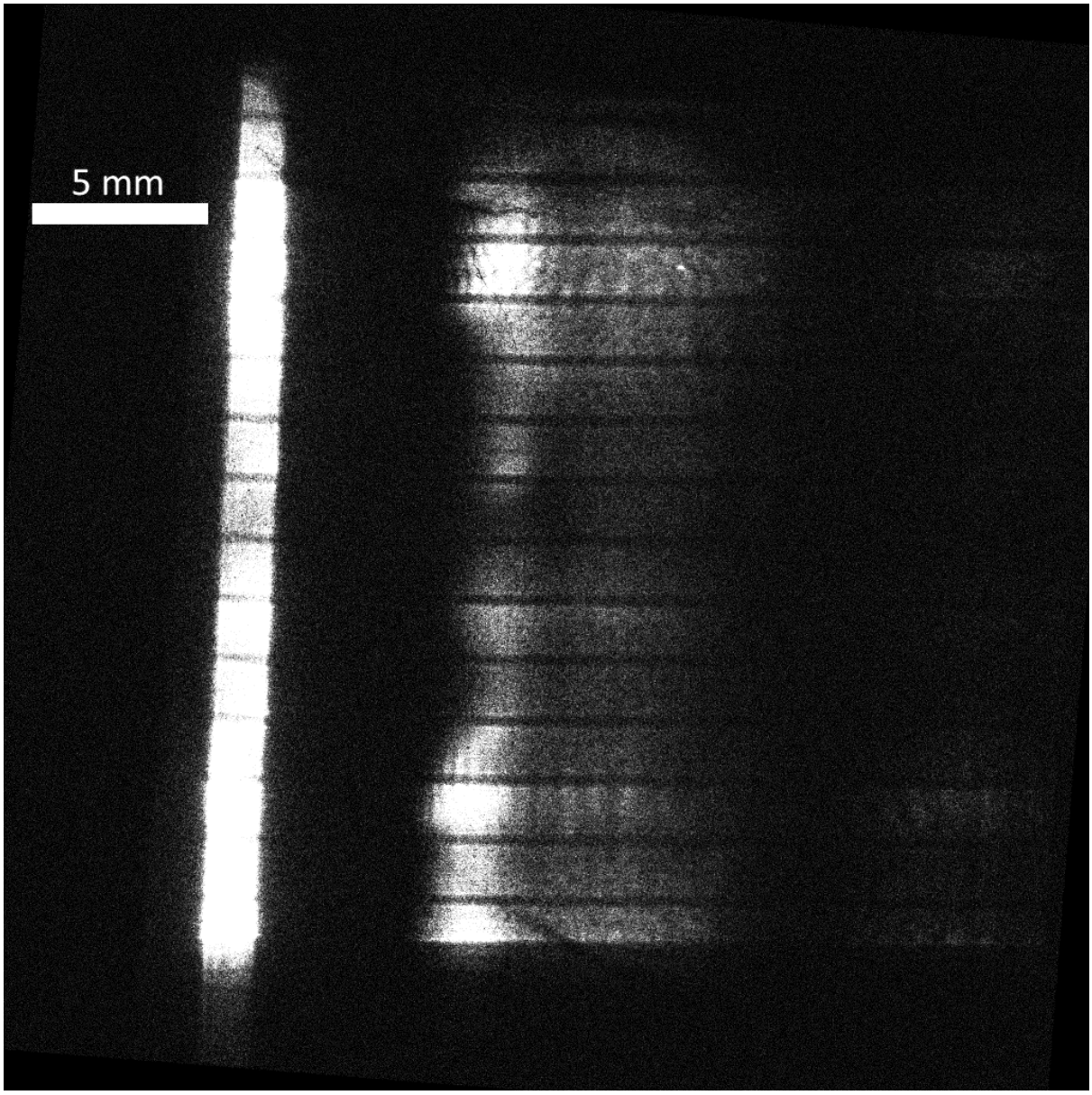

Figure 4.13: Spectra from argon gas. The bright zero order is seen on the left and the harmonic spectrum is dispersed to the right. A bright plasma line is present at the shortest wavelengths. [2022-02-23, Shot 20, 11.89 J, 600 fs^2, 72 fs, $1.6 \times 10^{14} W/cm^2$, Argon, 46 bar, 22 ms, 8 mm, 130 mm, 8 mm, Grating]

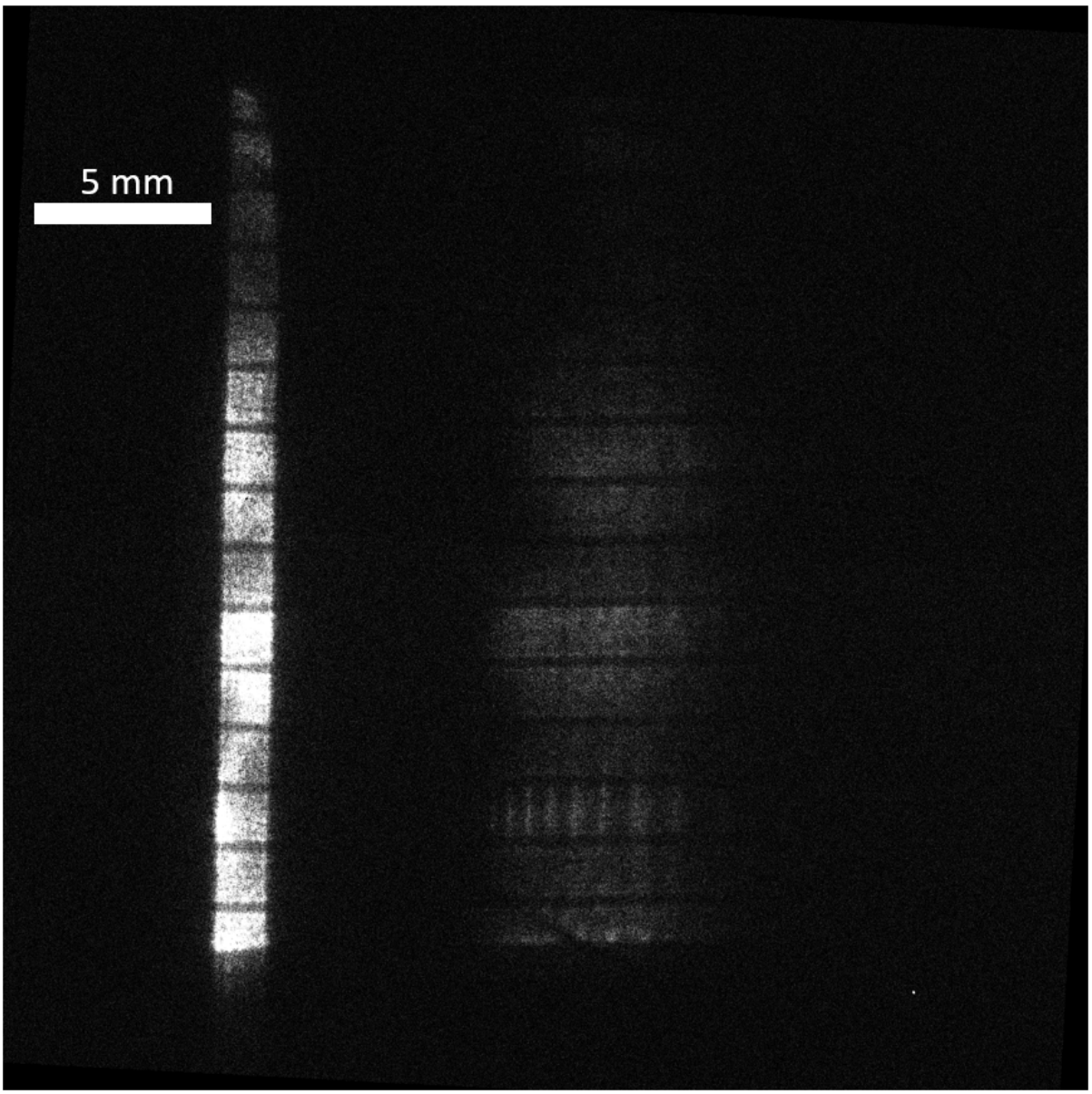

Figure 4.14: Spectra from Argon gas. The bright zero order is seen on the left and the harmonic spectrum is dispersed to the right. No bright plasma line is present. [2022-02-22, Shot 27, 8 J, 1200 fs^2, 95.2 fs, $1.4 \times 10^{14} W/cm^2$, Argon, 46 bar, 22 ms, 6 mm, 100 mm, 8 mm, Grating]

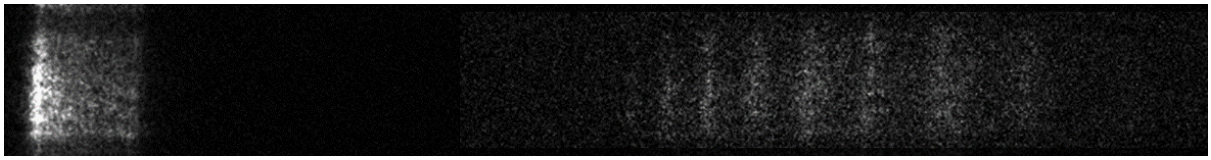

Figure 4.15: The effect of beam spatial modulation on the measured spectra, image composite from two different brightnesses of the same image superimposed on eachother. A bright emission is present only on the left side of the grating slit leading to easily distinguished harmonics. [2022-02-22, Shot 27, 8 J, 1200 fs^2, 95.2 fs, $1.4 \times 10^{14} W/cm^2$, Argon, 46 bar, 22 ms, 6 mm, 100 mm, 8 mm, Grating]

4.4.1 Wavelength Calculation

To analyze the spectra, lineouts of regions that appeared to represent the harmonics particularly well were taken. In order to calculate the wavelength of each spectral line

the distance from the zeroth order must be used. The pixel count of the camera was converted into microns with each pixel corresponding to 15 microns. Equation 4.1 was then used to calculate the wavelength at each point along the lineout.

$$\lambda = \frac{sin(arctan(\frac{x - x_{zero}}{d_{grating}}))}{lines/mm} \tag{4.1}$$

Here λ is the wavelength, x_{zero} the pixel position converted into microns of the zeroth order, x the pixel position converted into microns for any point on the lineout, $d_{grating}$ the distance from the transmission grating to CCD (measured as $69.25 \pm 1cm$), and $lines/mm$ the number of lines per millimeter in the grating which was 500. This equation is very straightforward to use when having either a point source or uniformly illuminated zeroth order where the value of x_{zero} is easy to calculate. Unfortunately due to the spatial modulation our zeroth order was not uniform and x_{zero} could therefore be a range of values. In addition to this the measurement of the distance between the grating and the CCD was done outside of the chamber for practical reasons which lead to a greater degree of uncertainty. This resulted in the peaks of the spectra not lining up with the calculated harmonics very well. However, adjusting $d_{grating}$ to a value of 68.25 cm and moving the position of x_{zero} to the peak on the edge of the zeroth order rather than the zeroth order centroid, showed that the harmonics could line up perfectly as seen in figures 4.16 and 4.17. The positioning of x_{zero} on the peak makes sense for these lineouts as they were chosen due to presence of a sharp peak on the edge of the zeroth order allowing for easily distinguished harmonics as seen in figure 4.15. The adjustment to $d_{grating}$ is within the estimated measurement error and with the agreement to calculated harmonics seen in figures 4.16 and 4.17 it is reasonable to make this adjustment.

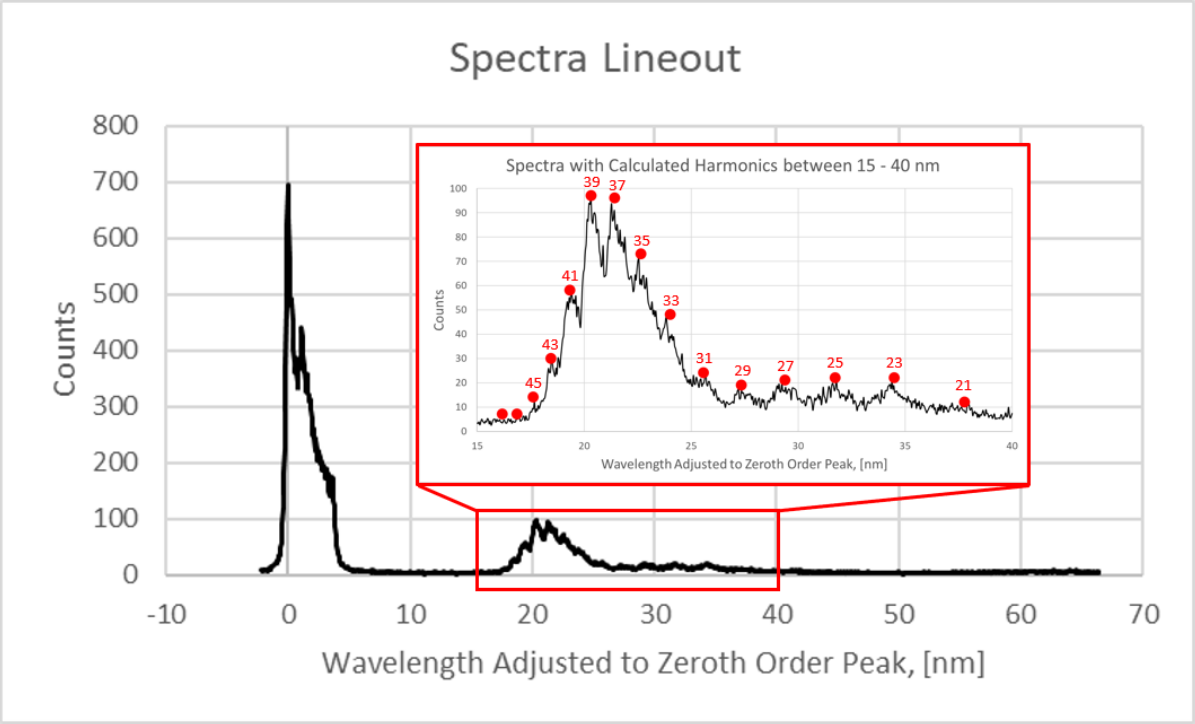

Figure 4.16: Lineout displaying both the zeroth and M+1 orders, the M+1 order is blown up and calculated harmonics (red circles) are shown lining up with the peaks. [2022-02-23, Shot 20, 11.89 J, 600 fs^2, 72 fs, $1.6 \times 10^{14} W/cm^2$, Argon, 46 bar, 22 ms, 8 mm, 130 mm, 8 mm, Grating]

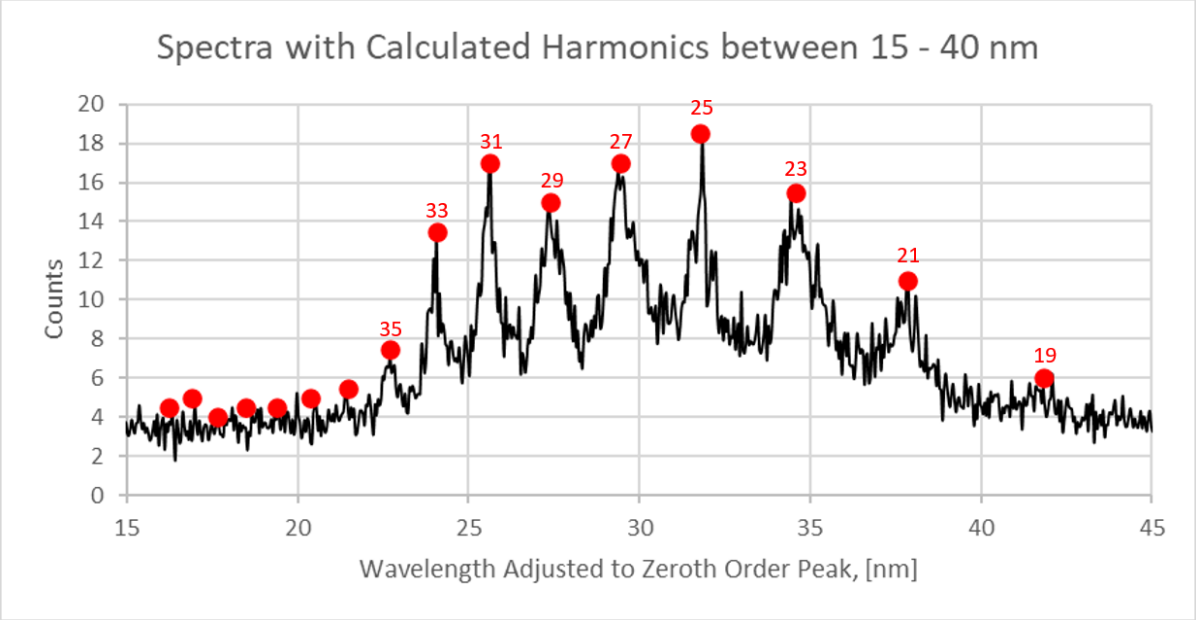

Figure 4.17: Lineout displaying the M+1 order showing that the calculated harmonics (red circles) line up well with the peaks of the data. [2022-02-22, Shot 27, 8 J, 1200 fs^2, 95.2 fs, $1.4 \times 10^{14} W/cm^2$, Argon, 46 bar, 22 ms, 6 mm, 100 mm, 8 mm, Grating]

4.4.2 Scaling with Intensity

The energy of the laser, the size of the beam at the interaction point with the gas jet, and the pulse-length all work together to determine the intensity of the beam interacting

with the gas jet. In order to determine the effects of different intensities on the spectra a scan of the dazzler was conducted which resulted in a varying pulse-length. The dazzler is part of the compressor system in the laser and allows for control of the linear dispersion component of the Gaussian pulse dispersion. This allows for control over the average pulse length of the laser, although there is still some variation between each shot. Pulse lengths are determined from the data collected by an autocorrelator placed outside of the chamber. There will be some difference between the measured pulse length outside of the chamber and the actual pulse length inside the chamber due to dispersion of the beam as it passes through the chamber window and the air. This difference will likely result in shorter pulse lengths and therefore higher intensities inside the chamber compared to what is measured by the autocorrelator outside. The analysis in this thesis will use the pulse length as measured by the autocorrelator.

The two spectra seen in figures 4.13 and 4.14 are from shot 20 on 2022-02-23 and shot 27 on 2022-02-22 respectively. As mentioned earlier the shot from the 22nd has a lower intensity than the shot from the 23rd. The shot from the 22nd had a laser energy of 8 J, a pulse length of 95 fs, and a beam diameter of 8.8 mm compared to the shot from the 23rd with an energy of 11.9 J, a pulse length of 70 fs, and a beam diameter of 11.4 mm. This leads to intensities of $1.4 \times 10^{14} W/cm^2$ and $1.6 \times 10^{14} W/cm^2$ respectively. Despite this relatively small difference in intensity the shot from the 23rd has a bright plasma line while there is no plasma line in the shot from the 22nd. In part this helps to highlight how sensitive the HHG process is to pulse intensity near the ionization threshold, however the higher energy of the shot from the 23rd likely plays a role as will be discussed later.

In order to investigate the effect of laser intensity on the spectra of the harmonics a series of shots at different dazzler settings was selected for examination. A compilation of these is seen in figure 4.18. Shot 4 boasts the highest intensity at $5.1 \times 10^{14} W/cm^2$ which was achieved due to a very short pulse length of 26 fs at a dazzler setting of 600 fs^2. Shots 3 and 11 are also very intense and capable of creating the bright plasma line. In shots 27 and 43 the bright plasma line dissapears but leaves a strong series of harmonics that are still visible by themselves. In shots 41 and 55 only some of the lower order harmonics from shot 27 are still visible with the higher order ones also fading out. This corresponds to the cuttoff energy being a function of intensity as seen in equations 2.4 and 2.5.

Another interesting feature is the effect that spatial modulation has on the spectra. Since the harmonic generation process is heavily reliant on intensity, it stands to reason that spatial modulations in the intensity of the driving laser will lead to spatial modulations of the spectra of generated harmonics. This can be seen in parts of the spectra shown in figure 4.18 as well as figures 4.13 and 4.14 which show that pockets of higher intensity in the zeroth order can translate to farther reaching harmonics and plasma

emission.

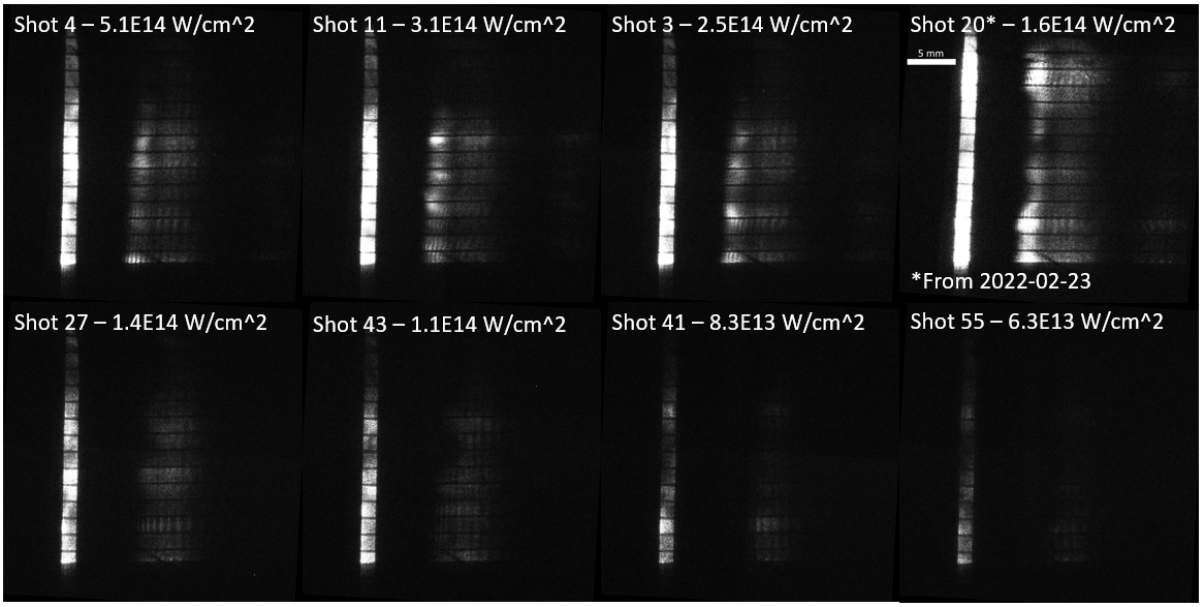

Figure 4.18: Spectra resulting from varying the dazzler settings on 2022-02-22 [2022-02-22, Shots 3,4,11,27,41,43,55, 8 J, varying, varying, varying, Argon, 46 bar, 22 ms, 6 mm, 100 mm, 8 mm, Grating] and 2022-02-23. [2022-02-23, Shot 20, 11.89 J, 600 fs^2, 72 fs, $1.6 \times 10^{14} W/cm^2$, Argon, 46 bar, 22 ms, 8 mm, 130 mm, 8 mm, Grating]

It is important to note that the intensity is very sensitive to shot-to-shot fluctuations. The laser energy will vary slightly between shots but the pulse length can have significant variations even at the same dazzler setting. For example figure 4.19 shows that two shots with the same dazzler and other settings can have quite different intensity due to variation in the pulse length, resulting in significant differences in the spectra.

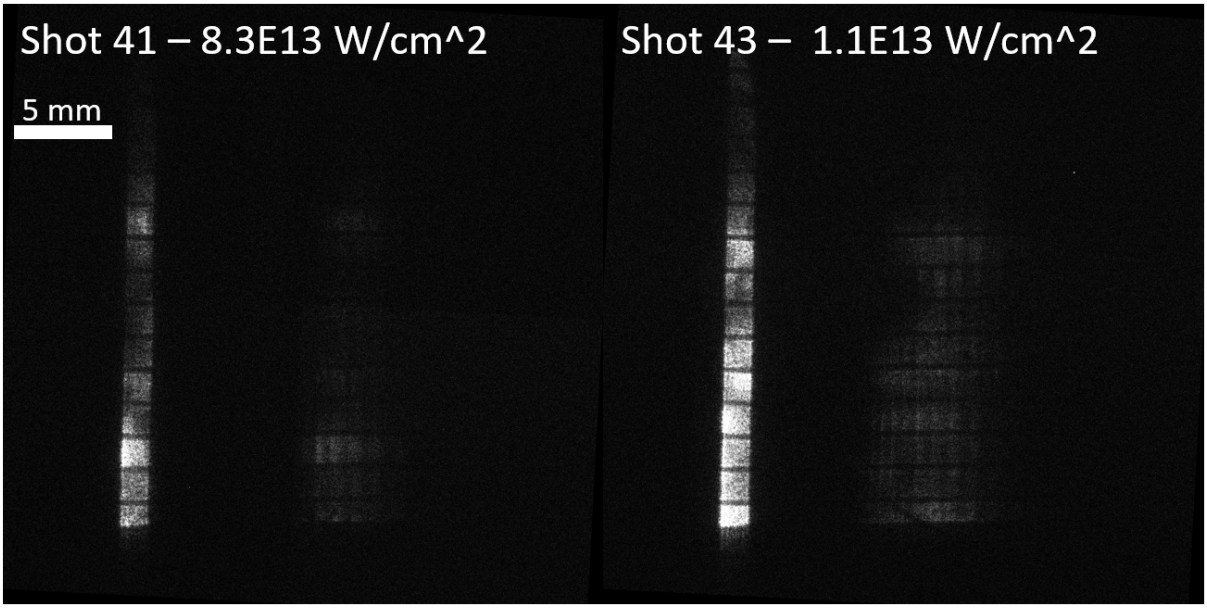

Figure 4.19: Effect of shot to shot variation for a constant dazzler setting of 1600 fs^2, shots 41 and 43 from 2022-02-22. [2022-02-22, Shots 41 and 43, 8 J, 1600 fs^2, 159 fs and 121 fs, 8.3E13 and 1.1E14 W/cm^2, Argon, 46 bar, 22 ms, 6 mm, 100 mm, 8 mm, Grating]

Lineouts from each of the spectra in figure 4.18 are shown in figure 4.20 which helps to confirm what was said previously. The shots are separated based on the range of spectra they create. The four shots intense enough to create a plasma line are at the top row, while the center has the two shots with a low enough intensity that the plasma is not generated but high enough that the higher order harmonics are able to be accessed. Lastly the bottom row has the two shots of lower intensity which are only able to create a few lower order harmonics. The estimated cutoff point for each row is represented by the vertical red lines.

Based on this it would appear that a plasma is formed for intensities between 1.4×10^{14} and $1.6 \times 10^{14} W/cm^2$. However, figure 4.21 shows that a bright plasma line is formed despite an intensity of only $1 \times 10^{14} W/cm^2$. This spectra is from the 23rd while most of the spectra shown in figure 4.20 are from the 22nd. On the 23rd the nozzle was 30 mm further from focus for most measurements, and the laser energy was set to 12 J rather than the 8 J from the 22nd. This indicates that most of the laser energy is inside of these spatial hot spots of intensity. In turn, this will lead to laser energy having a larger impact on the real intensity at the hot spots and the position of the nozzle having a lesser impact explaining why a plasma line is seen in figure 4.21 but not in 4.14 despite it having an overall higher intensity. Without having a stronger understanding of the intensity distribution of the laser and how it evolves as the laser focuses, it is difficult to quantify the real intensity in these hot spots. However, the calculated overall intensity is able to give a reasonable estimate for most of the analysis in this thesis.

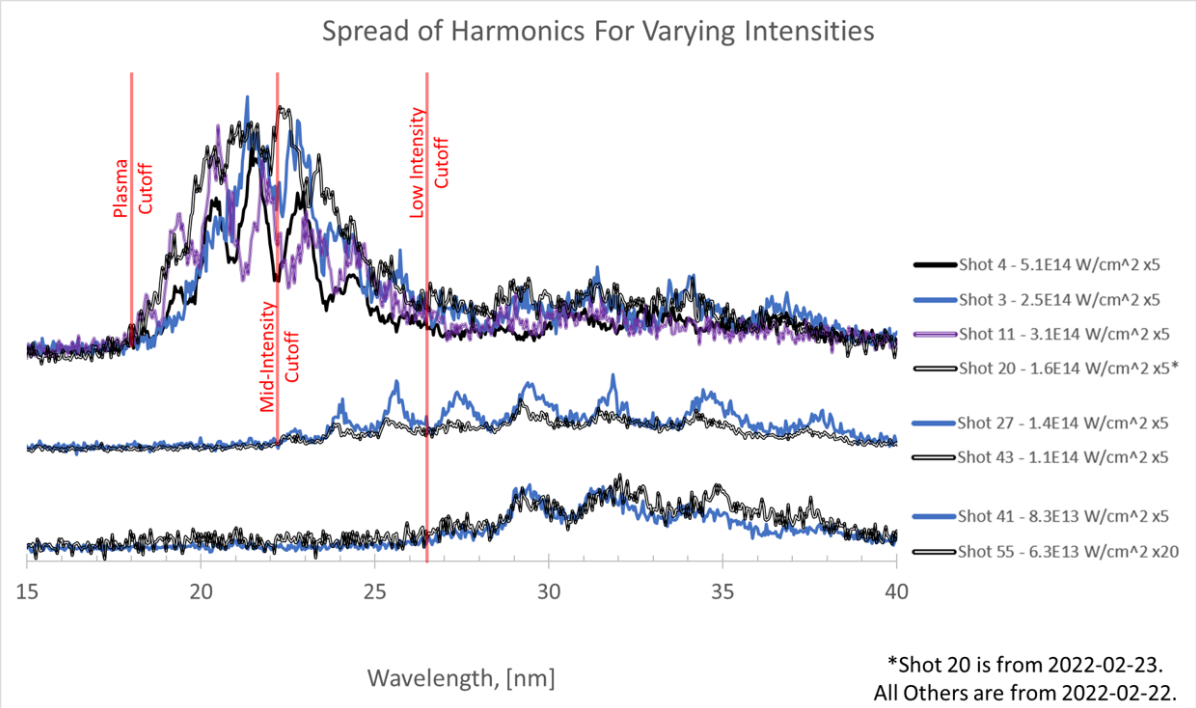

Figure 4.20: Spread of the harmonics for varying intensities from 2022-02-22 [2022-02-22, Shots 3,4,11,27,41,43,55, 8 J, varying, varying, varying, Argon, 46 bar, 22 ms, 6 mm, 100 mm, 8 mm, Grating] and 2022-02-23. [2022-02-23, Shot 20, 11.89 J, 600 fs^2, 72 fs, $1.6 \times 10^{14} W/cm^2$, Argon, 46 bar, 22 ms, 8 mm, 130 mm, 8 mm, Grating] Spectra are separated into three levels based on how far they extend. In the top level the black line is shot 4 from 2022-02-22, the blue line is shot 3 from 2022-02-22, the purple line is shot 11 from 2022-02-22, and the hollow black line is shot 20 from 2022-02-23. In the centre level the blue line is shot 27 from 2022-02-22 and the hollow black line is shot 43 from 2022-02-22. In the bottom level the blue line is shot 41 from 2022-02-22 and the hollow black line is shot 55 from 2022-02-22.

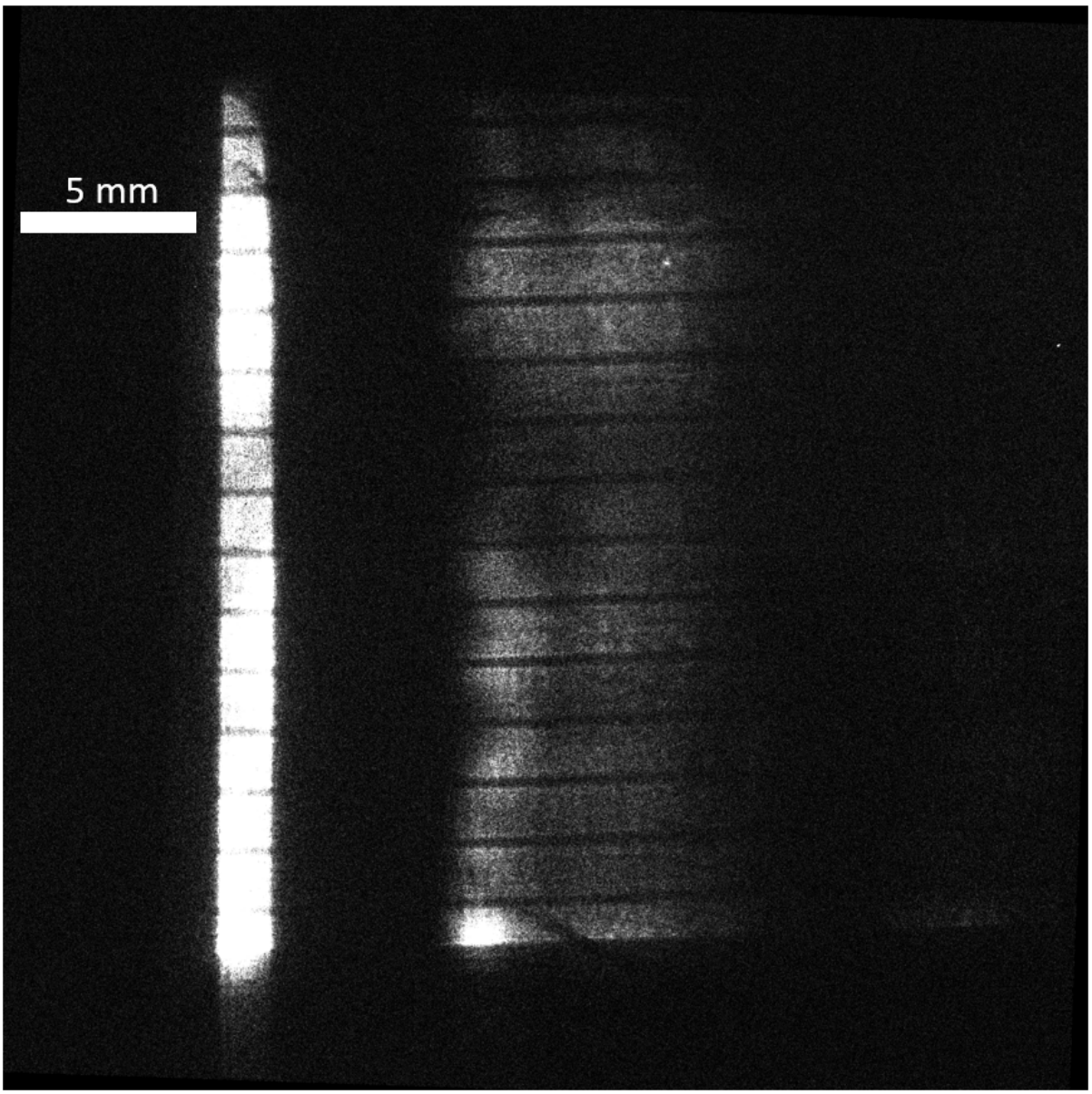

Figure 4.21: Spectra for shot 17 Feb 23rd 2022 with an intensity of only $1 \times 10^{14} W/cm^2$. [2022-02-23, Shot 20, 12.17 J, 600 fs^2, 113.3 fs, $1.0 \times 10^{14} W/cm^2$, Argon, 46 bar, 22 ms, 8 mm, 130 mm, 8 mm, Grating]

Error in the Spectra Measurement

As was established in figures 4.16 and 4.17, shot 20 from Feb 23rd and shot 27 from Feb 22nd line up well with the calculated harmonics. In turn some of the other measured harmonics (such as those in shots 3, 41, 43, and 55) line up well while others line up less well (such as shots 4 and 11) as can be seen in figure 4.20. The accuracy of these spectra measurements are highly dependent on the spatial modulation of each shot.

In order to quantify the error in spectra measurements the difference between measured and calculated harmonics for varying shots is shown in figure 4.22. The centroid of each visible peak was used for the measured data. This was done by first subtracting the rest of the signal that was not distinguishable from the peaks themselves and then taking the

centroid. Calculating the centroids in this manner helped reduce biasing the centroid calculation. For each of the lineouts the distance between the grating and the CCD was set to 68.25 cm (the best match value deduced previously), while the x_{zero} position was typically taken to be the peak of the zeroth order.

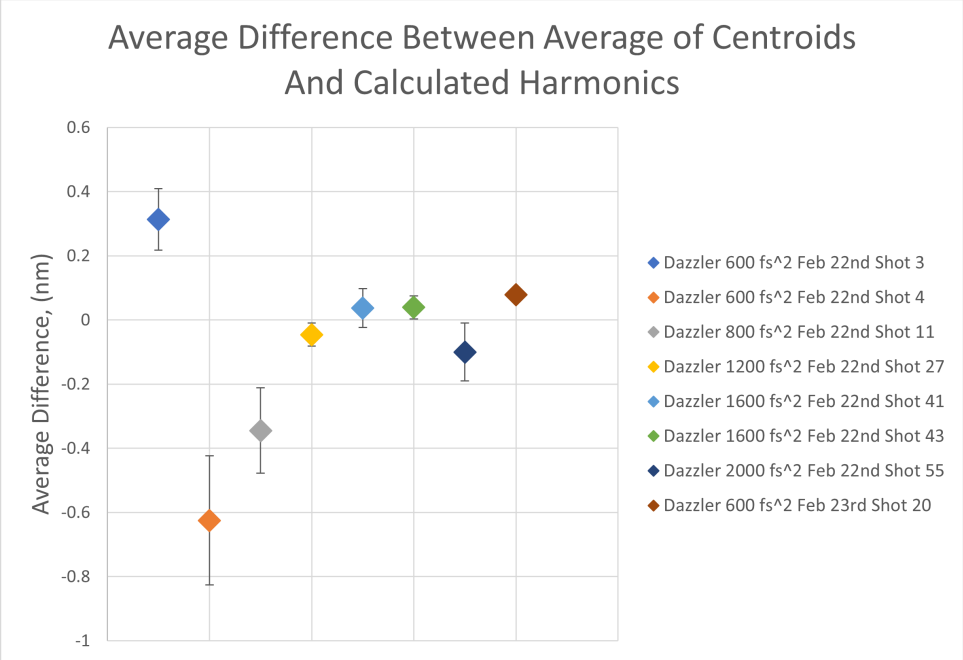

Figure 4.22: Difference between measured centroids of peaks and calculated harmonics from 2022-02-22 [2022-02-22, Shots 3,4,11,27,41,43,55, 8 J, varying, varying, varying, Argon, 46 bar, 22 ms, 6 mm, 100 mm, 8 mm, Grating] and 2022-02-23. [2022-02-23, Shot 20, 11.89 J, 600 fs^2, 72 fs, $1.6 \times 10^{14} W/cm^2$, Argon, 46 bar, 22 ms, 8 mm, 130 mm, 8 mm, Grating]

Some of the higher energy shots from 2022-02-22 are shown to have a large amount of error between measured and calculated values. However, shot 20 from 2022-02-23 is also a high energy shot and displays the least amount of error. As such, there does not appear to be a clear trend for error in the data apart from issues in relation to spatial modulation. Overall most measurements are reasonably close to the calculated value, lending credibility to the presumption that these are high-order harmonics.

4.4.3 Absorption of XUV Light

The spectrum output by the CCD is a filtered representation of the real spectra generated. There is absorption of XUV light due to a number of different sources including the aluminum filters used to separate XUV light from the visible light, absorption in the argon gas itself, trace amounts of water and hydrocarbon films covering either the aluminum filters or some of the optics, and the quantum efficiency of the camera itself. Transmission plots for the aluminum, argon, and water were obtained from [22], and the quantum efficiency plot for the camera was obtained from the Sophia XO camera data sheet [40]. These along with the raw data for shot 27 of 2022-02-22 are shown in figure 4.23. This shows that the filters heavily bias the result towards shorter wavelengths up

until $\sim 17nm$ at which point the aluminum filter transmission drops to zero, blocking everything past that point. The aluminum filter is taken to be two 1.6 um filters, while the water is taken to be 0.05 um although this is probably excessive. The argon transmission is merely an example, showing the transmission through 0.5 mm of 30 torr argon. The exact absorption effects of the argon are rather complicated since the argon gas will be distributed throughout the chambers at different densities from the source to the diagnostic measurement. In order to determine the exact absorption effects a sophisticated simulation capable of modeling HHG in gas as well as the absorption of it would be required. The development of such a simulation will be left for further research.

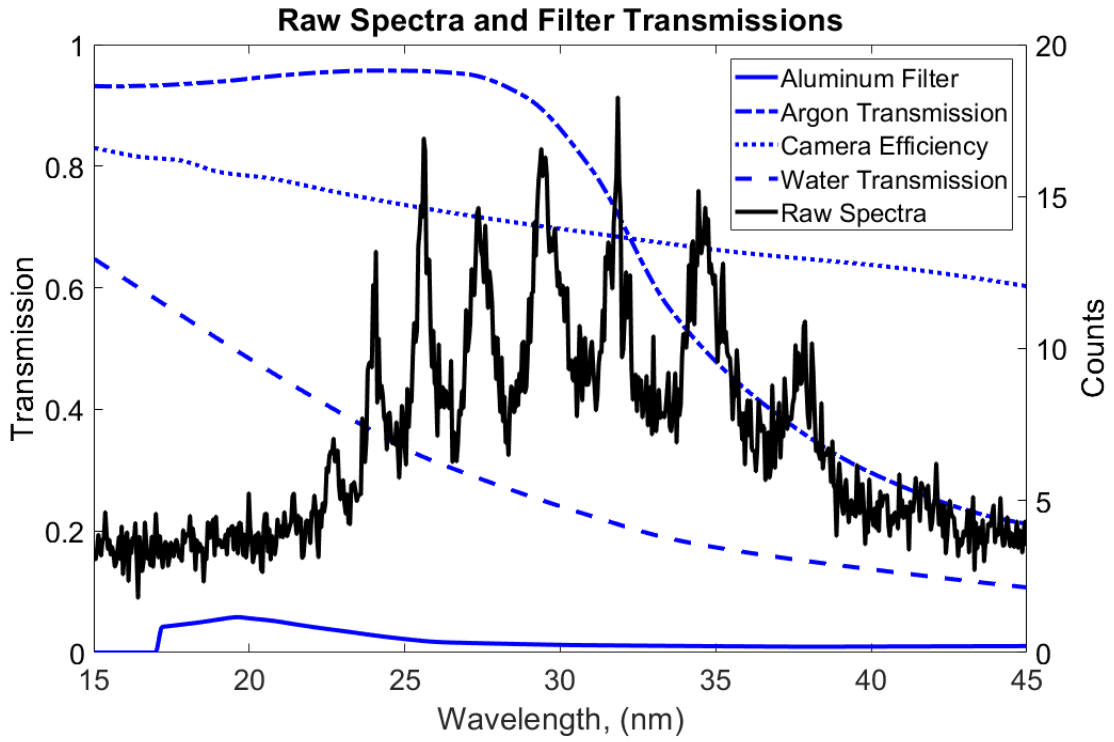

Figure 4.23: Image of the raw data from shot 27 with the transmission from the aluminum filter, argon gas, and water layer [22] shown along with the camera spectral efficiency. [40] The solid black line is the measured spectrum, the solid blue line is the aluminum filter transmission spectrum, the dashed blue line is the water transmission spectrum, the dotted blue line is the quantum efficiency of the Xray CCD, and the dashed and dotted blue line is the argon transmission spectrum. [2022-02-22, Shot 27, 8 J, 1200 fs^2, 95.2 fs, $1.4 \times 10^{14} W/cm^2$, Argon, 46 bar, 22 ms, 6 mm, 100 mm, 8 mm, Grating]

Taking the inverse of the camera efficiency, alumnium filter absorption, and water absorption provides the corrected spectra shown in figure 4.24. The spectra is adjusted to be stronger at higher wavelengths with the center of the harmonics seemingly shifted to between the 25th and 23rd harmonic (wavelengths of 31.8 and 34.6 nm) rather than 27th and 25th harmonic (wavelengths of 29.4 and 31.8 nm).

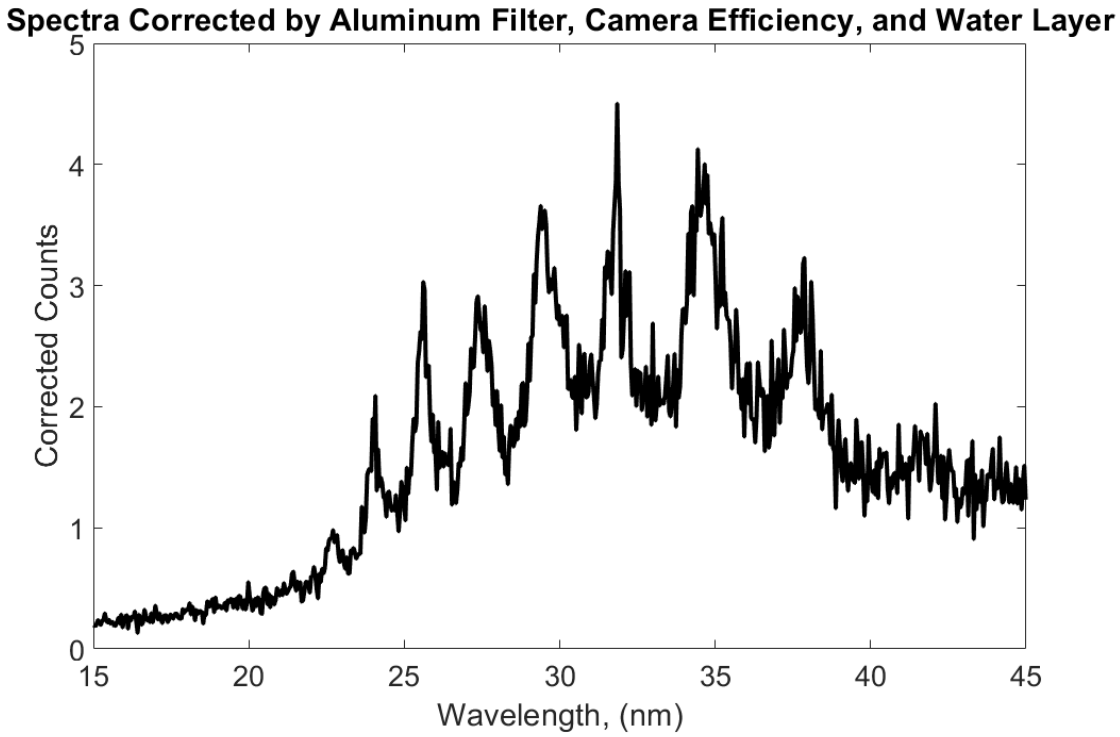

Figure 4.24: Spectra corrected for camera efficiency and absorption in the aluminum filter and water layers. [2022-02-22, Shot 27, 8 J, 1200 fs^2, 95.2 fs, $1.4 \times 10^{14} W/cm^2$, Argon, 46 bar, 22 ms, 6 mm, 100 mm, 8 mm, Grating]

4.4.4 Hot Plasma Spectra

Xenon gas was also used in addition to the argon gas used for most of the experiment. As mentioned in the background chapter xenon should have a higher conversion efficiency than argon. An example of a shot from the xenon measurements with mesh 2 is shown in figure 4.25. Interestingly the use of xenon seems to have picked up streaks and dots on the camera which were not seen before when using argon gas and are not seen after. It is unclear what causes this but it may be due to some water freezing on the detector or air which was let in when the gas was changed. Unfortunately, the conversion efficiency of the xenon gas is rather low which results in very faint spectra as seen in figure 4.26. This may at first seem in conflict with the conversion efficiencies seen in the background chapter, however the xenon efficiency falls off quickly and the various filters (in particular the aluminum filter) reduce the intensity of lower order harmonics. Therefore argon gas may actually have a greater intensity in the spectral region that is being examined which is in line with the observed data.

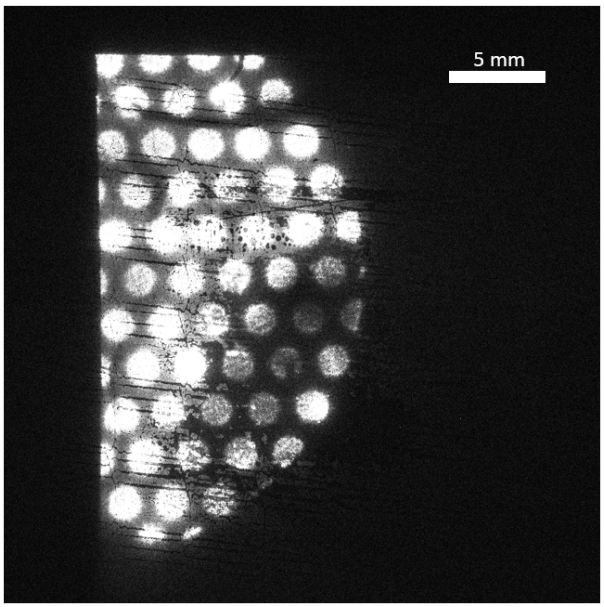

Figure 4.25: Example of a CCD image when using xenon gas, mesh 2 is in the way of the beam. [2022-02-18, Shots 251-255, 8 J, 1000 fs^2, Ave 58.4 fs, Ave $1.5 \times 10^{14} W/cm^2$, Xenon, 21 bar, 21 ms, 8 mm, 130 mm, 8 mm, Mesh 2]

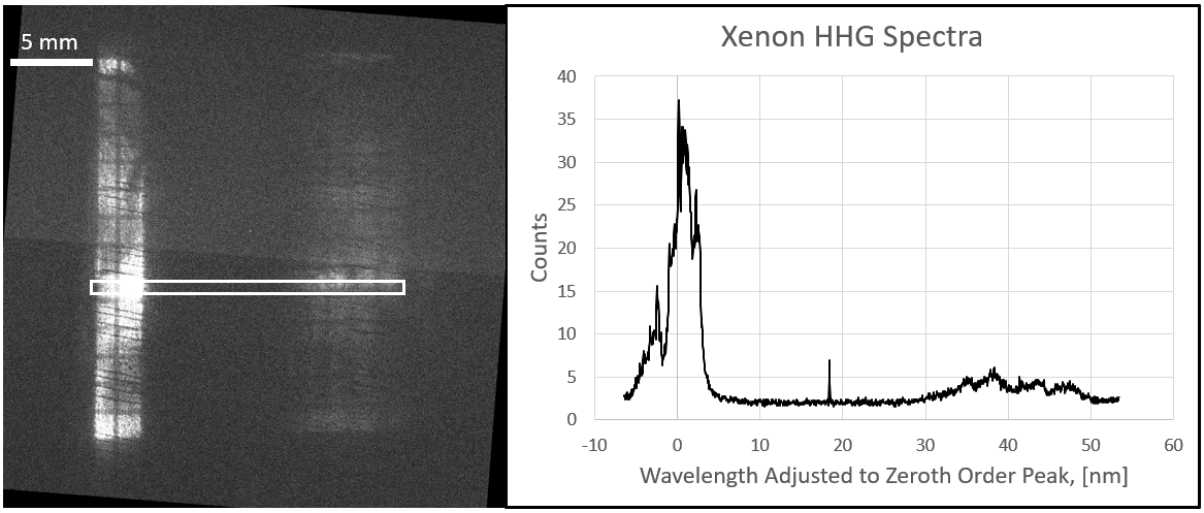

Figure 4.26: Spectra of HHG in xenon. [2022-02-21, Shots 81-115, 8 J, 600 fs^2, Ave 64 fs, Ave $1.3 \times 10^{14} W/cm^2$, Xenon, 24.5 bar, 26 ms, 7 mm, 130 mm, 8 mm, Grating]

A test of plasma formation was performed using xenon gas and a high laser intensity at the nozzle. This resulted in the formation of a hot plasma rather than HHG. The spectra for this is shown in figure 4.27 showing a single bright plasma line at 19 nm and nothing else. This is typical of the spectra expected from a hot plasma as opposed to the large spread of harmonics seen in the HHG spectra. The fact that the spectra in figure 4.26 is noticeably more spread out at longer wavelengths (albeit without clear harmonics) than this spectra lends credence to the belief that HHG is indeed occurring.

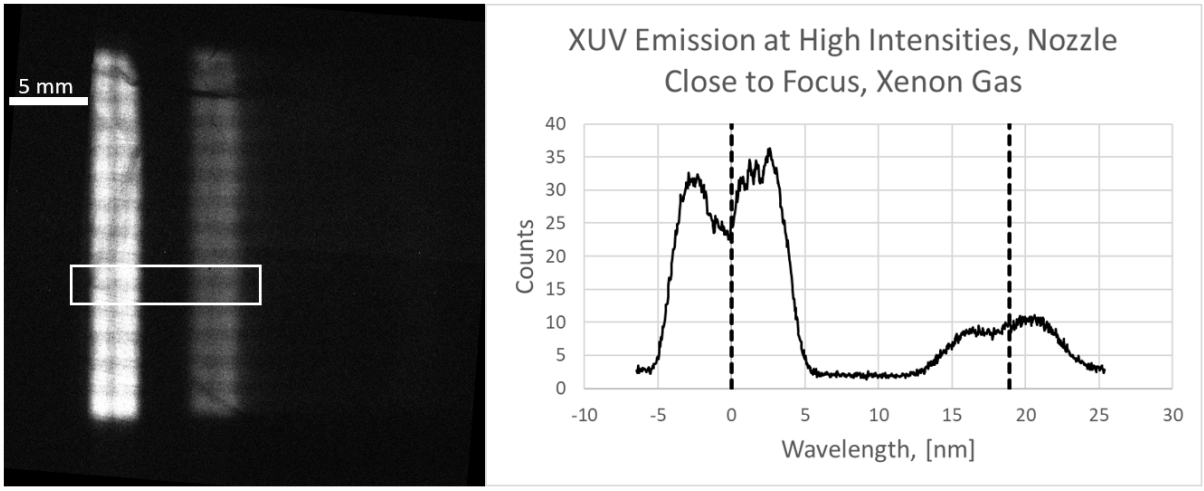

Figure 4.27: Spectra of a hot plasma formed in xenon. [2022-02-21, Shots 126-135, 8 J, 600 fs^2, Ave 58 fs, Ave 9.7 × $10^{14} W/cm^2$, Xenon, 24.5 bar, 26 ms, 5 mm, 50 mm, 8 mm, Grating]

4.5 Knife Edge

The use of diffraction from a knife edge allows us to estimate the spectral wavelengths and secondly the source spot size due to the blurring of the diffraction pattern.

4.5.1 Spectral Confirmation

First, in order to determine the spectral wavelengths of the knife edge, a lineout across the edge can be taken for a monochromatic source of wavelength λ. This will provide the variation in the intensity of light across the edge. After this is done a result similar to the small insert plot in figure 4.28 [42] could ideally be obtained. There should be an initial peak followed by a series of decreasing oscillations around the platuea intensity I_u. The intensity can be divided by I_u to normalize it about this oscillation line. The position of the lineout can then be adjusted so that the zero position is at 0.25 in the scaled intensity. This point where the line crosses the y-axis is now called O and is the spatial position of the knife edge. This is done because Fresnel diffraction can be modeled along a curve known as Cornu's spiral shown in the larger plot in figure 4.28. In this plot ν is the phase variable, represented by the distance along the curve and the coordinates of any point (x,y) on the spiral are given by the Fresnel integrals shown in equations 4.2 and 4.3.

$$x = \int_0^{\nu} cos\frac{\pi\nu^2}{2} d\nu \tag{4.2}$$

$$y = \int_0^{\nu} sin\frac{\pi\nu^2}{2} d\nu \tag{4.3}$$

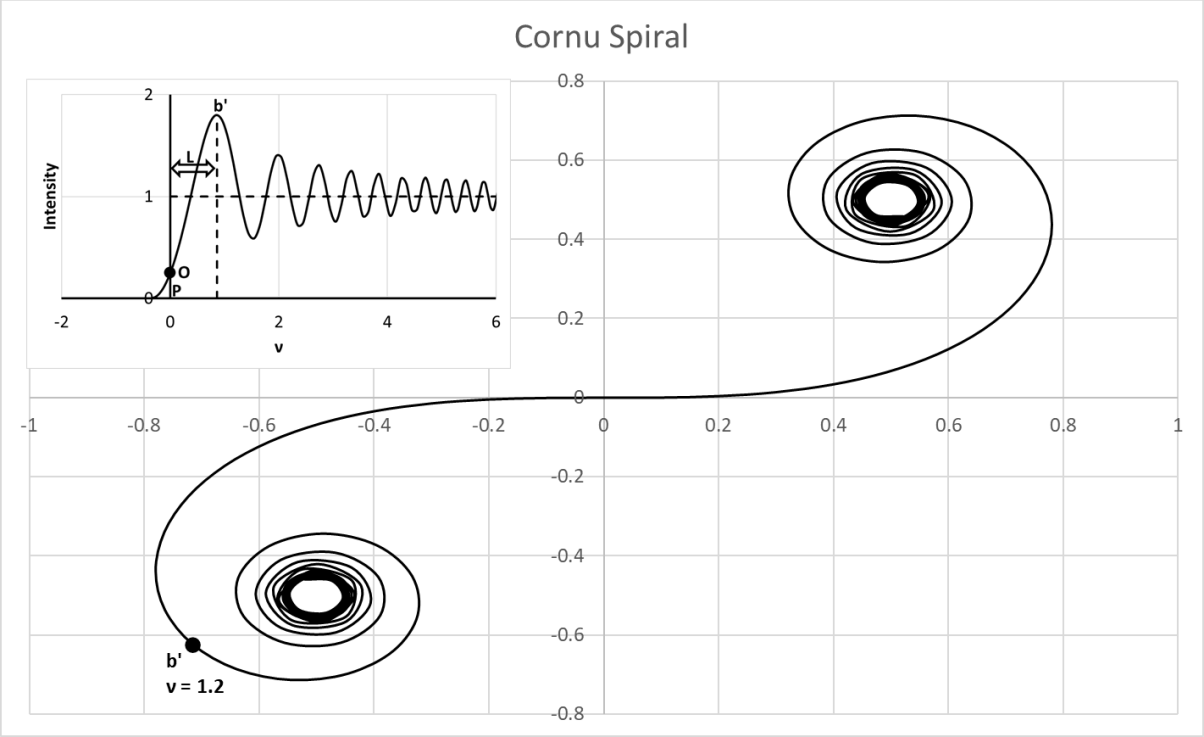

Figure 4.28: Theoretical example of Fresnel diffraction across a knife edge for intensity superimposed on the Cornu spiral for a straight-edge diffraction pattern. Data used to compose these plots from [42].

The Fresnel integrals do not need to be solved for, but it can be used to determine that the position of the first intensity peak, b', is at a position of $\nu = 1.2$. Equation 4.4 relates the position on the observation screen, L, to the phase variable, ν, as given by equation 4.4 and the variables defined in figure 4.29. [42] Here it can be seen that the term "a" in this equation refers to the distance from the source to the knife edge, while the term "b" is the distance from the knife edge to the CCD. This leaves wavelength λ, and L which is the lateral distance from the knife edge seen on the CCD. With all of this in mind the distance between point "O" and the first peak can be determined and the wavelength calculated.

$$L = \nu\sqrt{\frac{b\lambda(a+b)}{2a}} \tag{4.4}$$

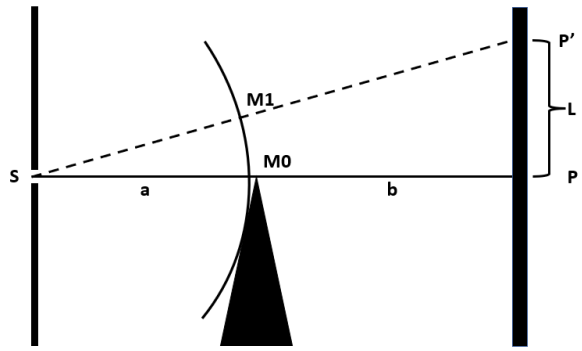

Figure 4.29: Side view of Fresnel diffraction across the knife edge.

An example of a knife edge result from the CLPU experiment is shown in figure 4.30. One can observe a peak along the highlighted edge indicating the presence of Fresnel diffraction. Lineouts of this and several other positions are shown in figure 4.31, the locations of each lineout are shown in appendix 3. Clearly the non-uniformity of the HHG is introducing background intensity gradients into the measurements introducing significant errors into the measured offset distance L.

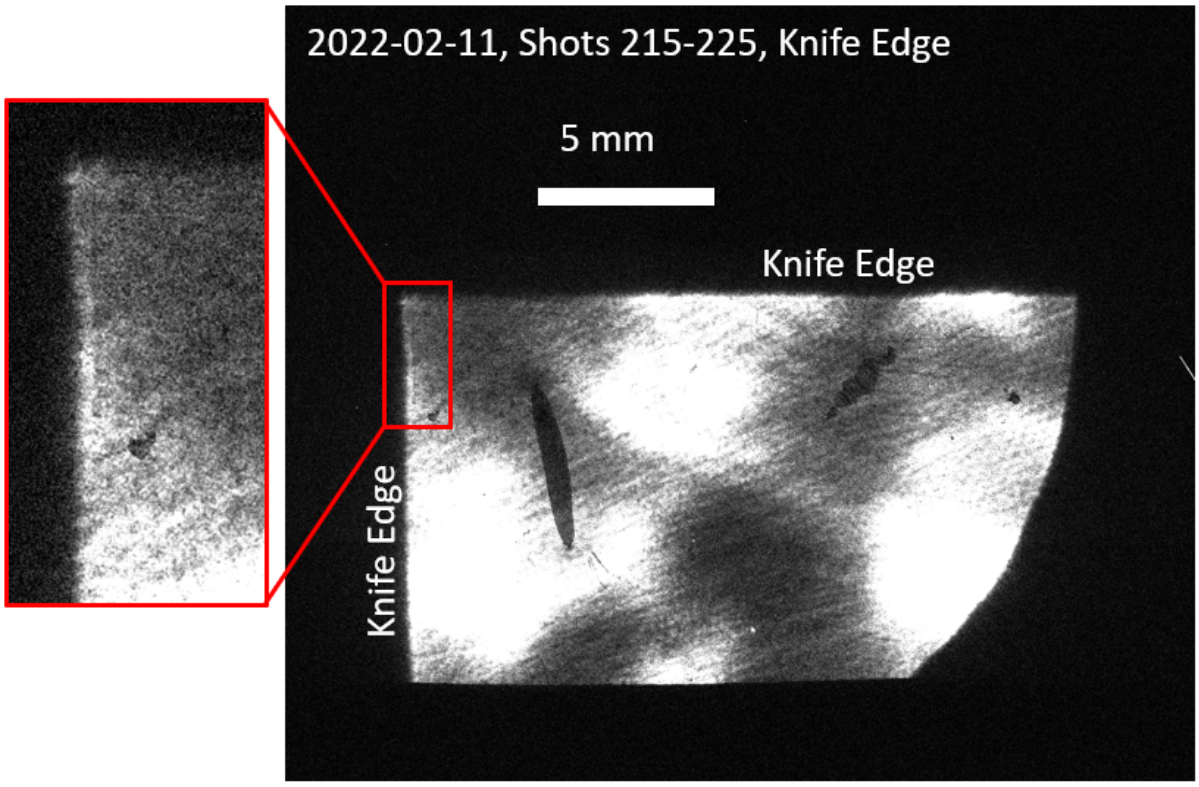

Figure 4.30: An example of Fresnel diffraction across the edge of a knife placed in the beam. [2022-02-11, Shots 215-225, 8 J, 800 fs^2, Ave 57 fs, Ave $1.6 \times 10^{14} W/cm^2$, Argon, 46 bar, 22 ms, 8 mm, 130 mm, 8 mm, Knife Edge]

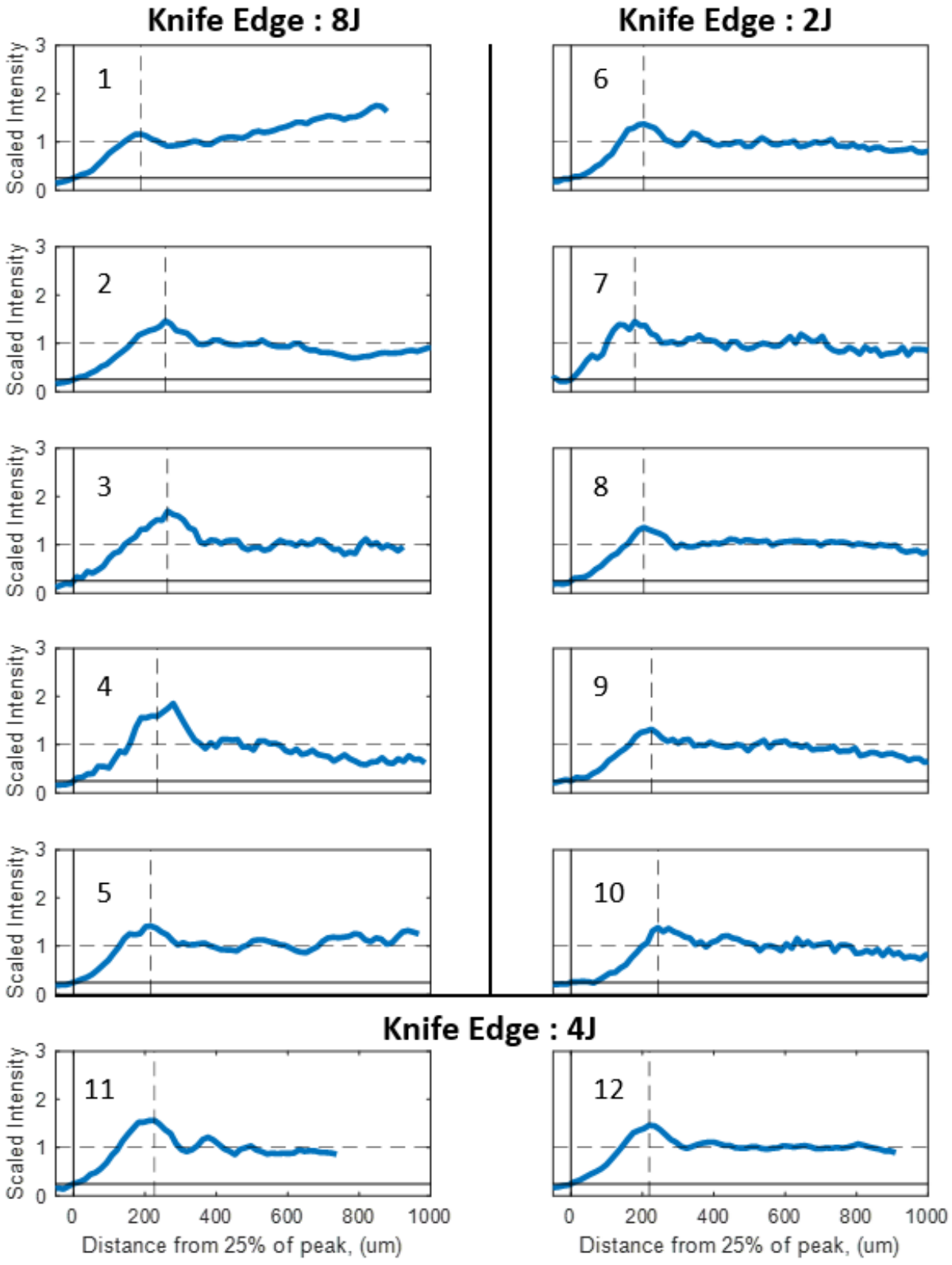

Figure 4.31: Compilation of various lineouts across the knife edge for 8, 4, and 2 J shots. [2022-02-08, Shots 139-168, 2 J, 1000 fs^2, Ave 77 fs, Ave $1.9 \times 10^{14} W/cm^2$, Argon, 36 bar and 21 bar, 22 ms, 4 mm, 50 mm, 8 mm, Knife Edge], [2022-02-10, Shots 170-179, 4 J, 800 fs^2, Ave 44 fs, Ave $2.1 \times 10^{14} W/cm^2$, Argon, 31 bar, 22 ms, 10 mm, 90 mm, 8 mm, Knife Edge], [2022-02-11, Shots 215-225, 8 J, 800 fs^2, Ave 57 fs, Ave $1.6 \times 10^{14} W/cm^2$, Argon, 46 bar, 22 ms, 8 mm, 130 mm, 8 mm, Knife Edge]

Lineout Number	1	2	3	4	5	6	Average
Wavelength, [nm]	24.2	45.4	47.6	37.5	32.2	28.6	34.1
Upper Limit of Spot Size, [um]	333	355	288	333	311	466	355.0
Lineout Number	7	8	9	10	11	12	Standard Error
Wavelength, [nm]	21.9	28.6	34.8	40.6	35.2	32.9	2.3
Upper Limit of Spot Size, [um]	422	422	311	311	244	466	21

Figure 4.32: Table of wavelength and upper limit of spot size from lineouts in figure 4.31. [2022-02-08, Shots 139-168, 2 J, 1000 fs^2, Ave 77 fs, Ave $1.9 \times 10^{14} W/cm^2$, Argon, 36 bar and 21 bar, 22 ms, 4 mm, 50 mm, 8 mm, Knife Edge], [2022-02-10, Shots 170-179, 4 J, 800 fs^2, Ave 44 fs, Ave $2.1 \times 10^{14} W/cm^2$, Argon, 31 bar, 22 ms, 10 mm, 90 mm, 8 mm, Knife Edge], [2022-02-11, Shots 215-225, 8 J, 800 fs^2, Ave 57 fs, Ave $1.6 \times 10^{14} W/cm^2$, Argon, 46 bar, 22 ms, 8 mm, 130 mm, 8 mm, Knife Edge]

The wavelengths determined from these lineouts are shown in the table of figure 4.32. This leads to an average of 34.1 nm which lines up well with the harmonic spectra as shown in figure 4.17 which has a centroid of 30.6 nm. There are a few points at 40 nm and higher which is a bit high for the spectra observed but not unreasonably high and may be attributed to error from the spatial modulation. There are also some lower values in the 20 nm range which falls within the bright spectral line attributed to plasma formation seen in figure 4.16. The first lineout is one of these 20 nm points which is taken over a bright spot on the 8 J case meaning it is feasible there is a significant plasma formation thereby resulting in the lower value. The seventh lineout also predicts a wavelength in the 20 nm range. This is for the 2 J case however, and is unlikely to have any plasma formation. Therefore, this is likely due to error from the spatial modulation. Overall, the range of wavelengths predicted by the knife edge lineouts are reasonable based on the observed spectra and help verify the accuracy of the observed spectra.

4.5.2 Spot Size

The knife edge can be used to estimate the spot size at laser focus. This can be done by measuring the distance across which the intensity is still above background from the region unblocked by the knife edge to the fully blocked region an example of which is shown in the image on the right of figure 4.33. After measuring this distance on the CCD (L), the known distances between knife edge and CCD (b) as well as TCC and knife edge (a) can be used to determine the angle (θ) at which point the spot size of the laser at focus can be determined.

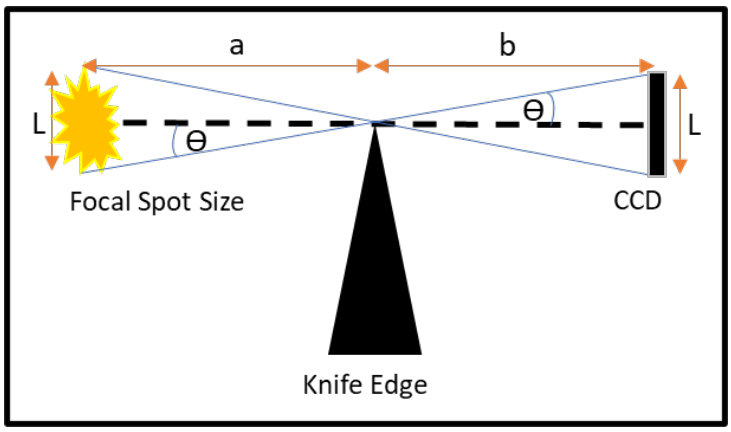

Figure 4.33: Layout of the knife edge for spot size calculation (left), simulated example of lineout across a knife edge (right).

Applying this technique to the previously acquired lineouts across the knife edge leads to the results shown in the table of figure 4.32. The average upper bound for the spot size is 355 um. Since the laser is not able to perfectly focus, it is not expected that the size of the beam will be non-zero but the size of the beam within the range of the nozzle varies between 22 mm and 4.4 mm as shown in figure 4.3, much larger than 244 um indicating that the XUV is not coming from a large plasma formed at the nozzle and is instead focusing down as expected.

Calculated Blurring

These values are the estimated upper bound of the spot size. In reality, as can be seen in figure 4.28, the diffraction will also extend the observed edge of the knife. In order to account for this, the calculated blurring of the knife edge for varying spot sizes are compared to the measured lineouts to determine which fits best. [42]

Before calculating the blurring from a large spot size however, the blurring due to the broad spectrum has to be found. This is shown in figure 4.34. The above image shows multiple knife edges weighted based on the spectrum shown in figure 4.17, and the below image is the combination of all the wavelengths. As can be seen this has already severely dampened the ringing after the first peak and the first peak is at the centroid of the spectrum.

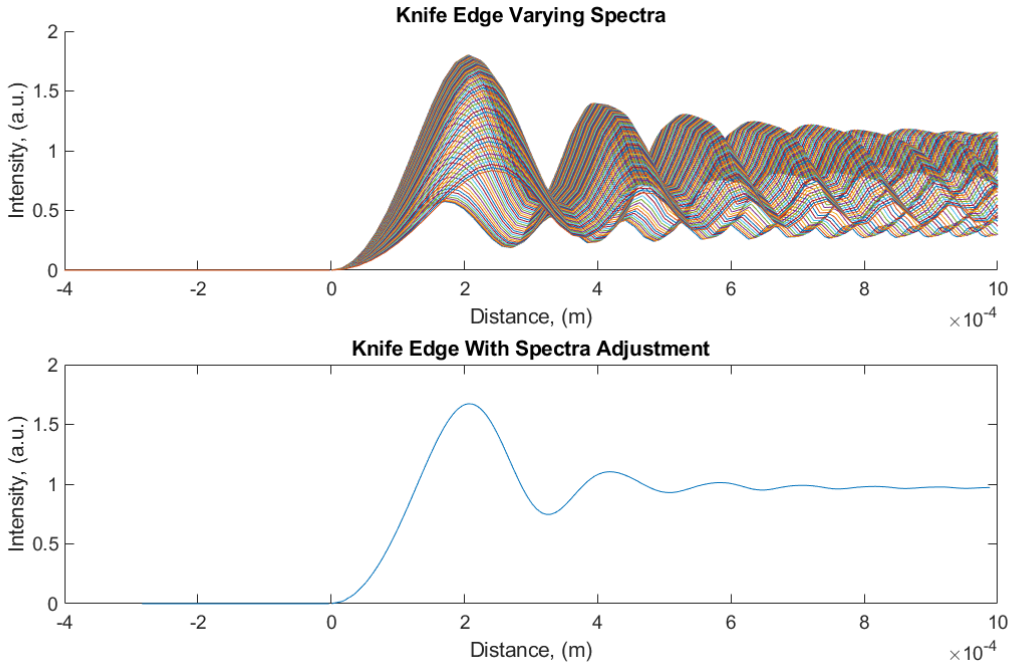

Figure 4.34: Multiple calculated knife edge lineouts weighted based on the spectra shown in figure 4.17 (above), and the combination of all of these into a single lineout (below).

With the lineout from figure 4.34 the blurring from the spot size can be found. This is shown in figure 4.35 which uses the 11th lineout from figure 4.31. Here the 250 um spot is shown to line up well with the slope at position 0 but the peak is too blurred and the ringing oscillations are almost completely gone. Meanwhile, the 100 um spot lines up better with the peak and has some oscillations (although still not as many as the measured data) but does not agree as well with the slope at position 0. This seems to indicate that the spot size is somewhere between 100 and 250 um, although the oscillations are still weak in these calculated lineouts perhaps indicating that the spot size is even smaller. A spot size of 500 um is also included, here the ringing oscillations are completely lost and the peak is nearly gone as well. The slope at position 0 is significantly broader than the measured slope.

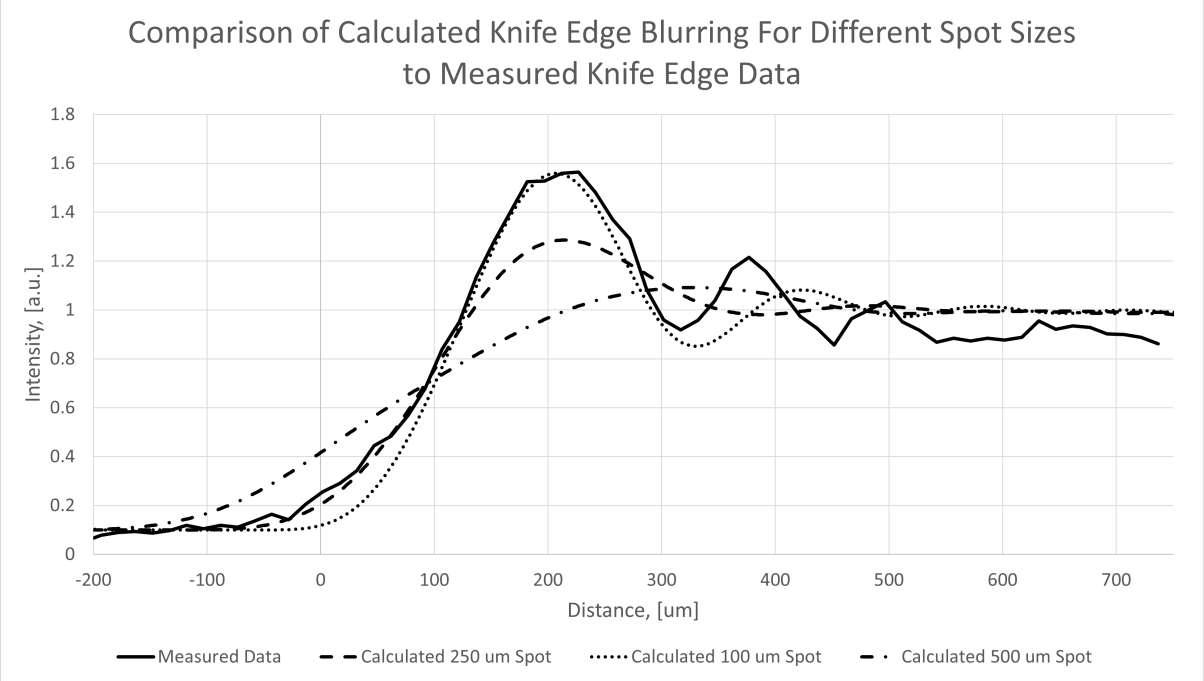

Figure 4.35: Comparison of measured knife edge and calculated knife edge for different spot sizes. The solid line is the measured data, the dashed line is the calculated knife edge with a 250 um spot, the dotted line is the calculated knife edge with a 100 um spot, and the dashed and dotted line is the calculated knife edge with a 500 um spot. [2022-02-10, Shots 170-179, 4 J, 800 fs^2, Ave 44 fs, Ave $2.1 \times 10^{14} W/cm^2$, Argon, 31 bar, 22 ms, 10 mm, 90 mm, 8 mm, Knife Edge]

Plasma Spot Size

In order to check the effect of an actual plasma, the knife edge technique was applied to the previously discussed xenon plasma as shown in figure 4.36. This shot was taken with the nozzle placed 50 mm from the laser focus. A lineout is shown on the right, this lineout predicted a spot size of 3.95 mm while the average of several lineouts provides a spot size estimate (with the distance 'a' adjusted by 50 mm as the source position is assumed to be at the nozzle) of $\sim 3.4mm$, which is 1 mm less than the 4.4 mm beam size at this nozzle position, but is certainly much larger than the 100 - 250 um seen in the previous result. Therefore providing credibility that the XUV light is actually being created through the focusing geometry as opposed to a plasma source located at the gas nozzle itself.

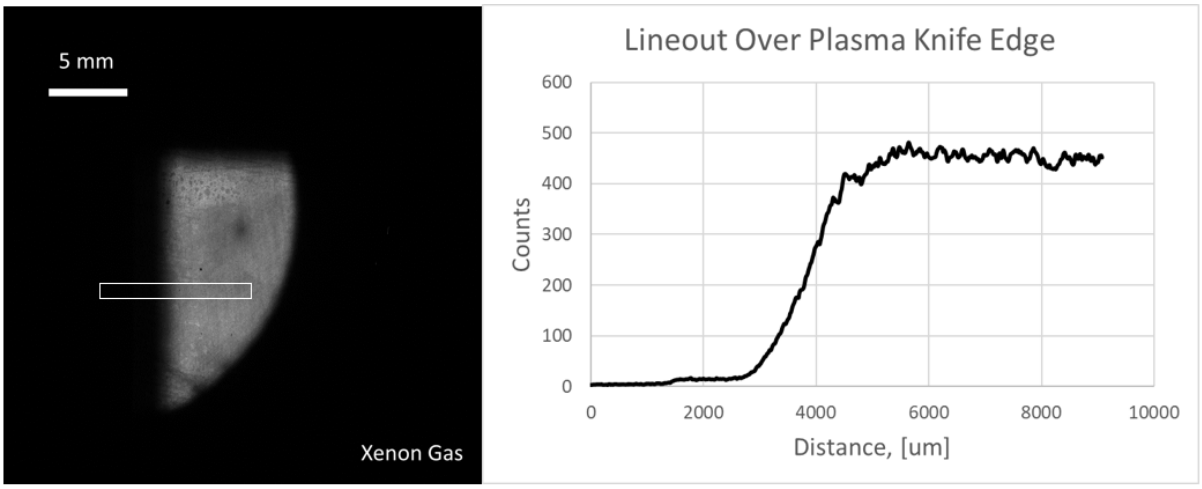

Figure 4.36: Knife edge with Xenon plasma. [2022-02-18, Shots 216-220, 8 J, 1000 fs^2, Ave 46.8 fs, Ave $1.2 \times 10^{14} W/cm^2$, Xenon, 21 bar, 21 ms, 5.6 mm, 50 mm, 8 mm, Knife Edge]

4.6 Shadowgraphic Imaging of Perforated Mesh

In order to demonstrate that a convergent cone of HHG radiation was generated a perforated aluminum sheet was used as a shadowgraphic mask to measure the beam divergence. This sheet was 0.6 mm thick, which was adequate to block the XUV light, and contained 1.2 mm diameter holes. [43] A picture of this mesh is shown in figure 4.37. Using this picture as a reference it was determined that the actual size of the holes was closer to 1.1 mm (see appendix 4) so that number is used for the calculations. The spacing between the holes along the axis of measurement was taken to be 1.67 mm $\pm 0.1mm$ based on measurements from this picture as well.

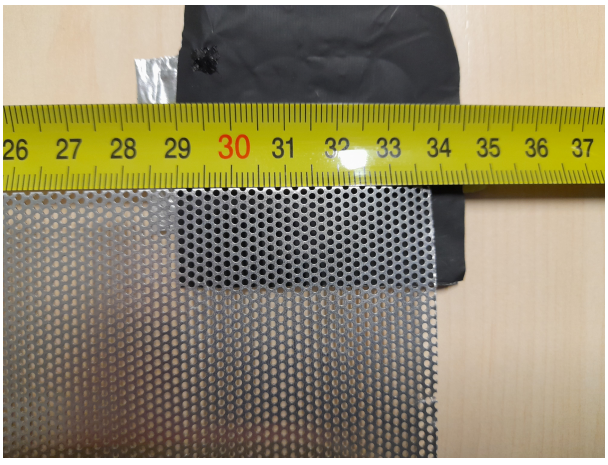

Figure 4.37: A picture of the perforated mesh used, along with a ruler for scale.

Two small pieces of this mesh were cut off and mounted on translation stages which could be moved in and out. Mesh 1 was mounted further from the camera on the same translation stage as the knife edge, while mesh 2 was mounted closer to the camera on its

own translation stage. This allowed for the meshes to be moved in and out of the beam as desired.

When placed in the beam the mesh creates a shadow which is then projected onto the CCD. This provides information on both the size of the beam and the location of the light source.

As discussed in the previous section, the size of the beam determines how much blurring of the image occurs. A large light source, such as a light bulb, would create a very blurred image while an infinitely small point source should create a perfectly sharp image. An ideal beam would act as a point source at laser focus which would then create a perfectly sharp image of the mesh on the CCD. Because diffraction lasers have a minimum spot size, rather than creating a perfect point source some blurring would be expected from the real images. Therefore, the focal cone HHG geometry should yield shadowgraphic images of these meshes with a small amount of blurring of each hole. Simulations can also shed insight into what size the light source is so ray tracing simulations in Zemax Optic-Studio are also carried out. [44]

The other reason for doing the shadowgraphic imaging is to determine where the beam is coming from. The focal cone geometry should focus the HHG to the laser focal point, while a plasma light bulb should show that the light source is coming directly from the point of interaction at the gas jet. Images captured from a secondary camera were also analyzed in order to directly observe where the plasma is forming.

4.6.1 Beam Location

To understand the beam location, a scan from nozzle longitudinal positions 70 mm to 150 mm from laser focus with shots every 10 mm was performed.

Figure 4.38 shows the shadowgraphic image created by mesh 1, while figure 4.39 shows the shadowgraphic image of mesh 2. It can clearly be seen that mesh 1 appears larger than mesh 2 in this image. This is because mesh 1 is further away which gives the beam more time to spread out before reaching the camera. In order to calculate the location of the origin point for the beam, lineouts were taken across the four visible rows of mesh 1 and the five visible holes of mesh 2, with the start and end hole being decided based on the quality of the beam at that point. Typically this meant a distance between 7 and 10 holes. Due to the spatial modulation of the beam there is some small error in determining the exact center of each hole. In order to aid in this the number of counts in the image was capped at some point above the noise level allowing for flat topped peaks of each hole at some threshold value to be created. The centroids of the first and last of these peaks were then taken and the difference between both solved for. The known real distance between these holes was then calculated and the difference between that and the previous result was solved for. This allowed for the angle at which the image was

expanding to be determined and the resulting distance between the mesh and the light source to be calculated.

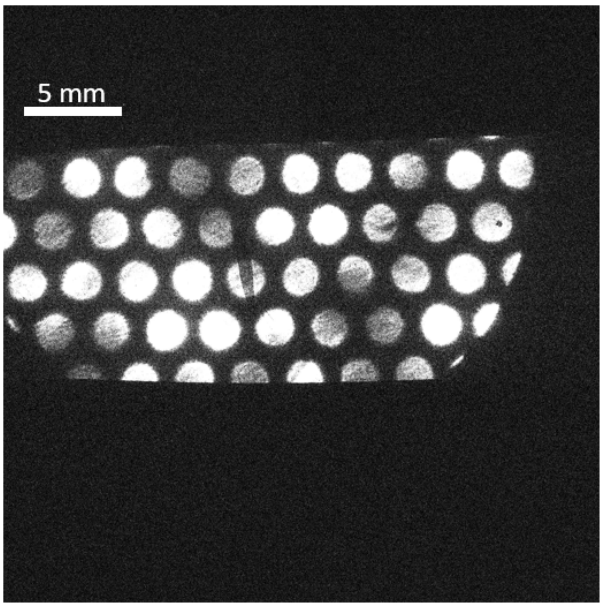

Figure 4.38: Shadowgraphic image of mesh 1 From 2022-02-11. [2022-02-11, Shots 207-211, 8 J, 800 fs^2, Ave 55 fs, Ave $1.8 \times 10^{14} W/cm^2$, Argon, 46 bar, 22 ms, 8 mm, 130 mm, 8 mm, Mesh 1]

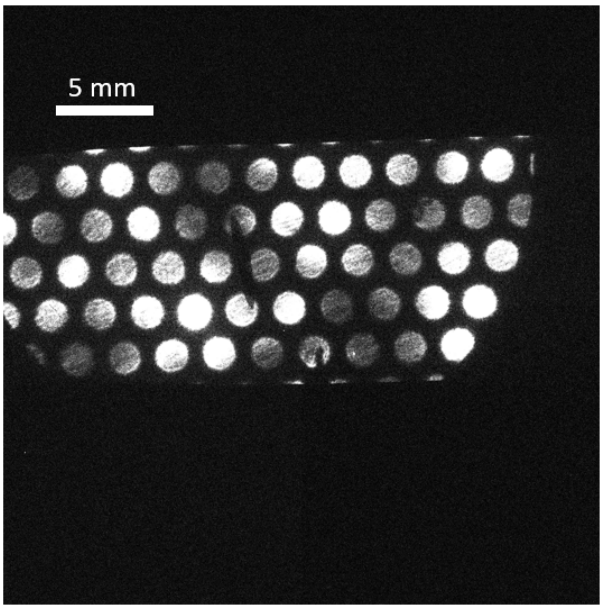

Figure 4.39: Shadowgraphic image of mesh 2 From 2022-02-11. [2022-02-11, Shots 202-206, 8 J, 600 fs^2, Ave 46 fs, Ave $1.8 \times 10^{14} W/cm^2$, Argon, 46 bar, 22 ms, 8 mm, 130 mm, 8 mm, Mesh 2]

Figure 4.40 shows the result of a scan of various nozzle distances from laser focus with mesh 2 in place. All shots were performed on the same day and no other parameters were changed during this scan. Figure 4.41 is a similar plot of mesh 1 as the nozzle distance from laser focus is varied. Unlike the former plot this was not the result of a scan over a single day and is instead a compilation from various days with a number of

other parameters changed including laser energy which was at 2 J on the 50 mm point, 4 J on the 90 mm point, and 8 J on the 130 mm point. In figure 4.40 the red dotted line represents the expected increase in distance to source if the source was varying with the nozzle longitudinal position. This expected variation can simply be found by adding on the change in nozzle position to the initial measurement at 70mm. However, instead of following this line, the data points are mostly clustered around a position of 2.90 ±0.0025 m with some small variation. The expected distance to the focal point is 3.00 m so this measurement is close to the expected value but there is still some difference. It should be noted that the last two data points are the result of a single measurement and therefore are assigned no error bar. The data point at 130 mm is the result of two lineouts which varied quite significantly from eachother, leading to the large error bar. None of this data indicates that the points are following the trend of the red line however, which provides a strong justification for believing that the XUV source is in fact being focused. Figure 4.41 also agrees with this assesment providing a distance to source measurement of 2.94 ±0.002 m. Despite there being somewhat larger errors than with mesh 2, the mesh 1 plot does not show an increase in distance to source as the nozzle distance from focus is increased. In fact there is a slight downward trend although this is likely just due to error in the measurement. Based on this analysis, it is our belief that the focusing aspect of the incident laser light is passed on to the HHG XUV light.

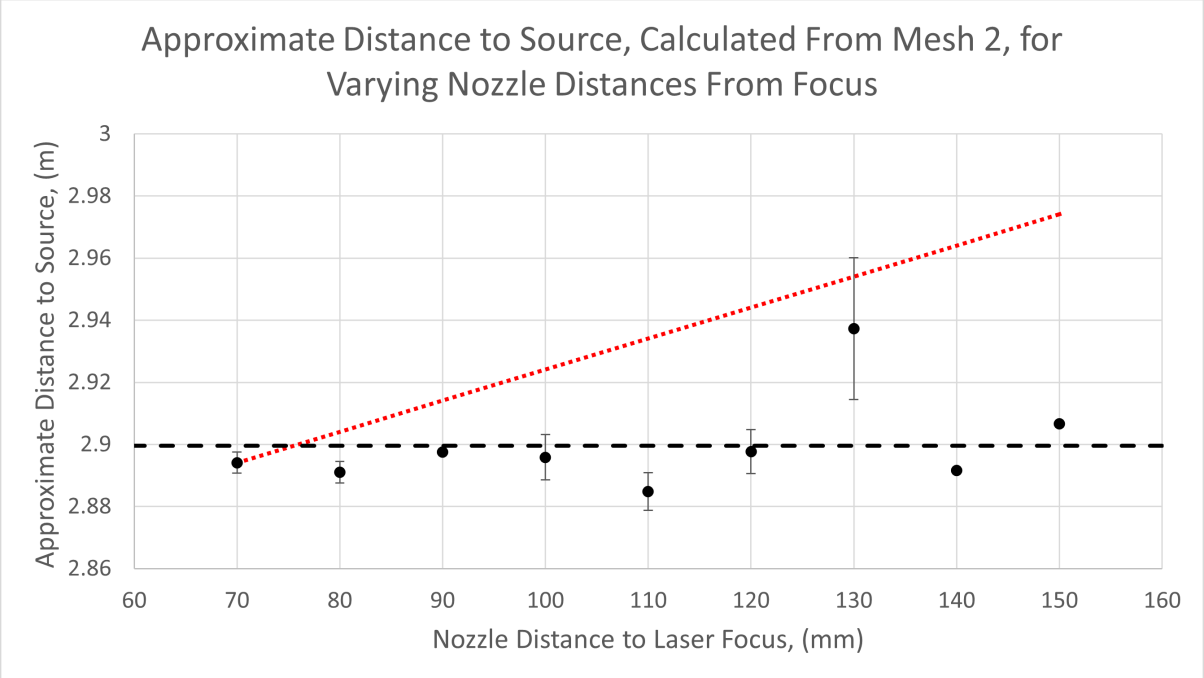

Figure 4.40: Distance to Source as calculated from mesh 2 for a scan of varying nozzle distances to laser focus between 70 and 150 mm. The red line is the expected position of each calculation based on the initial 70 mm calculation if the XUV source was situated at the nozzle rather than at laser focus. The black dashed line is the average value, and the black circles are the data points. The data points are averaged over a sampling of lineouts from an image at each nozzle position, with the error bars representing the standard error in this averaging. The 140 and 150 mm data points lack these error bars since only a single lineout was able to be obtained, with any real accuracy, at each of these points. [2022-02-10, Shots 82-126, 4 J, 800 fs^2, Ave 43 fs, Varying, Argon, 31 bar, 22 ms, 10 mm, Varying, 8 mm, Mesh 2]

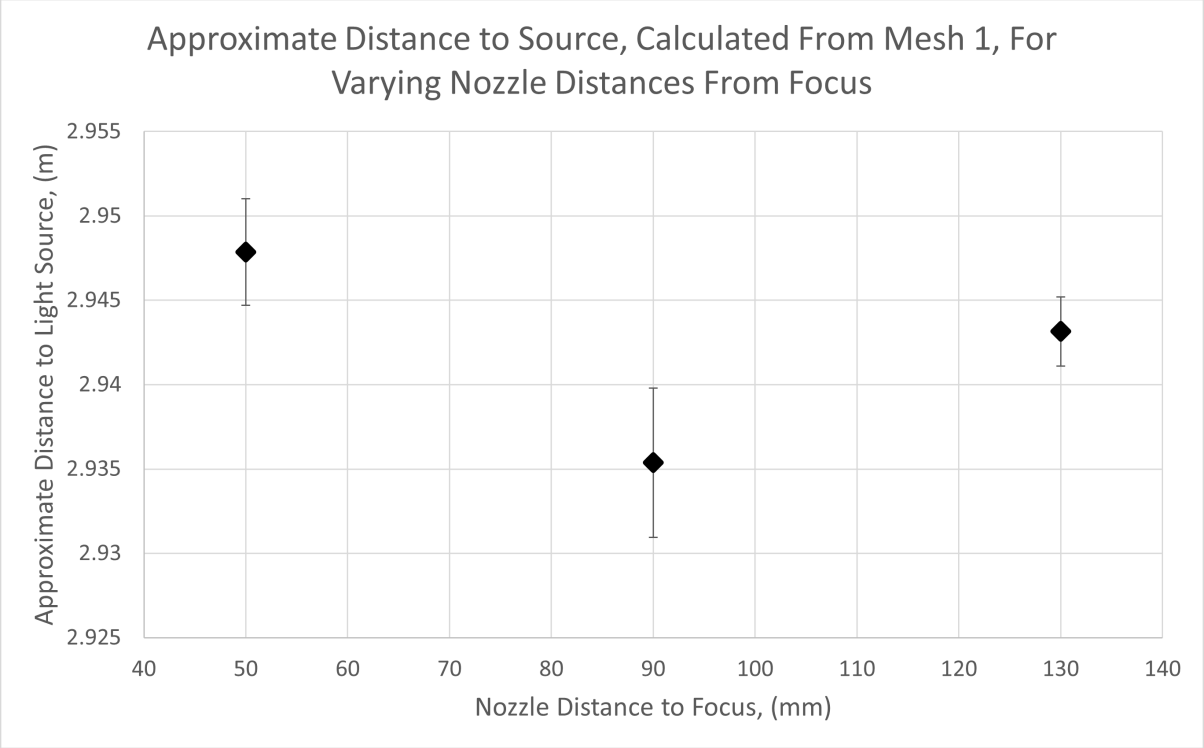

Figure 4.41: Distance to Source as calculated from mesh 1 for varying nozzle distances to laser focus between 50 and 130 mm. These are from three separate days and various other parameters were changed including laser energy. [2022-02-08, Shots 129-131, 2 J, 1000 fs^2, Ave 89 fs, Ave $1.7 \times 10^{14} W/cm^2$, Argon, 61 bar, 22 ms, 4 mm, 50 mm, 8 mm, Mesh 1], [2022-02-10, Shots 148-152, 4 J, 800 fs^2, Ave 40 fs, Ave $2.3 \times 10^{14} W/cm^2$, Argon, 31 bar, 22 ms, 10 mm, 90 mm, 8 mm, Mesh 1], [2022-02-11, Shots 207-211, 8 J, 800 fs^2, Ave 55 fs, Ave $1.8 \times 10^{14} W/cm^2$, Argon, 46 bar, 22 ms, 8 mm, 130 mm, 8 mm, Mesh 1]

As mentioned earlier the actual position of the light source was measured to be 3 m from the CCD, and that our measurements indicate a distance of 2.94 m and 2.90 m based on meshes 1 and 2 respectively. Some of this error may be attributed to measurement error. The distance from laser focus to CCD was measured with a measuring tape and given a rating of $\pm 1cm$ accuracy. The measurements of distance from both meshes to the CCD can be given a similar error rating, and the measurement of spacing between the holes can have an error of $\pm 0.1mm$. This is sufficient to account for the difference in measurement. Ultimately, however, the exact distances are not important for this calculation. The purpose of this section is to investigate how the XUV source position varies based on the nozzle distance from focus which means the relative differences are what is important rather than the exact distances.

4.6.2 Mesh blurring

Figures 4.42 and 4.43 compares the blurring of the measured data for the mesh to the blurring of ray tracing simulations performed in Zemax Optic Studio [44] for varying spot sizes. This is done for both mesh 1 and 2. While the knife edge calculations predicted an upper limit of 350 um for the spot size, the simulations show that both mesh 1 and 2 most closely agree with the a spot size around 0.5 mm. As discussed in the knife edge

section the blurring of the edge is due to both diffraction effects as well as the source size so while this 0.5 mm measurement is rather high, it acts as an upper bound for the spot size. For these measurements the beam size at the nozzle is 11.44 mm, significantly larger than the maximum spot size of 0.5 mm indicating that the XUV light is indeed focusing.

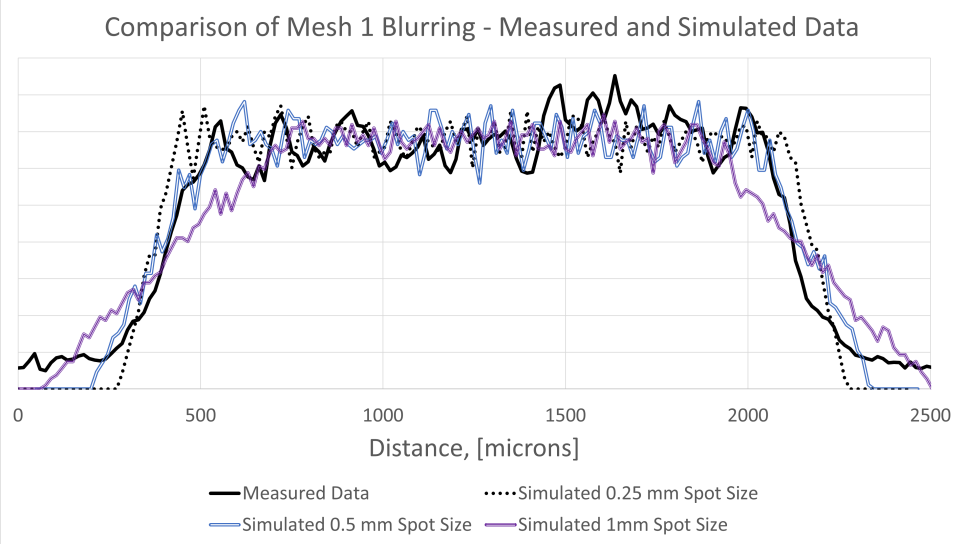

Figure 4.42: Measured data from Mesh 1 compared with simulated data for spot sizes of 0.25, 0.5, and 1 mm. The solid black line is the measured data, the dotted black line is the simulation with a 0.25 mm spot size, the hollow blue line is the simulation with a 0.5 mm spot size, and the purple line is the simulation with a 1 mm spot size. [2022-02-11, Shots 207-211, 8 J, 800 fs^2, Ave 55 fs, Ave $1.8 \times 10^{14} W/cm^2$, Argon, 46 bar, 22 ms, 8 mm, 130 mm, 8 mm, Mesh 1]

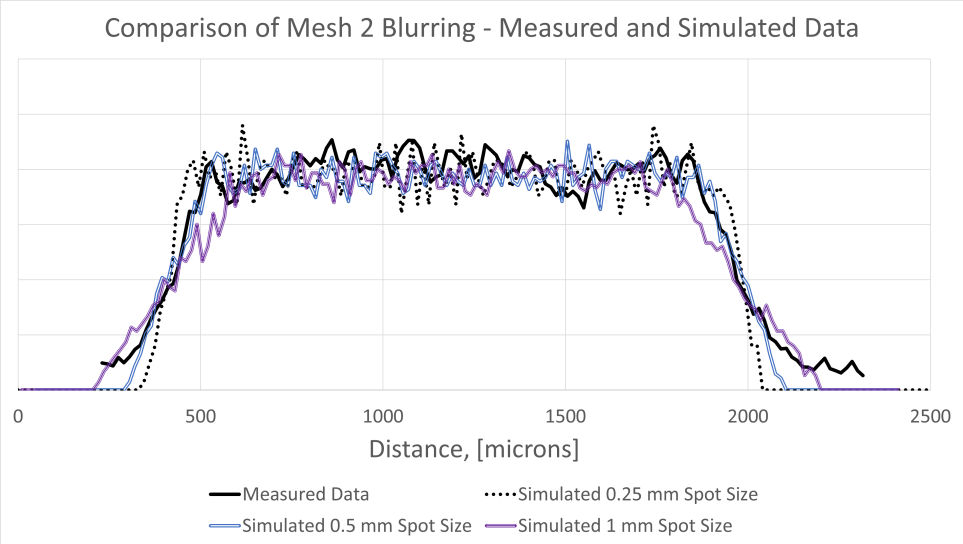

Figure 4.43: Measured data from Mesh 2 compared with simulated data for spot sizes of 0.25, 0.5, and 1 mm. The solid black line is the measured data, the dotted black line is the simulation with a 0.25 mm spot size, the hollow blue line is the simulation with a 0.5 mm spot size, and the purple line is the simulation with a 1 mm spot size. [2022-02-11, Shots 202-206, 8 J, 600 fs^2, Ave 46 fs, Ave $1.8 \times 10^{14} W/cm^2$, Argon, 46 bar, 22 ms, 8 mm, 130 mm, 8 mm, Mesh 2]

4.6.3 Plasma Formation

While the spot size and spectral range of the XUV will spread over the edge of a hole in the mesh, only the formation of a hot plasma would be able to lead to a signal far from the edge of a hole. Figure 4.44 shows mesh 1 backlit by a fully formed plasma leading to significant blurring and a high signal even between holes. However, while weaker, figure 4.38 and 4.39 also display a signal between the holes indicating that a plasma with weak emission is formed in addition to the harmonics. This is in agreement with the presence of the bright spectral line first seen in figure 4.13.

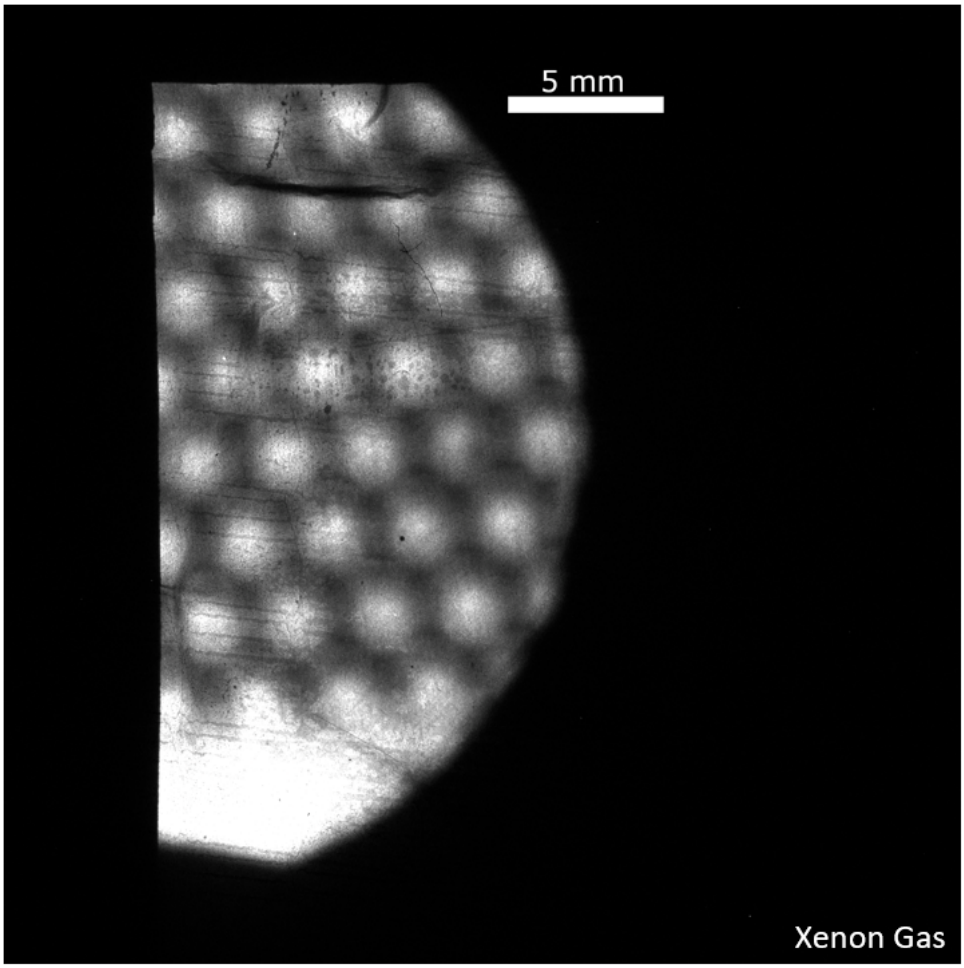

Figure 4.44: Mesh full plasma 2022-02-18. [2022-02-18, Shots 226-230, 8 J, 600 fs^2, Ave 46 fs, Ave $1.3 \times 10^{15} W/cm^2$, Xenon, 21 bar, 21 ms, 5.6 mm, 50 mm, 8 mm, Mesh 2]

The perforated mesh can therefore be used as a means of identifying the contribution of hot plasma to the measured conversion efficiency and subtracting that to achieve a more accurate estimate of conversion efficiency. In order to estimate the hot plasma contribution, the difference between the reading between the mesh holes and the background reading away from the mesh was taken resulting in figure 4.45. This figure shows the background subtracted signal between mesh holes as a function of laser intensity and with laser energies of 2, 4, and 8 J plotted separately. As discussed in section 4.4.2 the

formation of a plasma is more reliant on the laser energy than the intensity as a whole due to the spatial modulation of the beam. This is why there is such a significant difference between the measurements at different laser energies in figure 4.45. The data in this figure does show a general increase with laser intensity although the 4 J scan seemingly peaks at $1.6 \times 10^{14} W/cm^2$ and then decreases. For simplicity the average of the available points (0.30, 0.54, and 1.57 counts for 2, 4, and 8 J respectively) will be used to subtract from the reading at these energy levels in order to account for the effect of plasma on the conversion efficiency.

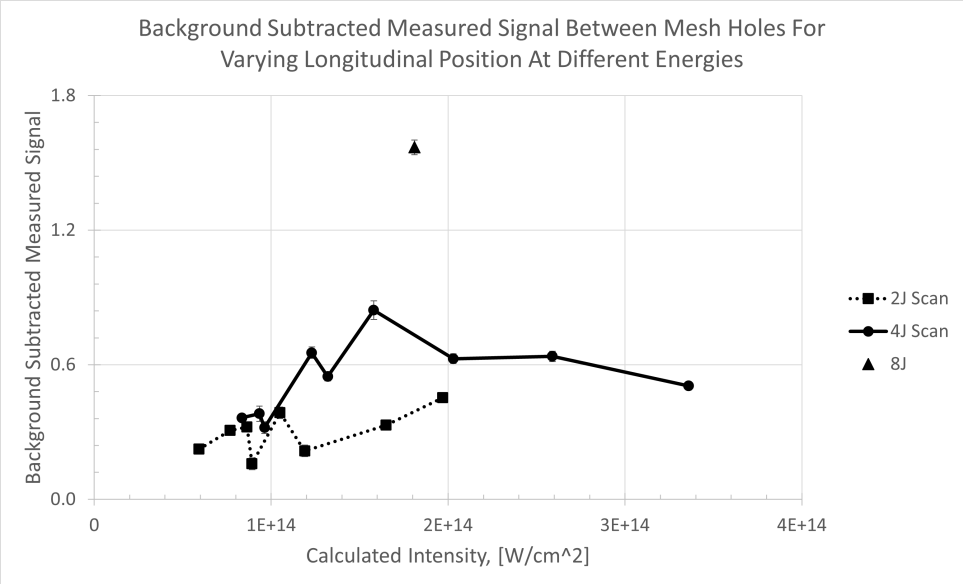

Figure 4.45: Measured signal between holes (background subtracted) as a function of laser intensity at the nozzle. The solid line with circles is the 4J scan, the dotted line with squares is the 2J scan, and the single triangle point is the 8J scan. Laser energies of 2, 4, and 8 J are plotted. Scans moving the nozzle further from laser focus were conducted for both the 2 and 4 J case resulting in various measurements of intensity, no scan was performed for the 8 J case. [2022-02-09, Shots 93-131, 2 J, 1400 fs^2, Ave 59 fs, Varying, Argon, 31 bar, 22 ms, 6 mm, Varying, 8 mm, Mesh 2], [2022-02-10, Shots 82-126, 8 J, 800 fs^2, Ave 43 fs, Varying, Argon, 31 bar, 22 ms, 10 mm, Varying, 8 mm, Mesh 2], [2022-02-11, Shots 202-206 and 207-211, 8 J, 600 fs^2, Ave 50.5 fs, Ave $1.8 \times 10^{14} W/cm^2$, Argon, 46 bar, 22 ms, 8 mm, 130 mm, 8 mm, Mesh 1 and Mesh 2]

4.7 Step Wedge

On the same translation stage as the XUV diodes is the step wedge. The step wedge is formed by two overlapping 0.8 um thickness Aluminum filters stacked in such a way that there are regions where there is no filter, one filter, and two filters. The step wedge can be moved into the beam to provide images as seen figure 4.46. This figure shows the step wedge on the left and the absence of the step wedge in the center. In addition a table showing the attenuation of the beam intensity at several highlighted points is shown on the right. The step wedge acts as a method to verify the presence of XUV. Since XUV light passes through an Al filter but visible light does not, moving the step wedge into the beam can verify that the light observed is XUV rather than visible light coming from holes in the existing filters. The attenuation of the XUV passing through the filters can

also confirm that the CCD is reading XUV. Within the expected wavelengths the XUV will be attenuated by approximately $10^{d_{Al}}$, where d_{Al} is the thickness of the aluminum filter in microns. This is derived from the transmission plot of Al as shown in figure 4.23. Therefore a 0.8 um Al filter attenuates the XUV by approximately $\sim 10^{0.8}$ which is equal to 6.31, while the 1.6 um filter attenuates light by $\sim 10^{1.6}$ which is equal to 39.81 so these are the expected values.

The attenuation from a filter can be determined by dividing the intensity without the filter by the intensity with a filter at the same spot. As seen in the table of figure 4.46 points 1 and 2 are a little below 1.0 so the shot without the filter seems to be a little less intense in these spots than the shots with the filter (although the overall calculated intensity is slightly larger for the shots without the filter than for the shots with the filter). Point 3 is 4.62 which is lower than the expected 6.31 but given the decrease in intensity this seems reasonable. Point 4 is a bit lower at 3.62 however, this is on a dark spot and therefore some of the data is being lost amongst the background. For the region with two filters point 5 is overtop a piece of debris on the CCD which explains the low attenuation. Point 7 is fairly close at 31.01 but point 6 is further off at 19.43. Overall, due to shot to shot variation in the spatial modulation, it is very difficult to get precise results from the step wedge but a general decrease as the number of filters increase is observed.

The XUV is definitely being attenuated by the filters which confirms that what is observed on the CCD is not leaked visible light but is light that can pass through an Al filter indicating XUV. The exact attenuation values do not line up exactly as expected but this may be attributable to error due to the spatial modulation and fluctuations in soht to shot intensity.

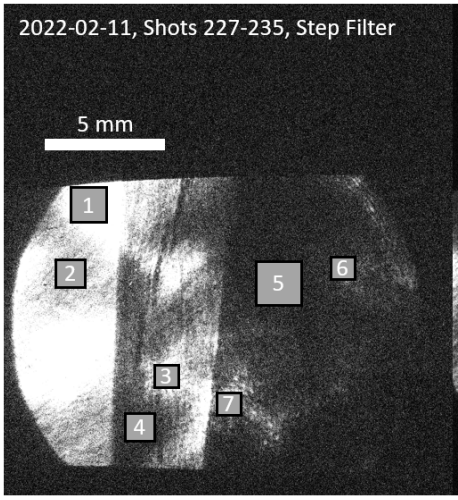

Point	Attenuation
1	0.77
2	0.92
3	4.62
4	3.62
5	4.26
6	19.43
7	31.01

Figure 4.46: CCD with step wedge (left), CCD without step wedge (center), and table with attenuation at the various highlighted points. [2022-02-11, Shots 227-235, 8 J, 800 fs^2, Ave 60.5 fs, Ave $1.4 \times 10^{14} W/cm^2$, Argon, 46 bar, 22 ms, 8 mm, 130 mm, 8 mm, Step Wedge], [2022-02-11, Shots 236-240, 8 J, 800 fs^2, Ave 57.6 fs, Ave $1.5 \times 10^{14} W/cm^2$, Argon, 46 bar, 22 ms, 8 mm, 130 mm, 8 mm, Nothing]

4.8 Conversion Efficiency

In order to obtain a better understanding of how efficient the FCHHG geometry is, the scaling of conversion efficiency versus nozzle position, gas pressure, and dazzler setting was studied.

Both the XUV diodes and the CCD camera were used to determine the conversion efficiency from the input laser energy to XUV. First, the size of the beam at the XUV diodes and the CCD camera was determined through simple geometry. The known size of the beam before focusing (220 mm) and the known focal length (2.5 m) were used to determine the cone angle of the input beam (5°). Then the known distance from TCC to the diode or CCD (2.18 m for XUV2, 3.00 m for CCD) was used to determine the radius of the beam at that position. It is assumed that the beam expands as a perfect circle allowing the area to be calculated from the known radius. Then, by multiplying by the laser energy, the energy per unit area of the full XUV beam is determined.

The XUV diode has a reading in Volts and a response similar to the example shown in figure 4.47. The average of the plateau region after the laser pulse at zero seconds is taken as the reading from the photodiode. This can be divided by the $1M\Omega$ termination in the oscilloscope line to determine current. The RC time constant is found by multiplying the $1M\Omega$ termination with the known capacitance of the XUV diode of 6 nF [39] to obtain a time constant of 6 ms. The charge in the capacitor can then be determined by multiplying the current by the RC time constant. This term is then divided by the area of the detector (1 cm^2) to obtain the charge per unit area. Based on the manufacturers data for an average photon energy of 40.5 eV (corresponding to 30.6 nm, the centroid of the harmonics from Shot 27 on 2022-02-22), there will be a factor of 3.6 eV of deposited energy needed for the formation of every electron-hole pair. [39] This translates into 0.28 C/J which can be used to divide the previously calculated charge per unit area to obtain energy per unit area. The last step is to take into account the attenuation of the aluminum filters protecting the XUV diodes by multiplying the energy per unit area by $10^{d_{Al}}$, where d_{Al} is the aluminum filter thickness in um. After this the energy per unit area from the detectors is divided by the energy per unit area from the incident laser beam to determine conversion efficiency.

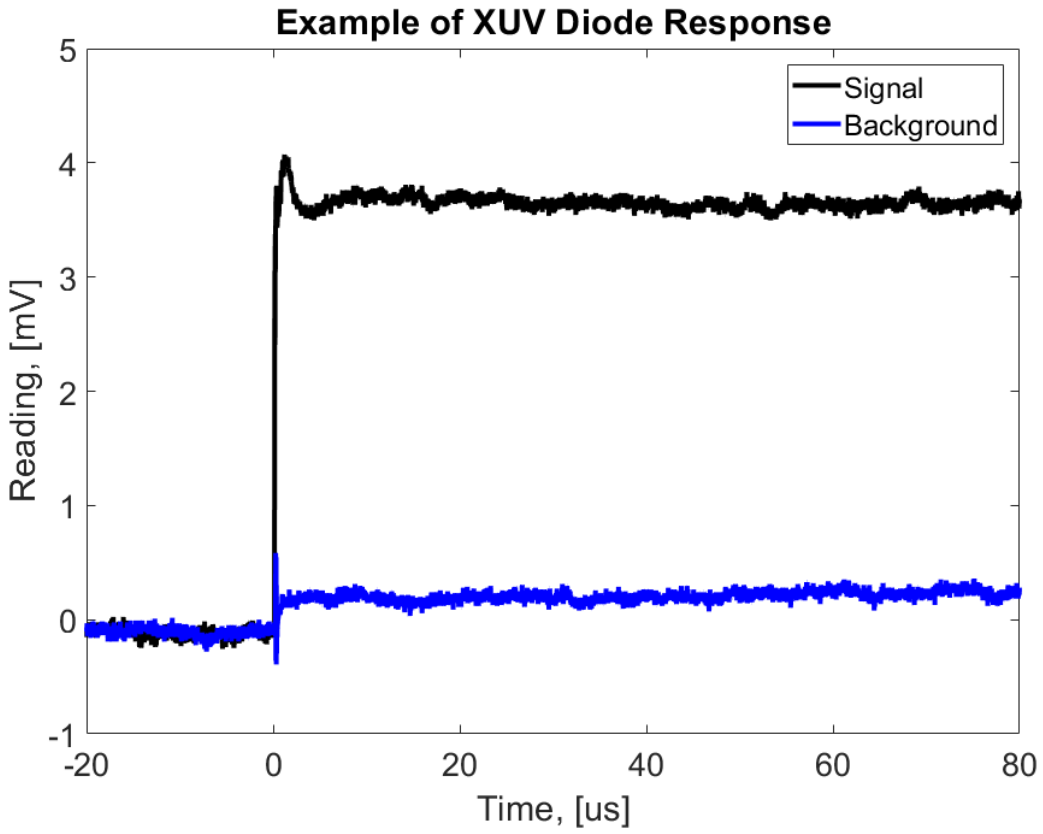

Figure 4.47: Example of the XUV diode response to the laser. The response with the gas turned on is shown in black and plateaus around 3.6 mV while the background response with the gas off is shown in blue and plateaus around 0.2 mV. [2022-02-10, Shots 219-223 and 67-71 as Background, 4 J, 800 fs^2, Ave 41.1 fs, Ave $2.2 \times 10^{14} W/cm^2$, Argon, 31 bar, 22 ms, 10 mm, 90 mm, 8 mm, Nothing]

The CCD signal is in counts rather than Volts. Counts are proportional to the number of electron-hole pairs created by photons incident on the CCD. This proportionality is determined by the gain setting of the camera. In this case the camera was set to high gain with an average factor of 0.73 electron-holes per count which the counts are multiplied by to obtain the electron-hole pairs. Before doing so, however, the contribution due to plasma formation discussed in section 4.6.3 should be subtracted to obtain more accurate results. The electron-hole pairs are divided by the area of the CCD being examined and converted into Coulombs to obtain Coulombs per unit area. In order to convert the charge per unit area into energy per unit area the quantum efficiency of the CCD must be determined. A plot of quantum efficiency of the CCD for varying wavelengths is provided in reference [40]. Using 30.6 nm, as was done with the XUV diode, provides a quantum efficiency of 0.69. This means that 69% of photons at this wavelength will interact with the CCD while 31% will not. The Silicon in a CCD requires $\sim 3.6eV$ to create a single electron-hole pair. Therefore the energy of the XUV required per electron hole pair is 3.6 eV / 0.69 e-h, or 5.20 eV/e-h. This translates to an 0.19 C/J which allows for the energy per unit area of the XUV beam to be found. After this the attenuation of the Al filters is accounted for and the result is divided by the energy per unit area of the full beam to obtain conversion efficiency.

Due to the filters protecting the CCD, much of it is obscured in every shot. If the full area of the CCD were used for the conversion efficiency calculation this would offset results. Therefore, a truncated version of the CCD is used when determining conversion efficiency. Additionally, due to the spatial modulation of the XUV, it is of interest to examine the conversion efficiency resulting from hot spots and so an even more truncated version of the CCD focused on a single hot spot is used for this.

4.8.1 Gas Jet Delay Dependence

The overall delay of the laser from the trigger to the shot reaching the target chamber is 30 ms. The gas jet is delayed with respect to this setting so a delay of 25 ms corresponds to the solenoid on the gas jet opening 5 ms before the laser reaches the chamber. The gas jet is open for 7 ms and then closes. Figure 4.48 shows the scaling of CCD conversion efficiency with varying gas jet delay for xenon gas. A rapid initial rise is seen up to a peak at 8 ms followed by a slow decrease. Since the solenoid closes at 7 ms this result makes sense. This is also somewhat different than what was seen in figure 3.12 which shows a slower increase and a rapid decrease but it is important to remember that these are both looking at different axes of the nozzle.

Most of the measurements in which pressure scaling is investigated are performed with a delay of 22 ms corresponding to the laser entering the chamber 8 ms after the gas jet fires. Therefore, for these measurements, the 3D integrated result is scaled to 8 ms using the data from figure 3.11. This corresponds to a scaling factor of 37.8 for the 2D simulation and a scaling factor of 64 for the 3D simulation. Since the solenoid is still open at 8 ms for these interferometry measurements, this likely overestimates the gas density somewhat.

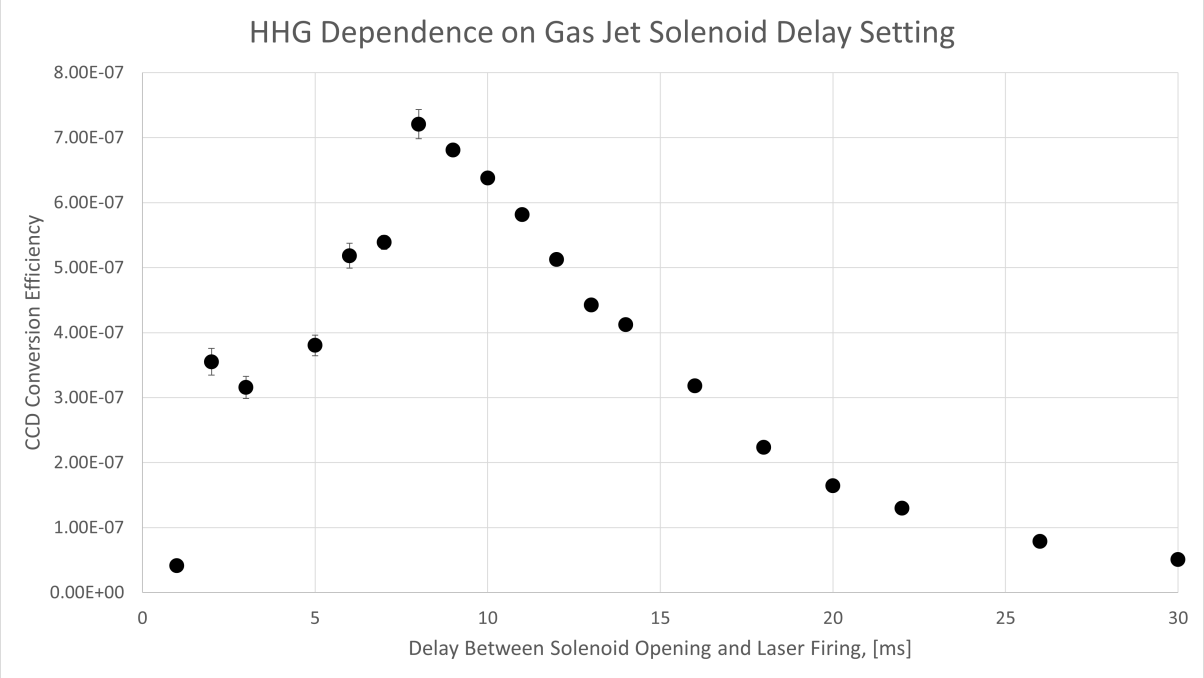

Figure 4.48: Scaling of the CCD conversion efficiency as a function of gas jet delay. Gas used for this scan is Xenon. [2022-02-18, Shots 18-125, 4 J, 800 fs^2, Ave 55.3 fs, Ave $1.5 \times 10^{14} W/cm^2$, Xenon, 20 bar (decreased over time), Varying, 7 mm, 130 mm, 8 mm, Nothing]

4.8.2 Pressure Dependence

HHG dependence on backing pressure as measured by both the XUV photodiode and the Xray CCD is shown in figure 4.49. The general trend is that a higher backing pressure results in a higher conversion efficiency. The left vertical axis is the XUV diode conversion efficiency while the right vertical axis is Xray CCD conversion efficiency. The XUV diode measurements achieve conversion efficiencies on the order of 10^{-7}. The CCD measurements achieve efficiencies around 10 times higher, on the order of 10^{-6}. The reason for this difference is because the CCD is in the center of the beam which results in it being exposed to a higher overall intensity. Additionally, due to spatial modulation, the XUV diode may be only exposed to relatively dim spots while the CCD will see some dim spots and some bright spots.

While the lower horizontal axis displays backing pressure, the upper horizontal axis displays the integrated isothermal pressure dervied from the 3D simulation in section 3.5 scaled to 8ms as mentioned in section 4.8.1. From this it can be seen that distance-pressure products between 21 and 217 mm-mbar are achieved. This range is higher than Nayaks predicted optimum HHG at a distance-pressure product of 37.5 mm-mbar [11]. Nayaks result predicts that conversion efficiency plateaus for distance-pressure products higher than this so it would be expected that the measured data would show a peak at the lowest integrated isothermal pressure values and then a plateau afterward. What is observed, however, is a continual increase of conversion efficiency as backing pressure increases as shown in figure 4.49. This result appears to be in conflict with the predicted

behaviour from [11]. It is not necessarily clear why this is the case but some explanations are proposed in the discussion section for this chapter.

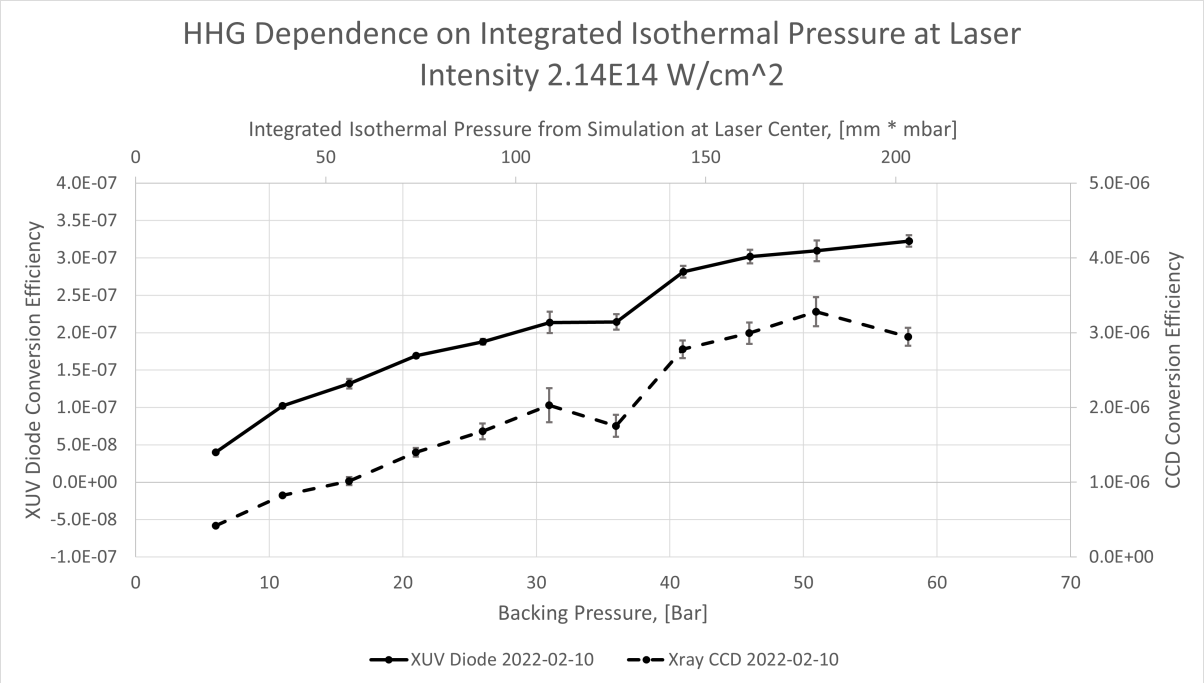

Figure 4.49: Dependence of the HHG on backing pressure. The solid line is the conversion efficiency as determined by the XUV diode, while the dashed line is the conversion efficiency as determined by the CCD camera. On the left axis is the XUV diode conversion efficiency and on the right is the CCD conversion efficiency. On the bottom axis is the backing pressure while on the top is the integrated isothermal pressure dervied from the 3D simulation. [2022-02-10, Shots 219-278, 4 J, 800 fs^2, Ave 43.1 fs, Ave $2.1 \times 10^{14} W/cm^2$, Argon, 31 bar, 22 ms, 10 mm, 90 mm, 8 mm, Nothing]

In order to investigate the impact spatial modulation is having on the calculated conversion efficiency a single bright spot was isolated on the CCD and the conversion efficiency for it plotted in figure 4.50. The XUV diode data from figure 4.49 is also shown for reference. When isolating this bright spot conversion efficiencies on the order of 10^{-5} are achieved on the CCD. This leads to values an average of 3.3 times greater than what was seen for the conversion efficiency of the full image.

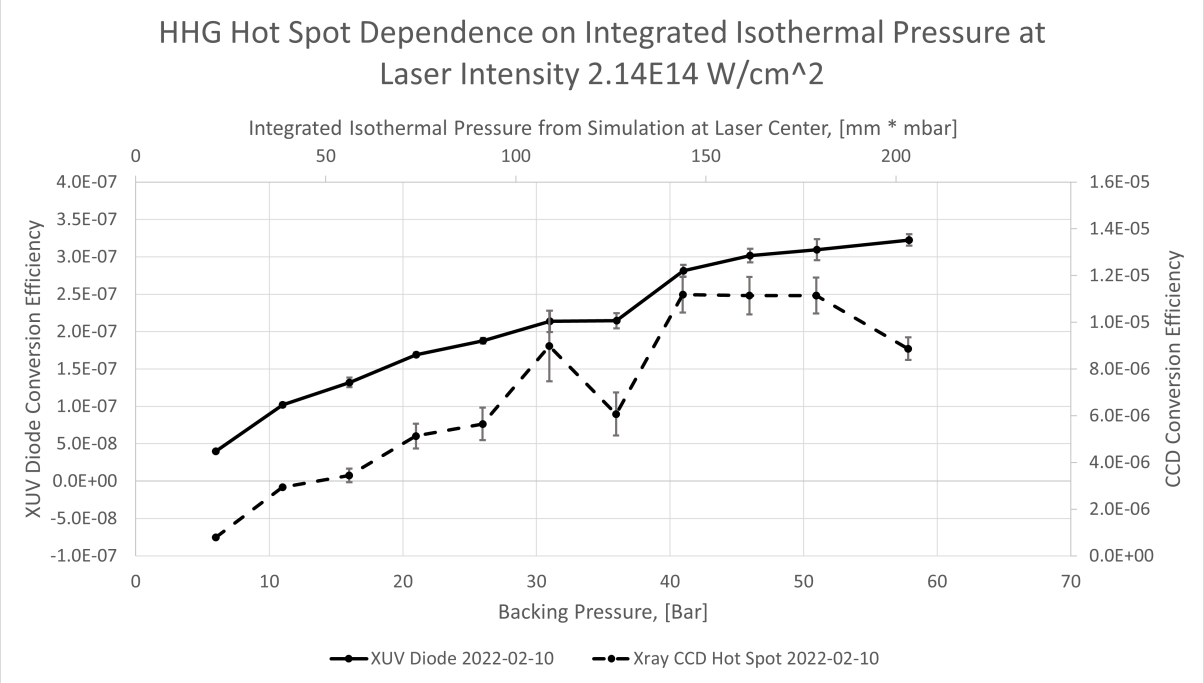

Figure 4.50: Dependence of the HHG on backing pressure around a single bright spot. The solid line is the conversion efficiency as determined by the XUV diode, while the dashed line is the conversion efficiency as determined by the CCD camera. On the left axis is the XUV diode conversion efficiency and on the right is the CCD conversion efficiency. On the bottom axis is the backing pressure while on the top is the integrated isothermal pressure dervied from the 3D simulation. [2022-02-10, Shots 219-278, 4 J, 800 fs^2, Ave 43.1 fs, Ave $2.1 \times 10^{14} W/cm^2$, Argon, 31 bar, 22 ms, 10 mm, 90 mm, 8 mm, Nothing]

Several different pressures scans are shown in figure 4.51. Only the Xray CCD measurements are shown from the 2022-02-08 scan as the XUV diode readings were below background. Additionally, mesh 1 was in the beam path for the 2022-02-08 scan so the Xray CCD data is scaled based on the mesh fill factor (42% [43]). The presence of the mesh here may impact the accuracy of this measurement somewhat.

In all of these lineouts the same general upward trend is observed, similar conversion efficiencies are observed between measurements as well. The 2022-02-08 shots have a laser energy of 2 J and a calculated intensity of $1.9 \times 10^{14} W/cm^2$, the 2022-02-10 shots have a laser energy of 4 J and a calculated intensity of $2.1 \times 10^{14} W/cm^2$, and the 2022-02-11 shots have a laser energy of 8 J and a calculated intensity of $1.4 \times 10^{14} W/cm^2$. Based on this it appears neither laser energy nor intensity have a large impact on how the conversion efficiency scales with backing pressure.

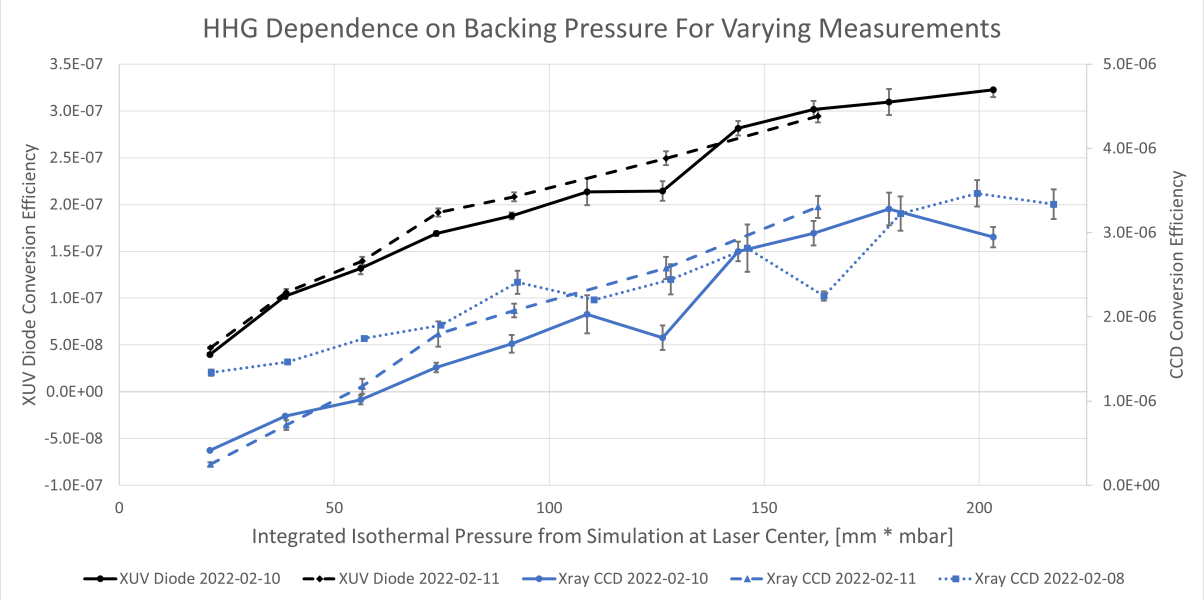

Figure 4.51: Dependence of the HHG on backing pressure for varying measurements. XUV diode measurements are shown in black with the solid line being the XUV diode measurement on 2022-02-10 and the dashed line being the XUV diode measurement on 2022-02-11. The Xray CCD measurements are shown in blue with the solid line being the CCD measurement on 2022-02-10, the dashed line being the CCD measurement on 2022-02-11, and the dotted line being the CCD measurement on 2022-02-08. The measurement from 2022-02-08 had mesh 1 in the path of the beam and was corrected based on the fill factor of the mesh (42% [43]). [2022-02-08, Shots 98-131, 2 J, 1000 fs^2, Ave 77.7 fs, Ave $1.9 \times 10^{14} W/cm^2$, Argon, Varying, 22 ms, 4 mm, 50 mm, 8 mm, Mesh 1], [2022-02-10, Shots 219-278, 4 J, 800 fs^2, Ave 43.1 fs, Ave $2.1 \times 10^{14} W/cm^2$, Argon, Varying, 22 ms, 10 mm, 90 mm, 8 mm, Nothing], [2022-02-11, Shots 96-140, 8 J, 800 fs^2, Ave 61.5 fs, Ave $1.4 \times 10^{14} W/cm^2$, Argon, Varying, 22 ms, 8 mm, 130 mm, 8 mm, Nothing]

4.8.3 Dependence On Nozzle Offset From Laser Axis

HHG dependence on the nozzle distance from the laser axis for a scan conducted on 2022-02-10 is shown in figure 4.52. The integrated density falls off slowly as it slowly spreads out transversely. In fact, for distances from 8 to 18 mm the conversion efficiency plateaus suggesting that the integrated gas density stays close to constant in this region. There is a slight downward slope in this region but it is less than the region from 20 - 26 mm. For distances less than 6 mm from the beam center there is a spike which seems to violate this idea. Perhaps there is a higher overall density at this point, another possibility is that the laser is clipping the nozzle slightly. The beam radius at this point is 3.96 mm providing only 2 mm distance from the nozzle. There is likely some larger than desired spread to the beam as well which may lead to low energy portions hitting the nozzle and forming a small plasma resulting in a higher reading at this point (although no plasma is observed on the CCD). At 20 mm the conversion efficiency starts to fall off as the spread of the gas causes the density to fall off transversely.

Conversion efficiencies on the order of 10^{-7} are seen for XUV diode while efficiencies on the order of 10^{-6} are seen for the Xray CCD. This is largely in line with what was observed in the previous section. The backing pressure here is 31 bar which had conversion efficiencies of 6.6×10^{-7} and 2.1×10^{-6} for the XUV diode and Xray CCD respectively. The average conversion efficiency in figure 4.52 is 5.4×10^{-7} and 1.66×10^{-6} for the XUV

diode and Xray CCD respectively showing that similar values are retained.

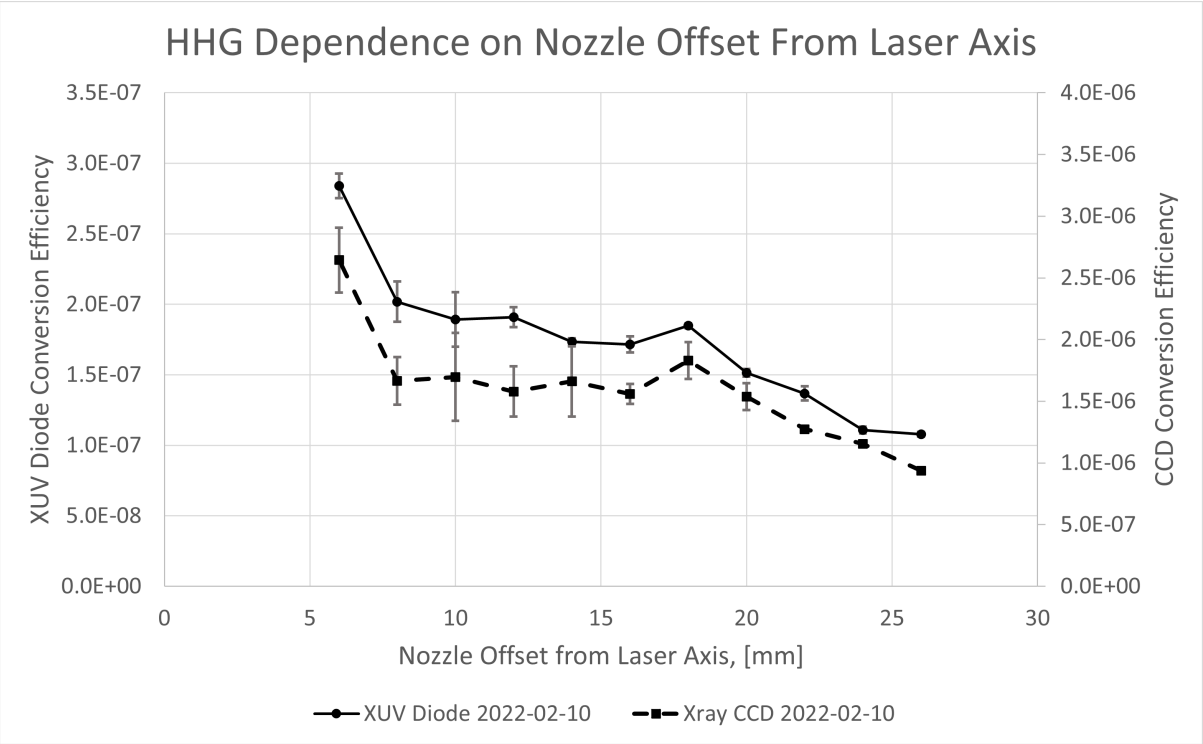

Figure 4.52: Dependence of the HHG on nozzle distance from beam center. The solid line is the XUV diode measurement and the dashed line the Xray CCD measurement. [2022-02-10, Shots 190-218, 4 J, 800 fs^2, Ave 43.5 fs, Ave 2.2 × $10^{14} W/cm^2$, Argon, 31 bar, 22 ms, Varying, 90 mm, 8 mm, Nothing]

Another scan of nozzle distance from laser axis was performed on 2022-02-09 and is shown in figure 4.53 alongside the Xray CCD measurement from 2022-02-10. Mesh 2 was in the beam path so the CCD data was scaled based on the fill factor of the mesh. The data has a somewhat higher conversion efficiency than the 2022-02-10 case but this may just be an overcorrection from the fill factor scaling. The XUV diode readings were below background in these shots so data from them is not included.

There is a general slope across the entire region rather than the steep slope and plateau which were seen in the 2022-02-10 case. Additionally, this was scan was performed with a beam diameter of almost half of the one on 2022-02-10 and so the data is more localized around the center of the beam. From the 3D simulation it would seem that a beam of this size in the scanned positions would not encounter a high density ridge or enter the low density region outside of the main gas jet. This seems to agree with the measured data as there is only a slow decrease in conversion efficiency rather than the sharper changes seen in the 2022-02-10 case. This indicates that the 2022-02-09 case is operating entirely within the plateau region seen in the 2022-02-10 case. From this data, it is clear that there is still a noticeable loss in gas density that occurs when varying the nozzle distance from the beam even inside the plateau region. From the comparison it is more noticeable that the plateau region in 2022-02-10 data has a slight slope until it reaches 18 mm from

the beam at which point it has a slight peak. This peak may be the result of shock waves creating a locally high density region which the edge of the beam is interacting with. Compared to the areas with steep slopes the plateau region in the 2022-02-10 case and the entirety of the 2022-02-09 case offer much more uniform gas density targets even if there is a slow decay.

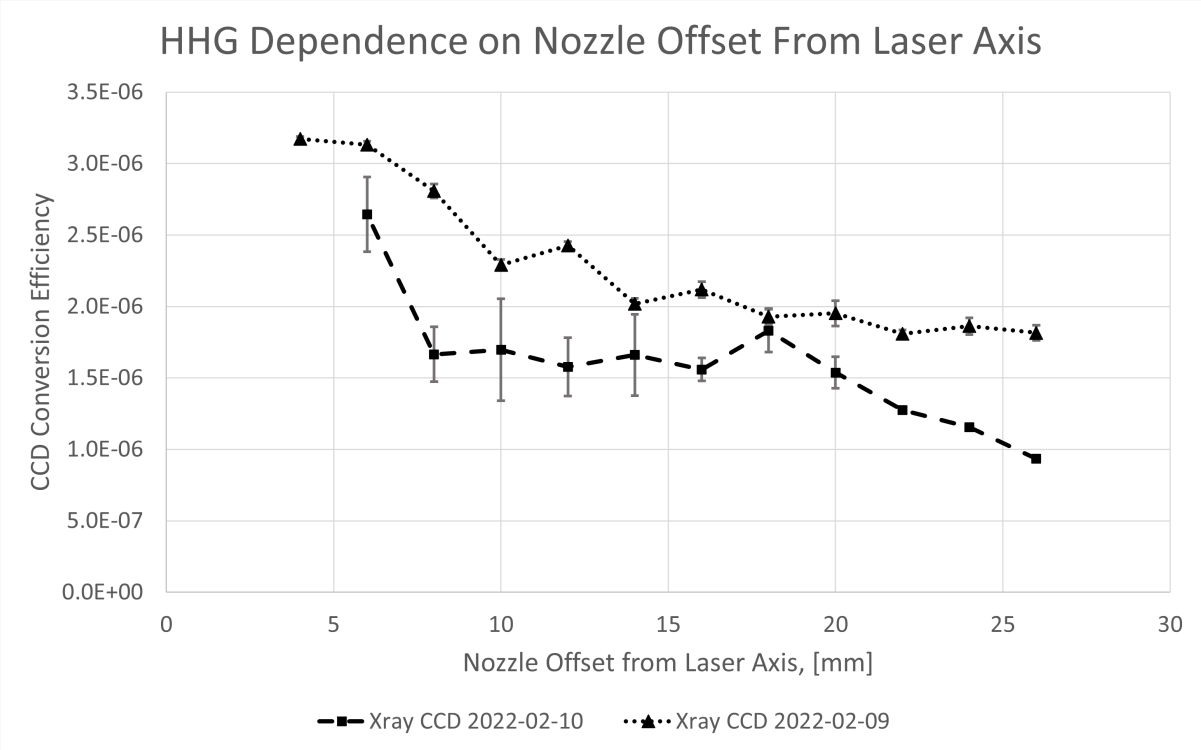

Figure 4.53: Comparison of the conversion efficiency for scans of the nozzle distance from laser axis on 2022-02-09 and 2022-02-10. The dashed line is the CCD measurement from 2022-02-10 and the dotted line is the CCD measurement from 2022-02-09. The 2022-02-10 case is the same as CCD data in figure 4.52. The 2022-02-09 case was done when Mesh 2 was in the beampath and has been corrected based on the fill factor of the mesh (42% [43]). As such the conversion efficiency is less than it should be and some information may be lost. [2022-02-10, Shots 190-218, 4 J, 800 fs^2, Ave 43.5 fs, Ave $2.2 \times 10^{14} W/cm^2$, Argon, 31 bar, 22 ms, Varying, 90 mm, 8 mm, Nothing], [2022-02-09, Shots 21-81, 2 J, 1000 fs^2, Ave 39.3 fs, Ave $3.6 \times 10^{14} W/cm^2$, Argon, 31 bar, 22 ms, Varying, 50 mm, 8 mm, Mesh 2]

Comparing to the simulation in figure 3.18 the initial plateau region lines up well with the simulation predicting a uniform density in the center of the nozzle, the high density region on the edges then provides the slight bump seen at 18 mm, and the low density region after this leading to the sharper decrease afterward. However, when integrating through the 3D model, this does not line up quite as well. An integration through the 3D gas jet for the 2022-02-10 case previously discussed provides the solid line in figure 4.54. This is an almost linear line, quite different to what is observed in figure 4.52. Another integration is performed, this time with the beam shifted 4.5 mm to the side of the nozzle and the beam size reduced to 4.4 mm (from 7.9 mm). This provides the dashed plot in figure 4.54 which matches up well with the plot seen in figure 4.52. These adjustments are well beyond the possible error in the nozzle position so the nozzle would not actually be seeing this density profile. However, the 3D model is rather coarse and loses much of

the finer details of the gas flow. It may very well be the case that density modulations, similar to what is seen in the dashed line, are present within the region that the beam passes through but these are not picked up in the simulation due to the coarseness of the mesh. Considering how well the dashed line matches with the measured data it seems likely that this is the case.

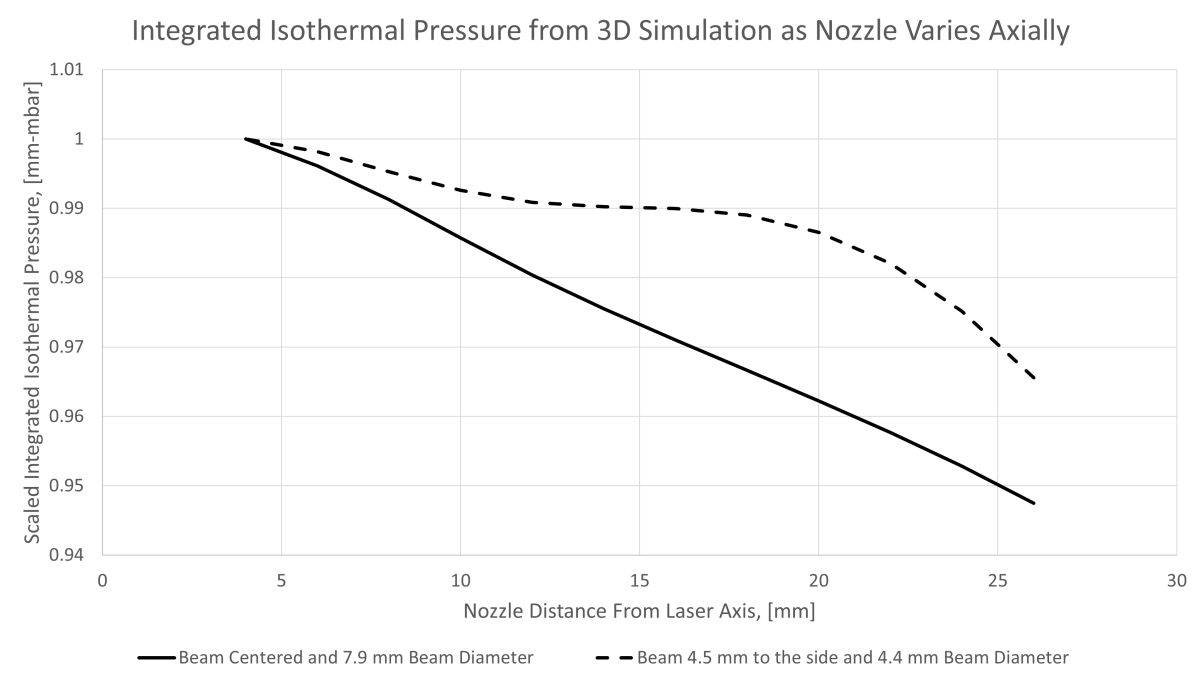

Figure 4.54: 3D simulation, average integrated density seen by the beam for parameters: [2022-02-10, Shots 190-218, 4 J, 800 fs^2, Ave 43.5 fs, Ave $2.2 \times 10^{14} W/cm^2$, Argon, 31 bar, 22 ms, Varying, 90 mm, 8 mm, Nothing]. The solid line is the unmodified case while the dashed line is the case for moving the beam 4.5 mm to one side of the nozzle and decreasing the beam size to 4.4 mm (from 7.9 mm).

4.8.4 Nozzle Distance From Laser Focus Dependence

HHG dependence on the distance of the nozzle from laser focus is shown in figures 4.55, 4.56, 4.57. These are from scans performed on several different days and with laser energies of 2, 4, and 8 J respectively. Figure 4.55 had a mesh in the beam path so the conversion efficiency was scaled based on the fill factor of the mesh. Figure 4.57 required that the nozzle be moved further from the laser axis in order to avoid clipping with the nozzle at distances far from laser focus. The nozzle was moved from its original position of 10 mm from the laser axis to 12 and then 14 mm from the beam for the points at 200, 220, and 240 mm from laser focus. To account for this these points were scaled using the nozzle distance from laser axis data of figure 4.52.

The 2 J case appears to reach a maximum conversion efficiency at around 60 mm from laser focus. The 4 J case appears to have a peak between 90 and 100 mm from laser focus but a sharp rise on the last data point at 70 mm indicates it may increase further at closer distances. The XUV diode in the 8 J case reaches peak conversion efficiency when the nozzle is 130 mm from laser focus and then decreases as the nozzle draws closer,

however, the CCD reaches its peak when the nozzle is 90 mm from laser focus. Since the spatial modulation is affected by the nozzles distance from laser focus it is possible that at 130 mm a bright spot was on the XUV diode but as the distance was decreased that spot moved. It also looks as though the conversion efficiency may be plateauing for nozzle positions between 90 and 130 mm as neither the XUV diode or CCD are changing rapidly in this region.

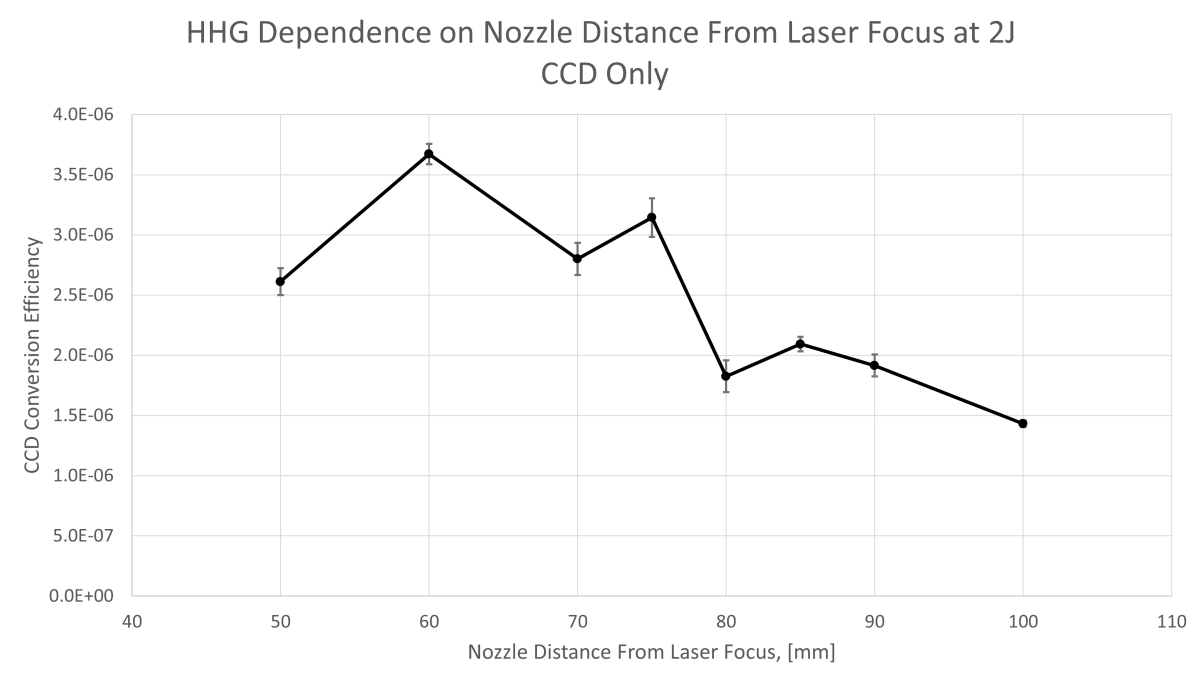

Figure 4.55: Dependence of the HHG on nozzle distance from laser focus for shots on 2022-02-09 conducted at 2 J. A mesh was in the beampath so the conversion efficiency was corrected based on the fill factor of the mesh (42% [43]). [2022-02-09, Shots 93-131, 2 J, 1400 fs^2, Ave 59.2 fs, Ave $1.1 \times 10^{14} W/cm^2$, Argon, 31 bar, 22 ms, 6 mm, Varying, 8 mm, Mesh 2]

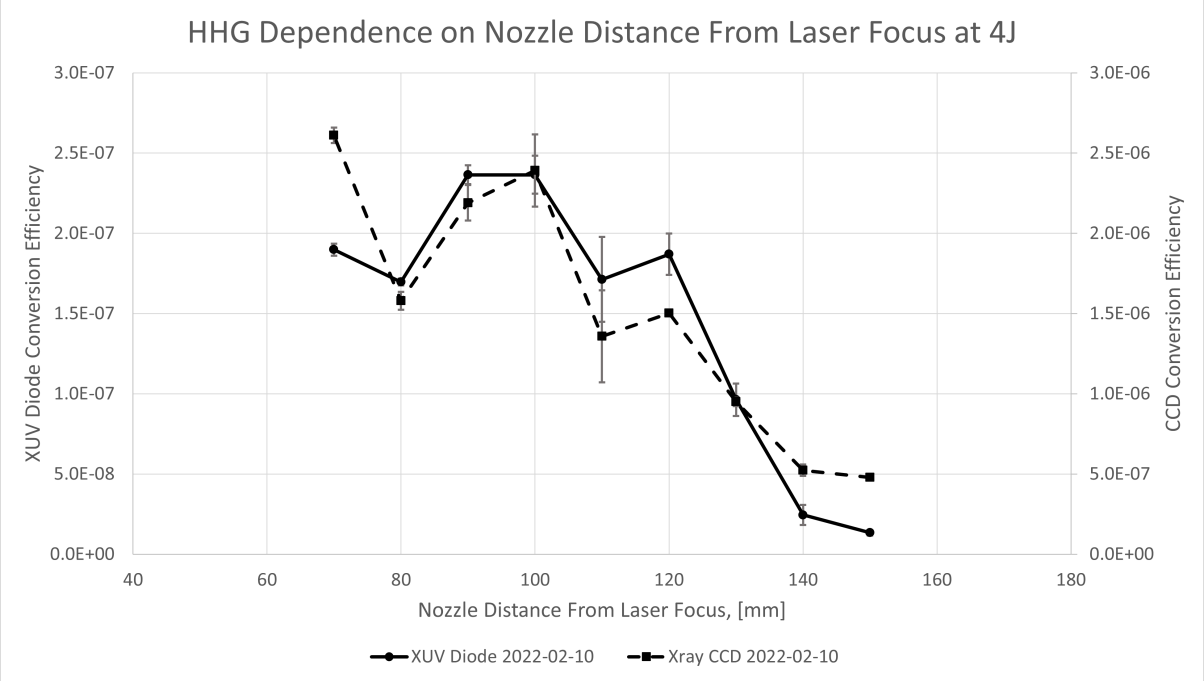

Figure 4.56: Dependence of the HHG on nozzle distance from laser focus for shots on 2022-02-10 conducted at 4 J. The solid line is the XUV diode measurement and the dashed line is the Xray CCD measurement. [2022-02-10, Shots 129-147, 4 J, 800 fs^2, Ave 39 fs, Ave $1.8 \times 10^{14} W/cm^2$, Argon, 31 bar, 22 ms, 10 mm, Varying, 8 mm, Nothing]

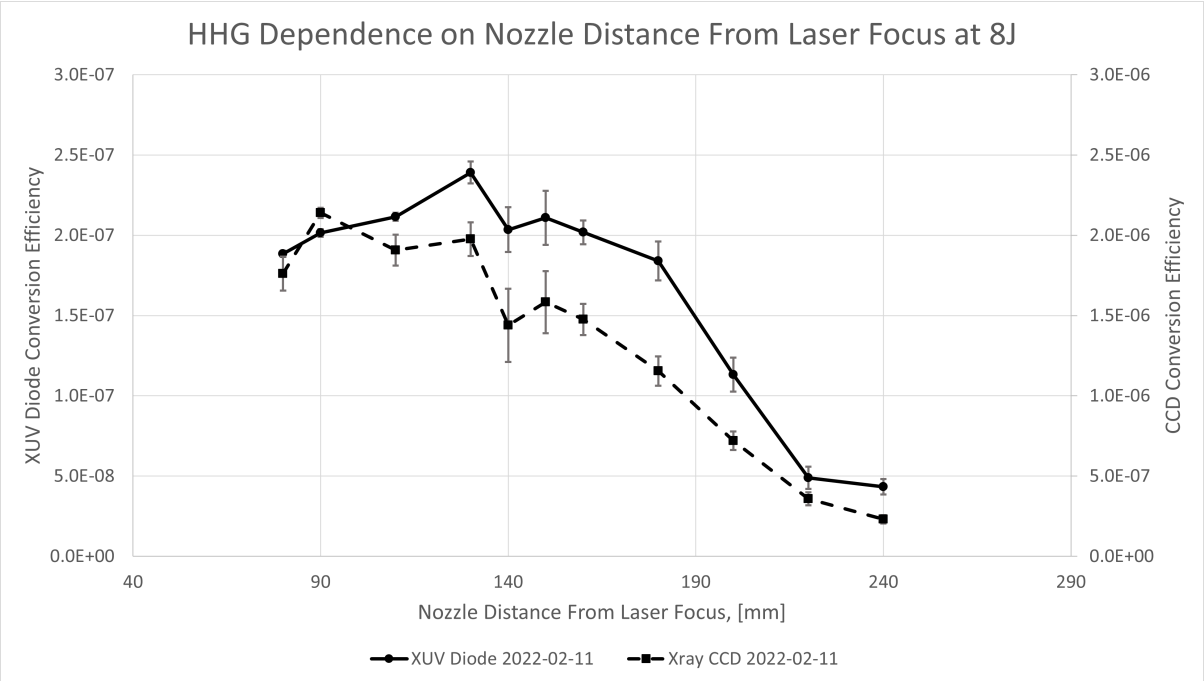

Figure 4.57: Dependence of the HHG on nozzle distance from laser focus for shots on 2022-02-11 conducted at 8 J. The solid line is the XUV diode measurement and the dashed line is the Xray CCD measurement. The nozzle was 10 mm from the laser axis for most shots but was varied to 12 and 14 mm for the points at 200, 220, and 240 mm from the laser focus. To account for this scaling from figure 4.52 was used to scaled these points. [2022-02-11, Shots 146-201, 8 J, 800 fs^2, Ave 55.6 fs, Ave $1.5 \times 10^{14} W/cm^2$, Argon, 36 bar, 22 ms, 10-14 mm scaled to 10 mm, Varying, 8 mm, Nothing]

Taking the CCD data from figures 4.55, 4.56, and 4.57 provides figure 4.58. The 2 J case achieves the highest conversion efficiencies although, as mentioned earlier, the

corrective factor for the mesh blocking the beam may be exaggerating the conversion efficiency somewhat. In section 4.8.6 the data here is examined again but as a function of laser intensity. From this latter analysis it does indeed seem that the scaling exaggerates the conversion efficiency. Despite issues with scaling, figure 4.58 shows how having a high laser energy allows for higher conversion efficiencies further from the laser focus. The 8 J case is clearly able to sustain strong conversion efficiencies even 200 mm from focus, while the lower energies fall off much more rapidly.

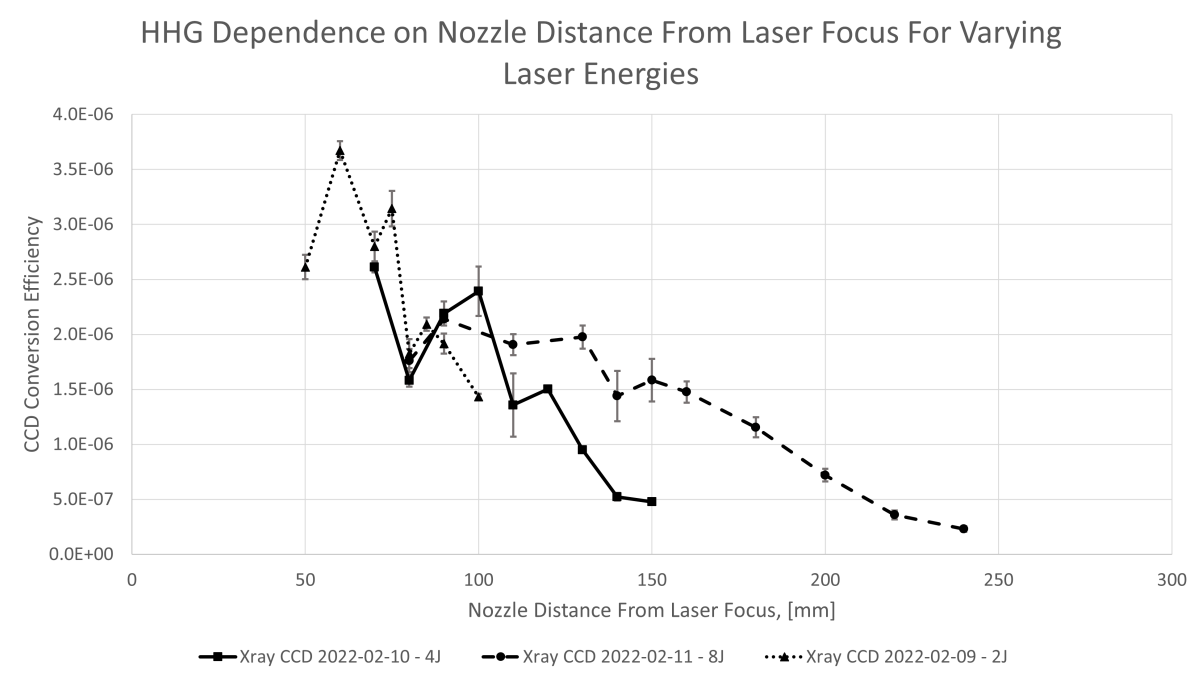

Figure 4.58: Dependence of the HHG on nozzle distance from laser focus for shots at varying laser energies. The solid line is the CCD measurement from 2022-02-10 at 4J, the dashed line is the CCD measurement from 2022-02-11 at 8J, and the dotted line is the CCD measurement from 2022-02-09 at 2J. [2022-02-09, Shots 93-131, 2 J, 1400 fs^2, Ave 59.2 fs, Ave $1.1 \times 10^{14} W/cm^2$, Argon, 31 bar, 22 ms, 6 mm, Varying, 8 mm, Mesh 2], [2022-02-10, Shots 129-147, 4 J, 800 fs^2, Ave 39 fs, Ave $1.8 \times 10^{14} W/cm^2$, Argon, 31 bar, 22 ms, 10 mm, Varying, 8 mm, Nothing], [2022-02-11, Shots 146-201, 8 J, 800 fs^2, Ave 55.6 fs, Ave $1.5 \times 10^{14} W/cm^2$, Argon, 36 bar, 22 ms, 10-14 mm scaled to 10 mm, Varying, 8 mm, Nothing]

The results of the averaged integrated 3D simulation are shown in figure 4.59. As nozzle moves further from focus the size of the beam interacting with it increases. Initially the integrated profile is a flat plateau, but as the beam size increases it begins to overlap with the high-density edge region, leading to an increase in the average integrated density. Once the beam is large enough to pass the high-density region the average value then falls off rapidly as the beam overlaps with the low-density region. The effects of this are not really seen in the data however. Because the intensity of the beam changes with longitudinal position, the relatively minor fluctuations in density predicted by the simulation are not enough to be noticeable when compared to the changes in intensity.

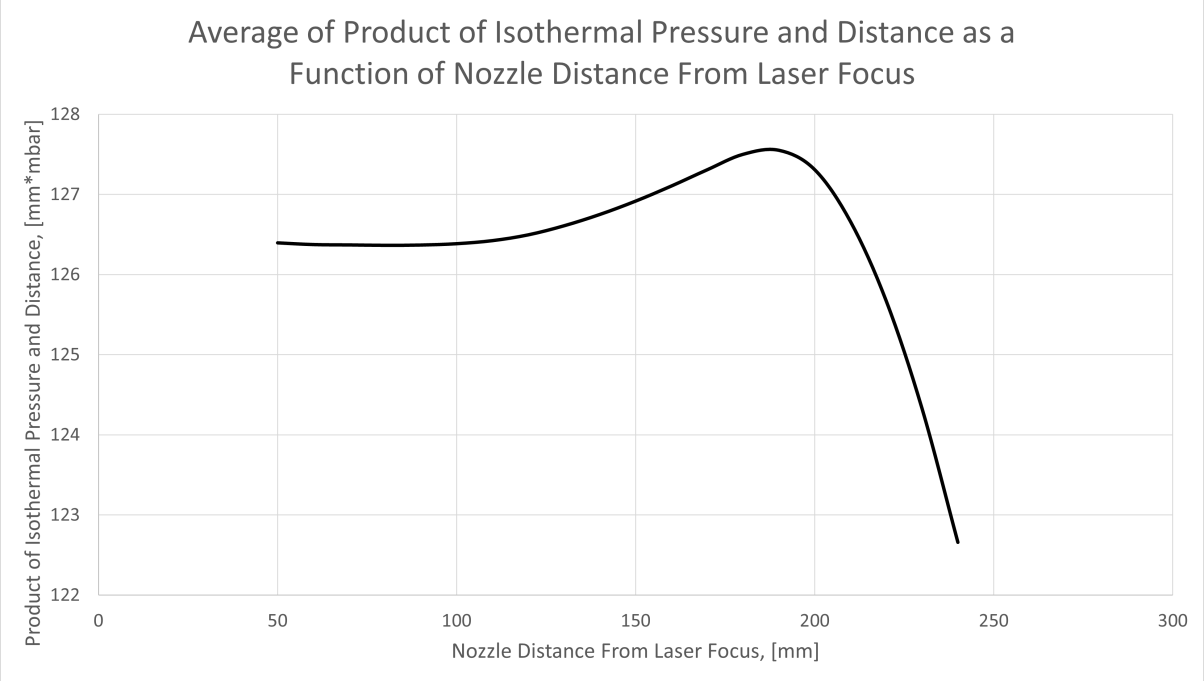

Figure 4.59: 3D simulation, average integrated density seen by the beam for varying the nozzle distance from focus. For parameters: [2022-02-11, Shots 146-201, 8 J, 800 fs^2, Ave 55.6 fs, Ave $1.5 \times 10^{14} W/cm^2$, Argon, 36 bar, 22 ms, 10-14 mm, Varying, 8 mm, Nothing]

4.8.5 Laser Pulse Width Dependence

In the front end of the laser the dazzler is used to control the pulse length of the beam. The pulse length is measured by an autocorrelator outside of the chamber but may be different from the pulse length inside the chamber. The dependence of the dazzler setting on HHG conversion efficiency is shown in figure 4.60. The dazzler base setting for recorded data was 17065 fs^2 and deviations from this are recorded as either positive or negative. Both the X-ray camera and CCD agree nicely indicating that maximum conversion efficiency is achieved at a dazzler setting of 17865 fs^2. There is an offset from the calculated intensity however. The calculated intensity predicts the strongest peak at a dazzler setting of around 17565 fs^2, 300 fs^2 off of the peak predicted by the conversion efficiency. The peak of the measured conversion efficiency should be in agreement with the peak intensity. These values conflicting perhaps indicates error in the measured value of pulse length by the autocorrelator.

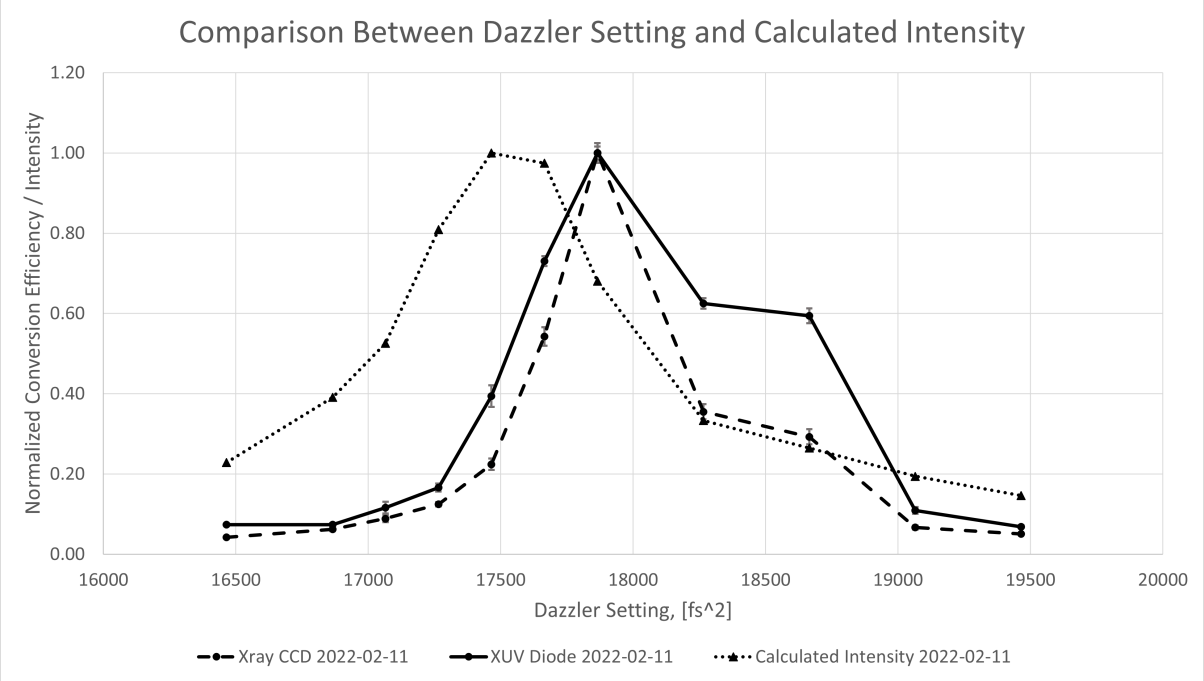

Figure 4.60: Comparison between the dependence of the HHG on dazzler setting at 6 J and the calculated intensity of the beam. The solid line is the XUV diode measurement, the dashed line is the CCD measurement, and the dotted line is the calculated intensity. [2022-02-11, Shots 30-90, 6 J, Varying, Ave 125.5 fs, Ave $9.93 \times 10^{13} W/cm^2$, Argon, 46 bar, 22 ms, 8 mm, 110 mm, 8 mm, Nothing]

Figure 4.61, shows the results of dazzler scans from 2022-02-10 and the previously seen 2022-02-11. The 2022-02-10 dazzler setting again peaks around 17865 fs^2. The conversion efficiency of the 2022-02-10 data is somewhat lower than the 2022-02-11 data. It is not clear why this might be but it may be the result of a difference in intensity. Unfortunately, some of the pulse length data for the 2022-02-10 shots was not recorded, making it difficult to come to any conclusions.

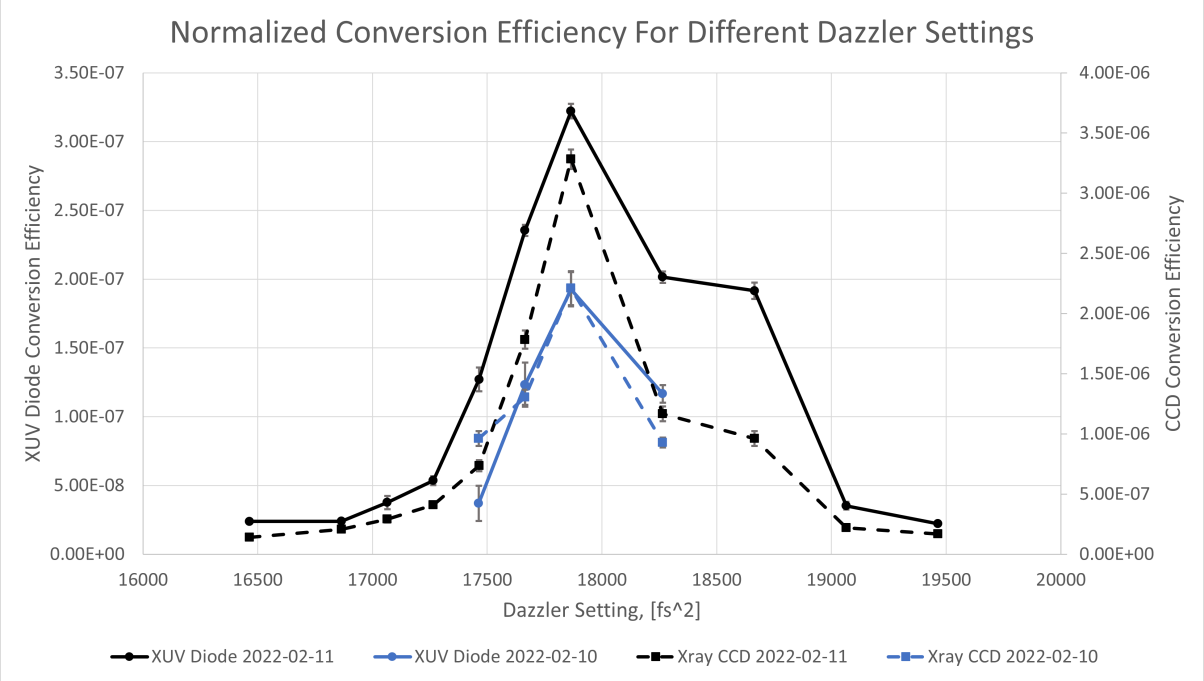

Figure 4.61: Normalized conversion efficiency for different measurements of dazzler setting. The black lines are from measurements on 2022-02-11 with the solid black line being the XUV diode measurement on 2022-02-11 and the dashed black line being the CCD measurement on 2022-02-11. The blue lines are from measurements on 2022-02-10 with the solid blue line being the XUV diode measurement on 2022-02-10 and the dashed blue line being the CCD measurement on 2022-02-10. [2022-02-11, Shots 30-90, 6 J, Varying, Ave 125.5 fs, Ave $9.93 \times 10^{13} W/cm^2$, Argon, 46 bar, 22 ms, 8 mm, 110 mm, 8 mm, Nothing], [2022-02-10, Shots 6-14 and 37-51, 2 J, Varying, Missing Data, Missing Data, Argon, 31 bar, 22 ms, 6 mm, 70 mm, 8 mm, Nothing]

4.8.6 HHG Dependence on Laser Intensity

In order to achieve HHG the intensity of the laser beam must be quite high, but not so high as to cause full ionization of the gas and the creation of a hot plasma. For lower laser energies some HHG will be created and this should continuosly increase until the point of plasma creation is reached. This was seen in figure 2.5, where the 15th harmonic of argon enters the plateau region at an intensity of $1 \times 10^{14} W/cm^2$ and ionization starts occuring at an intensity of $4 \times 10^{14} W/cm^2$. Obviously, there will be some differences due to the focal cone geometry and spatial modulation but this provides an estimate of intensity scaling. Due to time constraints during the experiment, no direct scan of the effects of laser energy was conducted. Instead, the scaling from the previous sections is applied to different data in order to normalize it and derive the scaling with laser energy.

The HHG dependence on pressure and nozzle distance from beam center seem largely unaffected by the laser intensity in terms of how conversion efficiency scales. However, the dazzler setting and the nozzle distance from focus both directly factor into the intensity calculation. As seen in figure 4.60 the conversion efficiency disagrees with the intensity calculation in regard to the ideal dazzler setting. Therefore, intensity scaling derived from variations in the dazzler setting will have errors. Instead the data from the longitudinal variation in figure 4.58 is examined as shown in figure 4.62. As mentioned before the

data from 2022-02-09 which was blocked by a mesh is scaled by the mesh fill factor and this may have thrown off the accuracy of the results. Both the data from 2022-02-10 and 2022-02-11 have similar conversion efficiencies but the data from 2022-02-09 is noticeably higher. All three results display a general increase in conversion efficiency as laser intensity increases.

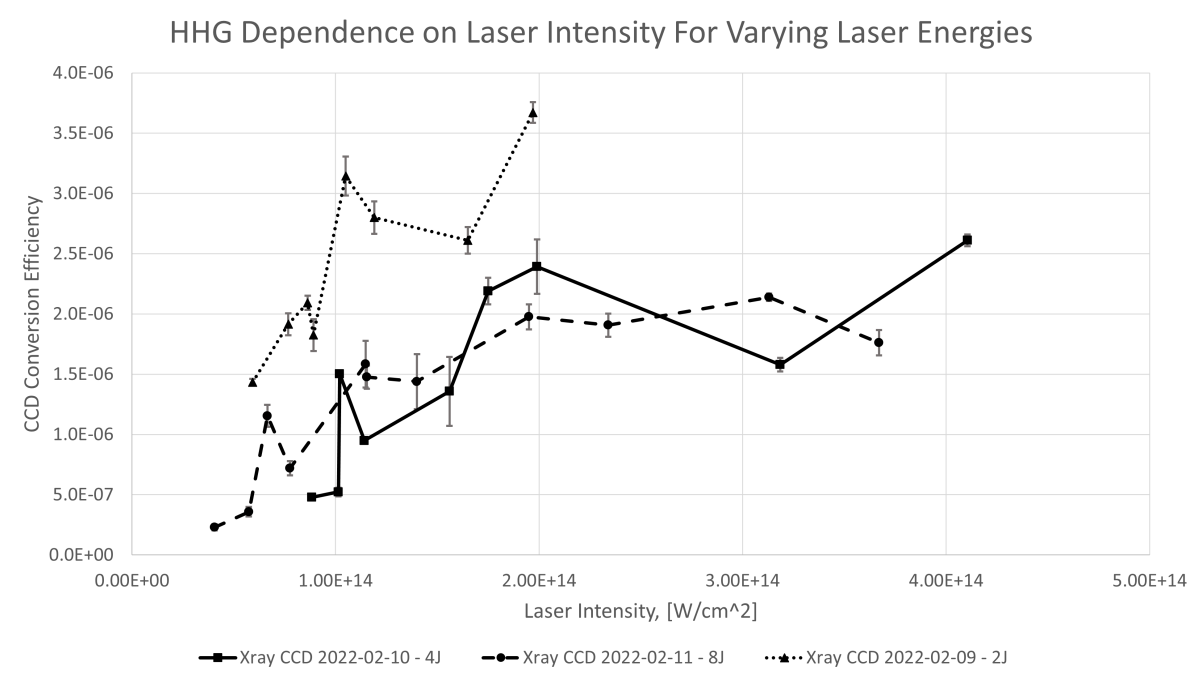

Figure 4.62: Conversion efficiency as a function of laser intensity for the three longitudinal scans shown in figure 4.58. The solid line is the CCD measurement from 2022-02-10 at 4J, the dashed line is the CCD measurement from 2022-02-11 at 8J, and the dotted line is the CCD measurement from 2022-02-09 at 2J. [2022-02-09, Shots 93-131, 2 J, 1400 fs^2, Ave 59.2 fs, Ave $1.1 \times 10^{14} W/cm^2$, Argon, 31 bar, 22 ms, 6 mm, Varying, 8 mm, Mesh 2], [2022-02-10, Shots 129-147, 4 J, 800 fs^2, Ave 39 fs, Ave $1.8 \times 10^{14} W/cm^2$, Argon, 31 bar, 22 ms, 10 mm, Varying, 8 mm, Nothing], [2022-02-11, Shots 146-201, 8 J, 800 fs^2, Ave 55.6 fs, Ave $1.5 \times 10^{14} W/cm^2$, Argon, 36 bar, 22 ms, 10-14 mm scaled to 10 mm, Varying, 8 mm, Nothing]

The data from these scans can be combined to create a more accurate plot of HHG dependence on intensity. The data from 2022-02-09 is excluded from this however, since the scaling makes it less reliable. The result of combining the scans for 2022-02-10 and 2022-02-11 is shown in figure 4.63. The conversion efficiency appears to increase at a decreasing rate with intensity so a logarithmic line with equation $y = 9 \times 10^{-7} ln(x) - 3 \times 10^{-5}$ is fit to it. This behaviour is similar to what would be expected based on the results seen in figure 2.5.

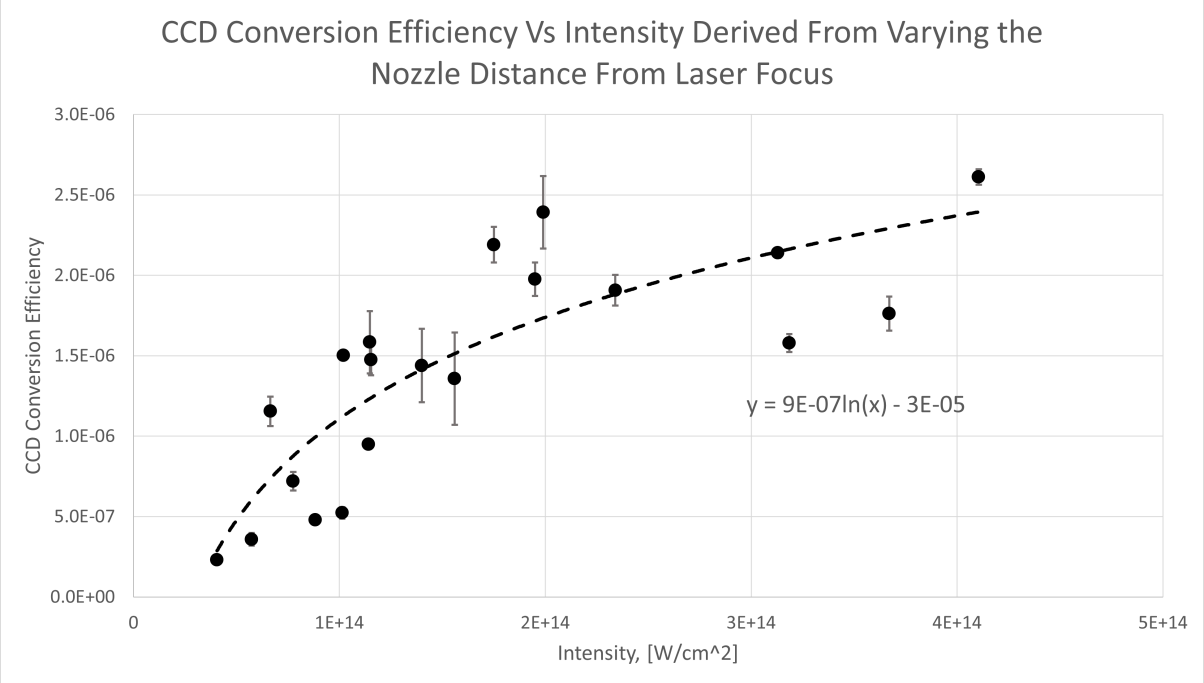

Figure 4.63: Conversion efficiency as a function of laser intensity for the three longitudinal scans shown in figure 4.58 combined together. The solid line is the data and the dashed line is a logarithmic fit to the data. [2022-02-10, Shots 129-147, 4 J, 800 fs^2, Ave 39 fs, Ave $1.8 \times 10^{14} W/cm^2$, Argon, 31 bar, 22 ms, 10 mm, Varying, 8 mm, Nothing], [2022-02-11, Shots 146-201, 8 J, 800 fs^2, Ave 55.6 fs, Ave $1.5 \times 10^{14} W/cm^2$, Argon, 36 bar, 22 ms, 10-14 mm scaled to 10 mm, Varying, 8 mm, Nothing]

4.9 Discussion

While spatial modulation of the laser beam introduced some error to the analysis, most diagnostics behaved as expected and provided reasonable data. The calculated wavelengths for the harmonics lined up well with the observed spectral results both in figures 4.16 and 4.17. While there is some deviation for some of the lineouts, as can be seen in figure 4.22, these differences are likely explained by the spatial modulation combined with the wide opening for the grating. At high laser energy and intensity the spectra shows that a bright line is generated as shown in figure 4.13. This line appears to be the result of a plasma with weak emission forming as it only appears at high laser energies / intensities. The spectra scales with intensity, allowing higher order harmonics to be accessed at higher laser intensities as shown in figure 4.20. However, this scaling with intensity, is not entirely accurate as is demonstrated by figure 4.21 which forms the plasma line despite only having a laser intensity of $1 \times 10^{14} W/cm^2$. From figure 4.20 the expected intensity for plasma formation should be closer to $1.5 \times 10^{14} W/cm^2$. The difference with figure 4.21 is that it was performed at a laser energy of 12 J rather than the 8 J that most of figure 4.20 is composed of. This indicates that the laser energy is having a disproportionate impact on the laser intensity. This may be a result of the spatial modulation separating the laser into bright spots which contain a disproportionate amount of laser energy therefore leading to plasma formation at high laser energies even

with lower overall intensity. The hot plasma spectra is also shown in 4.27 which shows a single line at 19 nm. This is similar in position to the bright line observed earlier lending credence to the belief that this is indeed a plasma.

When the plasma is not formed harmonics between the 19th and 35th harmonic are achieved. This is centered around the 27th and 25th harmonic with a centroid of 30.6 nm. Taking into account some of the absorption factors shifts the spectrum to lower harmonics (higher wavelengths) as shown in figure 4.23. The spectrum moves to be centered around the 25th and 23rd harmonic (wavelengths of 31.8 and 34.6 nm). When the plasma line is formed it extends the harmonic spectrum providing harmonics between the 21st and the 45th (wavelengths of 37.8 and 17.6 nm). The shape of the adjusted spectra suggests that the plateau region runs to around the 27th harmonic before reaching cutoff and falling off. The fall off of intensity for lower order harmonics may be attributed to absorption effects, but there should be no absorption for the higher harmonics indicating that this is indeed the cutoff region. The variation of the highest order harmonic with intensity (before the plasma line) also suggests that this is the cutoff region.

The knife edge can also be used to verify the spectrum. Knife edge lineouts had an average of 34.1 nm which lines up well with the observed spectra. Beyond that the knife edge can provide estimates of spot size leading to an upper limit size of 355 um. The effect of diffraction increases the length of the knife edge gradient therefore making the spot size estimate larger than the actual size. Matching calculated knife edge lineouts to measured one,s as shown in figure 4.35, shows that the actual size may be between 100-250 um although it could still possibly be lower. Since the size of the beam at the nozzle varies between 22 mm and 4.4 mm, these values are much lower than the possible beam size at the nozzle which indicates that the observed XUV is focusing as expected. Looking at the blurring across a knife edge from a full plasma, as shown in figure 4.36, provides an average spot size measurement of 3.4 mm for a 4.4 mm beam at the nozzle. While this is still somewhat smaller, it is obviously much closer to the actual beam size than the XUV from the HHG.

The shadowgraphic imaging on the perforated mesh can be used to determine both the distance from CCD to the XUV source as well as give another estimate of spot size. Figures 4.41 and 4.40 show the measured distance to the XUV source for varying the nozzle distance to laser focus. Figure 4.40 in particular shows that there is no significant change to the measured distance to the XUV source as the nozzles moves further from laser focus. If there had been change, the source of the XUV would be at the nozzle position but no change supports the idea that the XUV light is being focused down to laser focus resulting in the XUV source being at laser focus. Using ray tracing simulations allows for an estimate of the spot size when comparing to the blurring of the mesh hole. Figures 4.42 and 4.43 show that the closest estimate for the spot size is about 500 um,

higher than the 355 um estimate from the knife edge measurement, but still significantly below the beam size. This difference may be due to error and diffraction effects along the mesh.

The step wedge demonstrates that the XUV is attenuated by the aluminum filter which acts as another verification that the observed radiation is XUV.

Based on the spectral results from the grating, the knife edge, and the step wedge it is reasonable to conclude that XUV light is being generated and that XUV is coming from HHG. It can also be concluded from the knife edge measurements of spot size and the shadowgraphic mesh measurements of XUV source position and spot size that the XUV light is focusing rather than occuring at the interaction point between the beam and the gas jet.

With this established it is useful to know how the conversion efficiency scales with varying parameters. From the 3D simulations it was determined that the line integrated isothermal pressure was between 21 and 217 mm-mbar, mostly above the desired 37.5 mm-mbar predicted by Nayak [11]. Nayaks result predicts a peak conversion efficiency at 37.5 mm-mbar but the measured data continues to increase as the line integrated isothermal pressure increases. However, Nayaks result uses the standard HHG geometry with the gas jet constrained to the beam waist region which experiences large changes in laser intensity. In the FCHHG geometry the laser intensity changes at a much slower rate compared to the standard geometry. Because of this, the intensity within the last 37.5 mm-mbar of the gas jet will remain mostly unchanged from the intensity at the start of the gas jet. This means that the last 37.5 mm-mbar will become the effective line integrated isothermal pressure interaction region. This potentially allows for optimal conditions to be achieved regardless of backing pressure as long as the line integrated isothermal pressure is greater than or equal to 37.5 mm-mbar. Prior to this last 37.5 mm-mbar most of the XUV will be absorbed but some XUV may survive absorption leading to the continual increase observed with increasing backing pressure. Another explanation is that the optimal condition for the FCHHG geometry is different than the 37.5 mm-mbar of the standard HHG geometry. This may be the case as equation 2.14 and papers [8,25-27] indicate that the phase matching conditions are significantly different for the FCHHG. The Guoy phase shift is almost completely negligible for FCHHG but the dipole phase shift is much more significant due to variations in intensity. It is perhaps these changes which lead to a higher optimal pressure-distance product for FCHHG. Detailed simulations of the FCHHG process need to be carried out in order to reach conclusions on this result.

Moving the nozzle away from the laser axis provides a plot with an initial fall off, followed by a slowly decreasing plateau, and then a more sharp fall off as shown in figure 4.52. These fluctuations show how the beam is being affected by modulations in the

density of the gas jet. Moving the nozzle away from laser focus is much less affected by density modulations since this movement directly affects the intensity of the beam at the gas jet. This is shown in figure 4.58 and shows that higher laser energies are able to achieve higher conversion efficiencies when the laser is further from focus. Taking this data and plotting in terms of intensity provides figure 4.63 which shows conversion efficiency increasing at a decreasing rate with laser intensity. Comparing this to figure 2.5 shows a similar trend of increasing at a decreasing rate with laser intensity indicating that the results achieved during this experiment line up with the expected behaviour.

The difference between calculated intensity and dazzler setting shown in figure 4.60 indicates that there may be a difference between the measured pulse length on the autocorrelator and the actual pulse length inside the chamber since the peak conversion efficiency should really be at the peak intensity.

Conversion efficiencies varying from 1×10^{-7} to 3×10^{-6} are observed for varying different shots. Concentrating on a single bright spot, such as in figure 4.50, provides conversion efficiencies up to 1.1×10^{-5}. This is not bad in terms of conversion efficiency but for comparison Nayak [11] obtained conversion efficiencies of 3×10^{-4} for the 11th, 13th, and 15th harmonics of argon. These are very high conversion efficiencies achieved in a highly optimized setup.

Overall, the laser intensity for HHG is believable and the conversion efficiencies are also believable. Parameters such as backing pressure, nozzle distance from laser axis, and nozzle distance from laser focus are all affected by the integrated isothermal pressure as predicted by the 3D simulation of the gas jet.

Chapter 5

Conclusions and Future Work

5.1 Conclusions

There were two main goals of the FCHHG experiment at the CLPU. The first was to demonstrate that the FCHHG geometry was capable of generating high-order harmonics in a manner consistent with other HHG experiments allowing scaling to higher output energies. The second goal was to determine whether these harmonics retained the focusing behaviour of the original beam.

Based on the spectral characterization data, it is clear that high order harmonics were created. These harmonics reached up to the 35th harmonic, with cutoff beginning after the 27th harmonic, but were extended to the 45th harmonic when plasma formation occurred. In many of the images clear peaks are easily distinguishable and in most of these images the peaks line up well with the calculated harmonics. In addition, the spectral characterization of diffraction from the knife edge measurements were consistent with radiation in the XUV wavelength range of the harmonic emission. The step wedge also demonstrated that the radiation observed on the CCD was attenuated by the aluminum filters confirming again that radiation in the XUV range was being generated.

The knife edge is used again for the determination of XUV spot size. Blurring of the knife edge images can be due to a combination of both the diffraction and the spatial size of the high harmonic hot spot that was created at laser focus. This provides an estimated spot size between 100-250 um for a laser beam diameter at the nozzle of 7.9 mm. When deliberately creating a plasma this measurement was a spot size of 3.4 mm for a laser beam diameter of 4.4 mm. The small spot size demonstrates that the XUV is indeed focusing as expected. Additionally, the effects of knife edge diffraction would be completely washed out for large spot sizes, so even observing the diffraction pattern verifies that the light is coming from a tightly focused source.

The existence of a focused high harmonic beam which then diverges after focus was

further verified by analysis of the shadowgraphic imaging of the perforated meshes. These meshes indicated a source size of less than 500 um, much smaller than the laser beam diameter, and also indicated that the focal spot of the XUV beam was in the region of the laser focal spot. Moving the nozzle in relation to laser focus did not cause the focal spot of the XUV beam to change which clearly shows that the XUV beam is not diverging from the nozzle position and is instead focusing down before diverging.

Analysis of the data has therefore demonstrated that high harmonic generation is occuring and that it is focusing into a high harmonic hot spot as expected.

Previous publications have indicated that an integrated isothermal pressure for an argon gas jet of the order of 37.5 mm-mbar would lead to the highest efficiency harmonic generation. [11] A supersonic rectangular nozzle was designed and modeled with 2D and 3D gas flow simulations in order to provide a large cross-sectional area of up to 20 mm in diameter. Interferometric analysis of the gas jet was used to scale the gas flow simulations which then allowed for the simulations to be applied to the CLPU data. Taking the integrated isothermal pressure along the beam path through the nozzle provided values ranging between 21 and 217 mm-mbar for varying backing pressure. Analysis of the scaling of HHG with increasing integrated isothermal pressure of the gas jet showed that conversion efficiency increased as the integrated isothermal pressure increased, which is in conflict with the predicted behaviour of a peak at 37.5 mm-mbar. This suggests that the FCHHG geometry may behave differently than the standard HHG geometry in this respect, or that absorption within the gas jet leads to the effective integrated isothermal pressure being much smaller than recorded.

The scaling of HHG with laser intensity was investigated by varying three different parameters: laser energy, laser pulsewidth, and beam diameter at the gas jet. Due to spatial modulation and uncertainty in the accuracy of the pulse width measurement there is some inaccuracy in the calculated intensity but it may still be used as an estimate of intensity. The conversion efficiency increases at a decreasing rate with increasing laser intensity. The trend of the conversion efficiency is similar to what is observed from previous research for these intensities. [16]

The final important variable to discuss is the conversion efficiencies achieved. Conversion efficiencies of up to 3×10^{-7} for the XUV diode and 3×10^{-6} for the CCD were achieved. Focusing on the bright spots on the CCD achieves conversion efficiencies of up to 1×10^{-5}. These are within the expected range for conversion efficiency of HHG but are below the optimal case of 10^{-4} for argon [11].

5.2 Future Work

The experiment at the CLPU was very successful in that it showed that the FCHHG geometry could work, however there are a number of issues and questions which remain and a number of improvements which could be made to improve the final conversion efficiency. Beam quality was a major issue during the experiment. The HHG was highly sensitive to spatial modulation in the driving laser which made it difficult to carry out both spatial and spectral characterization and led to differences between the measurements of CCD and XUV diode conversion efficiencies. Future experiments should ideally be conducted with a much more uniform beam so as to achieve greater accuracy in the results and a higher overall conversion efficiency. The spectral measurements could also be improved by making use of a dedicated spectrometer rather than placing a grating in front of the CCD. The grating worked well but had poor resolution making it difficult to distinguish between peaks at times, and the position of the grating relative to the CCD had a higher degree of uncertainty than would be desirable. It would also be useful to create a detailed computer model of the FCHHG process. While it is similar to traditional HHG, the effects of phase matching are different for the case of a converging beam and so it would be useful to create a proper model to investigate these differences and predict the theoretical behaviour.

Beyond what was shown in this thesis, an attempt was made during the CLPU experiment to characterize the focusing behaviour of the XUV through an ablation test. This was done by placing a glass target at laser focus with a sacrificial aluminum foil between it and the nozzle. The idea was that the foil would be destroyed but would succeed in blocking the visible light allowing only the XUV to pass and ablate the target. Unfortunately, the foil was not completely effective and on some of the shots the light was able to pass through anyway. The foil also ended up being coated onto the target making any ablation difficult to distinguish. This points to a more fundamental problem: how to separate the XUV from the visible light before the laser is focused. In order for HHG to occur the laser must be at intensities almost high enough to ionize gas, and since any separation would occur after the nozzle the intensity would only be higher there and capable of ablating any solid placed in the beam path. If the XUV is not able to be separated from the laser before focus then the FCHHG process would be less valuable as the main purpose of it is to create a high energy XUV hot spot without a high intensity laser beam.

There are a few different solutions to this problem. One solution would be to use sacrificial gratings to spatially separate the different wavelengths. This could be done using inexpensive sacrificial gratings which can be produced by laser ablation. [45] Another possible route would be to create a plasma mirror tuned to allow XUV to pass but reflect the visible light. Non-collinear high harmonic generation may also be able to be used.

This process involves using two beams convering onto the gas jet at different angles to create HHG which then moves out at an angle in between the angles of the two beams. Since the movement of the electron in HHG can be estimated using a semi-classical model the fields of the two beams work together to move the electron at an angle between the two beams. This method has been shown to work in standard HHG experiments [46] but the FCHHG geometry may not work with this method. Alternatively, the XUV could be separated after laser focus when the intensity is low enough to do so and a focusing mirror could be used to refocus the beam but this would require a large vacuum chamber and additional XUV focusing optics. Future work should be done to determine an effective method of separation.

Lastly, conversion efficiency can be considerably improved. The results of Nayak [11] indicates that under optimum intraction and phase matching conditions conversion efficiencies of a few times 10^{-4} are achievable for argon and slightly higher for xenon. Further study will be required to achieve such optimal conditions for the FCHHG. If such efficiencies are achieved in the FCHHG geometry and used for Petawatt laser pulses with energy of 30 J, high harmonic pulses of several mJ should be achievable. If an effective method of separating the laser from the XUV is developed then the FCHHG method will be capable of generating high intensity XUV pulses.

References

[1] J. Rothhardt et.al. “Table-top nanoscale coherent imaging with XUV light,” Journal of Optics Vol 20, 113001 (2018).

[2] R. L. Sandberg et.al. “Lensless Diffractive Imaging Using Tabletop Coherent High-Harmonic Soft-X-Ray Beams,” Physical Review Letters Vol. 99, 098103 (2007).

[3] J. Schwenke et.al. “Single-shot holography using high-order harmonics,” Journal of Modern Optics Vol. 55, No. 16, pp. 2723-2730 (2008).

[4] C.W. Gwyn, R. Stulen, D. Sweeney, et. al., “Extreme ultraviolet lithography,” Journal of Vacuum Science & Technology B: Microelectronics and Nanometer Structures Procesing, Measurement, and Phenomena Vol 16, pp. 3142-3149 (1998).

[5] B. Wu and A. Kumar, “Extreme ultraviolet lithography: A review,” Journal of Vacuum Science & Technology B: Microelectronics and Nanometer Structures Procesing, Measurement, and Phenomena Vol 25, pp. 1743-1761 (2007).

[6] T. T. Luu, M. Garg, S. Yu. Kruchinin, A. Moulet, M. Th. Hassan, and E. Goulielmakis, “Extreme Ultraviolet high-harmonic spectroscopy of solids”, Nature, Vol 521, pp. 498 - 502 (2015).

[7] S. Ghimire and D. A. Reis, “High-harmonic generation from solids”, Nature Physics, vol 15, pp. 10 - 16 (2019).

[8] C. M. Heyl et.al, “Introduction to macroscopic power scaling principles for high-order harmonic generation,” Journal of Physics B: Atomic, Molecular and Optical Physics Vol 50, 013001 (2017). Images used with permission through Creative Commons Attribution 3.0 license: https://creativecommons.org/licenses/by/3.0/

[9] Ch. Spielmann, et.al. “Generation of Coherent X-rays in the Water Window Using 5-Femtosecond Laser Pulses,” Science Vol. 278, (1997)

[10] Z. Chang, et.al. “Generation of Coherent Soft X Rays at 2.7 nm Using High Harmonics,” Physical Review Letters Vol. 79, No. 16, pp. 2967-2970. (1997)

[11] A. Nayak et.al. “Multiple ionization of argon via multi-XUV-photon absorption induced by 20-GW high-order harmonic laser pulses,” Physical Review A Vol 98, 023426, (2018). Images used with permission from APS.

[12] M. Fox, “Nonlinear Optics,” in Optical Properties of Solids. Oxford University Press, Second Edition, New York, United States of America: 2010, ch. 11, pp. 295 - 321.

[13] R. W. Boyd, “Nonlinear Optics,” Elsevier, Third Edition, Burlington, United States of America: 2008.

[14] C. Jin, “Introduction to High-Order Harmonic Generation,” Springer Theses, First Edition, Kansas State University, United States of America: 2013, Ch. 1, pp. 2.

[15] C. Winterfeldt, C. Spielmann, and G. Gerber, “Colloquium: Optimal control of high-harmonic generation,” Review of Modern Physics Vol 80, pp. 117-140, (2008). Images used with permission from APS.

[16] A. L’Huillier and Ph. Balcou, “High-Order Harmonic Generation in Rare Gases with a 1-ps 1053-nm Laser”, Physical Review Letters, Vol. 70, No. 6, pp. 774 - 777 (1993). Images used with permission from APS.

[17] S. Driever et. al. “Near infrared few-cycle pulses for high harmonic generation,” Journal of Physics B: Atomic, Molecular, and Optical Physics Vol 47, 204013, (2014).

[18] C.-G. Wahlstrom, et.al. “High-order harmonic generation in rare gases with an intense short-pulse laser,” Physical Review A. Vol. 48, No. 6. pp. 4709-4720 (1993). Images used with permission from APS.

[19] A.V. Smith, “Phase Matching,” Nonlinear Optics, Applications, 153-163 (2005). Image used with permission from Elsevier.

[20] P. Salieres, A. L’Huillier, M. Lewenstein. “Coherence Control of High-Order Harmonics,” Physical Review Letters Vol. 74, No. 19. pp. 3776-3779 (1995)

[21] M. B. Gaarde, et.al. “Spatiotemporal separation of high harmonic radiation into two quantum path components,” Physical Review A. Vol 49, No. 2. pp. 1367-1373 (1999).

[22] Center for X-ray Optics, "Filter Transmission," Accessed: 2022. [Online] Available: https://henke.lbl.gov/optical_constants/filter2.html

[23] L. B. Elouga Bo, et.al. "Mutli-μJ coherent extreme ultraviolet source generated from carbon using the plasma harmonic method," Vol 19, No. 4, (2010).

[24] J. Series, et.al. "Coherent superposition of laser-driven soft-X-ray harmonics from successive sources," Nature Physics Vol 3, pp. 878-883, (2007).

[25] Y. Tao, et.al. "Temporal model for quasi-phase matching in high-order harmonic generation," Optics Express Vol 25, Issue 4, pp.3621-3683, (2017).

[26] E. Constant, et.al. "Optimizing High Harmonic Generation in Absorbing Gases: Model and Experiment," Physical Review Letters Vol 82, pp. 1668 - 1671, (1999).

[27] K. Midorikawa, Y. Nabekawa, A. Suda, "Review: XUV multiphoton processes with intense high-order harmonics," Progress in Quantum Electronics Vol 32, Issue 2, pp. 43-88, (2008).

[28] NASA, "Compressible Area Ratio," Edited: 2021, Accessed: 2022. [Online] Available: https://www.grc.nasa.gov/www/k-12/airplane/astar.html

[29] J. C. Crown and W. H. Heybey, "Supersonic Nozzle Design," Naval Ordnance Laboratory Memorandum 10594, (1950)

[30] K. Schmid, "Supersonic Micro-Jets And Their Application to Few-Cycle Laser-Driven Electron Acceleration," Ph.D. Dissertation, Fakultat fur Physik, Ludwig-Maximilians-Universitat, Munchen, Germany, 2009.

[31] A. Sasoh, "Compressible Fluid Dynamics and Shock Waves," Springer, First Edition, Singapore, Ch 7, pp. 143-144.

[32] Nasa, "Flow Past A Wedge," Edited: 13 May, 2021, Accessed: 2022. [Online] Available: https://www.grc.nasa.gov/www/k-12/airplane/wdgflow.html

[33] I. M. Hall, "Inversion of the Prandtl-Meyer relation," The Aeronautical Journal Vol 79, Issue 777, pp. 417-418. (1975).

[34] Ansys, Academic Research Fluent, Version 2020 R2.

[35] S. Lorenz, et.al. "Characterization of supersonic and subsonic gas targets for laser wakefield electron acceleration experiments," Matter and Radiation at Extremes Vol 4, 015401, (2019).

[36] J. Nejdl, et.al. "Imaging Michelson interferometer for a low-density gas jet characterization," Review of Scientific Instruments Vol 90, 065107, (2019).

[37] Big Sky Laser Technologies Inc., Ultra CFR Nd:YAG Laser System User's Manual, Rev. D, (1999). [Online] Available: http://www.ece.ualberta.ca/∼lpfs/uploads/new/BigSky_Ultra-CFR_Manual.pdf

[38] M. Takeda, H. Ina, S. Kobayashi, "Fourier-transform method of fringe-pattern analysis for computer-based topography and interferometry," J. Opt. Soc. Am. Vol. 72, No. 1, (1982).

[39] OSI Optoelectronics, XUV 100 Datasheet, [Online] Available: https://www.osioptoelectronics.com/standard-products/silicon-photodiodes/x-ray-radiation-detectors/soft-x-ray-far-uv-enhanced-photodiodes.aspx

[40] Teledyne Princeton Instruments, "Sophia Ultra-Low-Noise CCD Cameras," Accessed: 2022. [Online] Available: https://www.princetoninstruments.com/products/sophia-family/sophia

[41] Hamamatsu, Solar blind photomultiplier R2078. [Online] Available: https://www.hamamatsu.com/content/dam/hamamatsu-photonics/sites/documents/99_SALES_LIBRARY/etd/R2078_TPMH1226E.pdf

[42] F. A. Jenkins, H. E. White, "Fundamentals of Optics," McGraw-Hill Primls Custom Publishing, Fourth Edition, Ch 18, (2001).

[43] RS Pro, "Lamina metalica RS PRO, long. 500mm, anch. 500mm, grosor 0.6mm," (2022) [Online] Available: https://docs.rs-online.com/0e59/0900766b81580073.pdf

[44] Zemax, Optic Studio Professional, Version 20.3.2.

[45] K. Ilcisin and R. Fedosejevs, "Direct production of gratings on plastic substrates using 248-nm KrF laser radiation," Applied Optics. Vol. 26, Issue 2, pp. 396-400 (1987).

[46] A. Ozawa, et.al. "Non-collinear high harmonic generation: a promising outcoupling method for cavity-assisted XUV generation," Optics Express. Vol. 16, No. 9, pp. 6233-6239 (2008).

[47] C. D. Argyropoulos, N. C. Markatos, "Recent advances on the numerical modelling of turbulent flows," Applied Mathematical Modelling. Vol. 39, pp. 693-732 (2015).

Appendices

Appendix 1 - Fluent Setup

Ansys: Fluent was used for the gas jet simulations. [34] In order to run a simulation in Fluent the geometry of the object must first be designed in the program ANSYS: Spaceclaim. Spaceclaim allows for files to be imported into it so the curve design from MATLAB was simply included this way. After this the user needs to create an appropriate mesh for their object. This mesh is then imported into Fluent where the user can setup the simulation that they wish to solve for. A post-processor allows for the analysis of the simulation upon completion.

Mesh Design

The Mesh designer in Ansys has a multitude of options, however a fairly simple mesh was all that was needed for these simulations. The large "chamber" area at exit had its mesh set with a "Face Sizing" method. This allows the software to create a disorganized mesh out of objects with a size that the user can specify. These objects can be rectangles, triangles or other depending on how the software decides to create them. This choice is best because the flow in this region is not necessarily in a predictable direction so the mesh allows for greater freedom.

Within the nozzle itself a "Face Meshing" option was chosen. This method creates a mapped mesh which moves smoothly from the inlet to the outlet taking into account the curvature of the nozzle as seen in figure 5.1. This mesh is best here due to its structure matching the nozzle shape. It allows the fluid to flow without confusing Fluent.

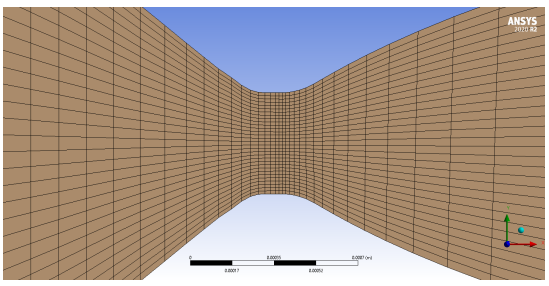

Figure 5.1: Face Meshing in Fluent

Solver Setup

Upon starting Fluent the first choice to make is whether to use the pressure based or density based solver.

The pressure based solver solves using the projection method. In this the pressure equation is derived in such a way that when it is used to correct the velocity of the system it satisfies the continuity equation. There are two ways that the pressure based solver can solve the system of equations: segregated or coupled. In the segregated solver velocity is solved for first and then corrected by solving for pressure and the continuity equation and then applying a correction to the velocity so that the continuity equation is satisfied. After this mass flux, pressure, and velocity are all updated and the energy, species, turbulence, and other scalar equations are solved for. Alternatively, in the coupled solver, the momentum and pressure based continuity equations are solved simultaneously after which the mass flux is updated and the scalar equations are solved for. The speed of solution convergence is much faster under the coupled solver, with the downside being that it takes up approximately twice as much memory.

The density based solver solves the coupled continuity, momentum, energy, and species transport equations and then goes on to solve turbulence and other equations before updating the solution and running through again until the solution is converged. The discrete non-linear equations for continuity, momentum, energy, and species transport are linearized using either an implicit or explicit method to produce the coupled system of equations which can be solved. The implicit method computes the unknown value in a cell using a relation that includes existing and unknown values from neighbour cells. The unknown value for each cell will therefore appear in the equation for itself and its neighbours and so the equations for every cell can then be solved simultaneously for the unknown values. The explicit method computes the unknown value of a cell using a relation that only includes existing values and not unknown values. Therefore each cell can be computed separately.

Originally the pressure based solver was designed for incompressible and mildly compressible flows while the density based solver was made for high-speed compressible flows. Over time both solvers have been improved to work with a variety of flows however the density based solver is more applicable to supersonic nozzle design such as what is done in this thesis and so it was chosen. The implicit method was used since it makies the solution for each cell more dependent on the surrounding cells and it seemed to be the easiest to work with.

Models

The next choice to make is to decide what additional models you want to use. These include: Multiphase, Energy, Viscous, Radiation, Heat Exchanger, Species, Discrete Phase, Acoustics, Structure, and Potential/Li-ion Battery. The only ones of interest to us are the Energy and Viscous models. The energy model is a simple on or off. Since we are dealing with compressible flows the energy equation should be on as it will determine how the temperature of the gas changes as it is compressed.

There are many different models for viscosity which can be used, and each of them has its own individual options that can be turned on or off as well. Two models are of particular interest: the K-epsilon and the K-omega viscosity models. These both are

based on Reynolds-averaged Navier-Stokes (RANS) equations, a set of equations widely used in computational fluid dynamics due to being both accurate and requiring fewer computational resources than other methods. K-epsilon and K-omega are two-equation models within the set of RANS models. This means that they use the mean flow Navier-Stokes equations as well as two transport equations for two turbulence properties (whereas a one-equation model such as the Spalart-Allmaras model only has one transport equation for a single turbulence propety). [47]

The K-epsilon model is the most widely used and tested of two-equation models. It deals with turbulent shear flows well but is poor at dealing with adverse pressure gradients and separated flows. [47] The standard K-epsilon model can be improved by selecting the "realizable" or "RNG" options. The realizable option turns a constant C_μ into a variable based on an eddy-viscosity equation. This substantially improves performance in jets, mixing layers, channels, boundary laryers, and separated flows when compared to the standard model. [47] The RNG model computes a coefficient with a different equation which provides better predictions of recirculation length in separating flows. Additionally there are several options for "Near-Wall Treatment" which can help improve the quality of the model near walls. [47] Of these the "Enhanced Wall Treatment" options seems to work best.

The K-omega model is also widely used and considered succesfull. It has greater predictive accuracy near boundary layers, under strong adverse pressure gradients, and when applied to free-shear flows and separated flows. It is rather weak at predicting flows with free-stream boundaries though. [47] Increased predictive accuracy near boundary layers is particularly important when inside of the nozzle but it's failure to predict the gas jet once it exits the nozzle is undesirable.

Fortunately there is a model which combines the advantages of the K-epsilon and K-omega models known as the Shear Stress Transport (SST) model. This model employs K-omega methods when close to boundaries but uses K-epsilon when further away. A set of blending equations is used to make a smooth transition between the two models. [47] This model ended up being chosen due to its predictive accuracy.

Materials

The built in materials database was used to select the gas type to use. Once selected several properties can be edited. These are Density, Specific Heat, Thermal Conductivity, Viscosity, and Molecular Weight. Density was set to be variable, obeying the ideal-gas law, viscosity was also set to be variable obeying the Sutherland law, the rest were left as default constants.

After this, boundary conditions may be set, the simulation can be initialized, and the calculation begun. Initialization was set so that there was a low vacuum everywhere prior to the gas flow beginning.

Appendix 2 - Error Introduced Into the Nozzle

After the experiment at the CLPU had concluded it was found that one of the sides of the nozzle had been slightly pushed upwards by the high pressure gas. After examination it was found that this occurred during some of the initial interferometry tests (discussed in a later section) and had therefore been present for the entire experiment. These interferograms are shown in figure 5.2, on the left is the picture before testing while on the right is the picture after testing with pressures of up to 50 bar. One edge of the nozzle visibly raised in these pictures while the other remains the same. It is likely that some of the gas got underneath the edge of the nozzle causing it to lift slightly. Measurements show that the edge was raised approximately 0.35 mm.

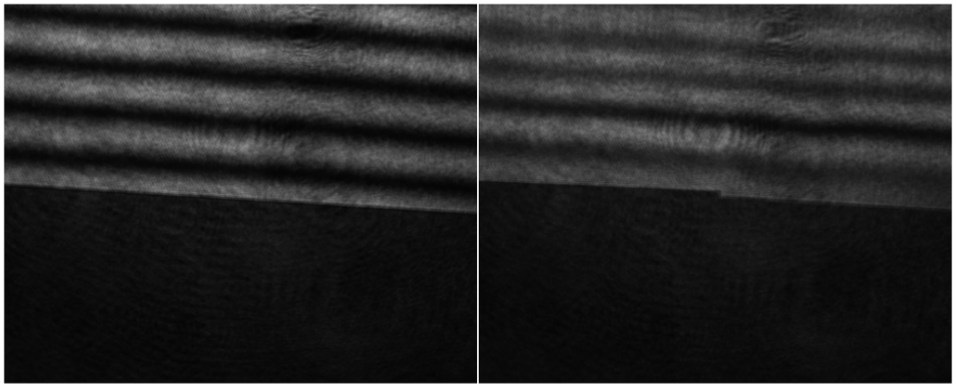

Figure 5.2: Interferograms showing the error introduced into the nozzle during the initial testing at the CLPU. On the left is before testing and on the right is after testing.

Simulations of this were run in fluent to better understand the effect that this might have on the overall gas density profile. The density contour plot for this is shown in figure 5.3, and the resulting on-axis and transverse lineouts are shown in figures 5.4 and 5.5 respectively. The Mach number plot in figure 5.4 shows that with the introduction of the error the nozzle no longer is able to reach Mach 1 by the end of the nozzle throat, although it is able to shortly afterward. In all four plots on this graph the effect of two large shocks are seen to disrupt the flow, although it recovers shortly afterward. Overall, even with the error, the on-axis properties of the nozzle are still roughly the same as the results without the error. The transverse plots show that the density profile is much more lopsided now. At the start the density is higher on the side without the error and there is a slight dip and then a peak on the side with the error. As distance from the nozzle increases though this peak on the error side becomes the highest density region and moves inward toward the center. Despite the lopsided nature of the plots the overall shape is the same and should not lead to any major issues for the CLPU experiment.

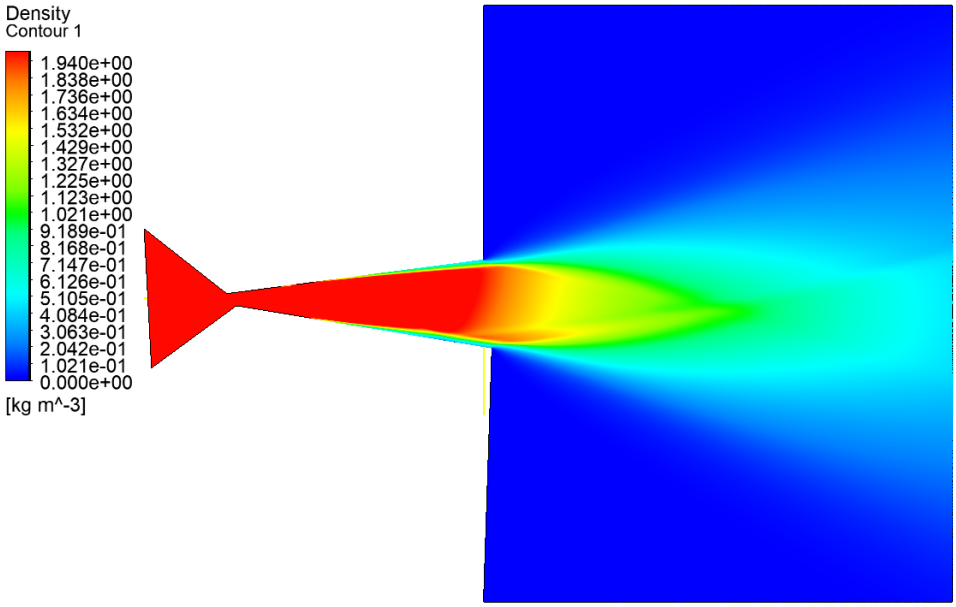

Figure 5.3: Density contour of the nozzle with error.

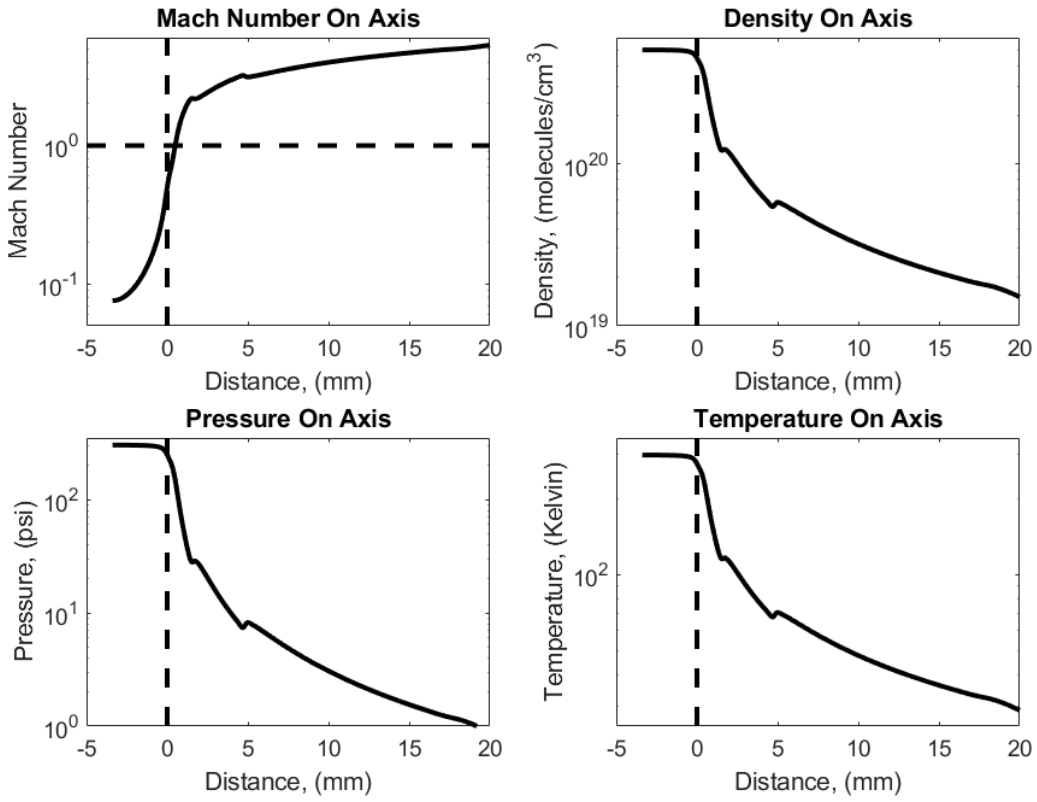

Figure 5.4: Logarithmic plots along the nozzle axis of Mach Number, Density, Pressure, and Temperature as a function of position relative to the nozzle throat. Vertical dashed lines represent the location of the nozzle throat while the horizontal dashed line in the Mach number plot represents Mach 1. For the nozzle with error.

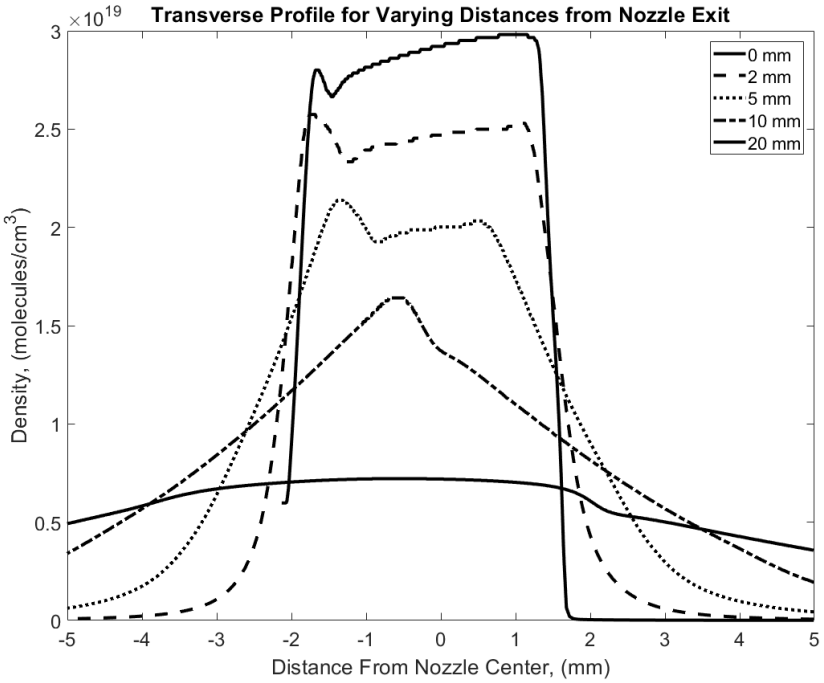

Figure 5.5: The first solid line with the larger peak is the 0 mm lineout, the dashed line is the lineout at 2mm, the dotted line is the lineout at 5 mm, the dotted and dashed line is the lineout at 10 mm, and the second broader solid line is the 20 mm lineout. For the nozzle with error.

Appendix 3 - Knife Edge Lineouts

Records of the locations where knife edge lineouts were taken are shown in figure 5.6.

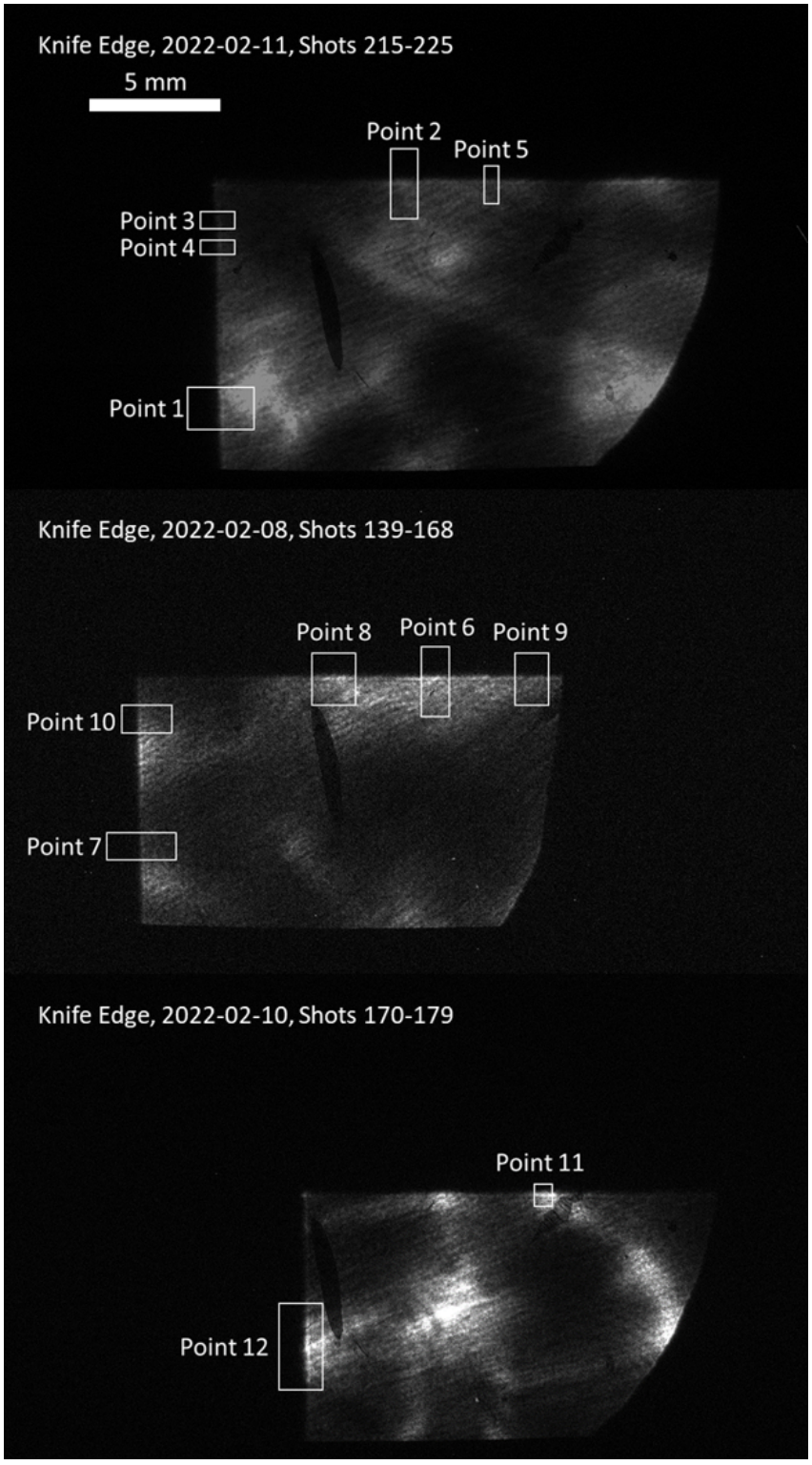

Figure 5.6: Picture of knife edge lineouts. [2022-02-08, Shots 139-168, 2 J, 1000 fs^2, Ave 77 fs, Ave $1.9 * 10^{14} W/cm^2$, Argon, 36 bar and 21 bar, 22 ms, 4 mm, 50 mm, 8 mm, Knife Edge], [2022-02-10, Shots 170-179, 4 J, 800 fs^2, Ave 44 fs, Ave $2.1 * 10^{14} W/cm^2$, Argon, 31 bar, 22 ms, 10 mm, 90 mm, 8 mm, Knife Edge], [2022-02-11, Shots 215-225, 8 J, 800 fs^2, Ave 57 fs, Ave $1.6 * 10^{14} W/cm^2$, Argon, 46 bar, 22 ms, 8 mm, 130 mm, 8 mm, Knife Edge]

Appendix 4 - Shadowgraphic Mesh Hole Size Measurement

Measurements showing the mesh hole sizes are shown in figure 5.7. From this a hole size of 1.1 mm is derived.

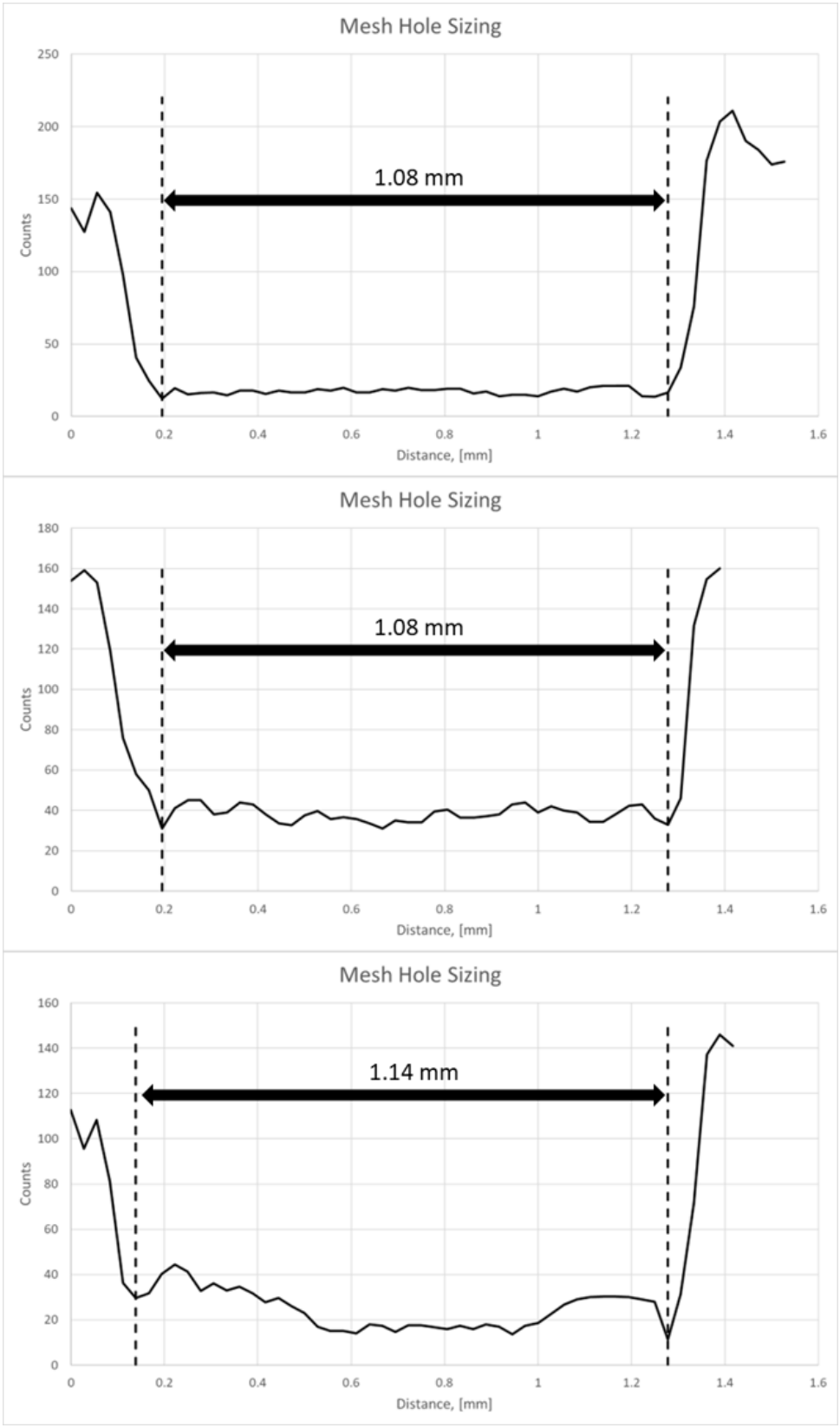

Figure 5.7: Mesh hole size measurements.

Appendix 5 - Comparison of XUV Diode 2 and Other XUV Diode Measurements

XUV diode 1 and 3 were on a translation stage capable of being moved into the beam path. The readings from these diodes often were below the background reading due to damage to the filter allowing light leakage. Additionally, in order to measure with these diodes the CCD had to be obscured. Due to these factors they were not used in the analysis. A comparison of conversion efficiency between XUV diode 2 and XUV diodes 1 and 3 is shown in figure 5.8. Similar conversion efficiencies are achieved between the diodes but there is still a fair amount of variation. This is likely a result of spatial modulation in the beam.

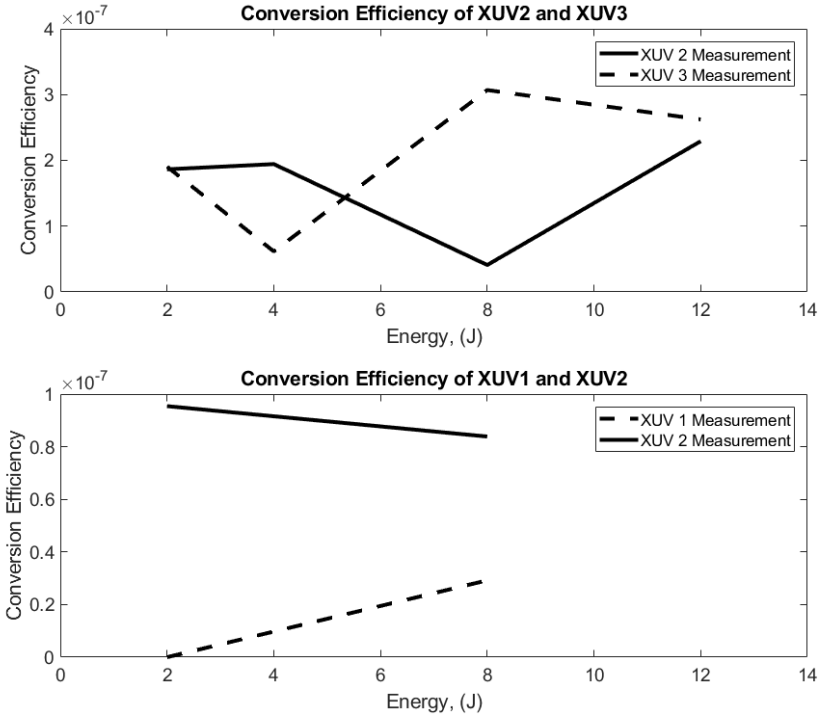

Figure 5.8: Comparison of XUV diode 2 (solid) and 3 (dashed) (top) and XUV diode 2 (solid) and 1 (dashed) (bottom). Data taken from a variety of different shots. [2022-02-09, Shots 160-162 and 166-168 and 172-174, 2 J, 1400 fs^2, Ave 51 fs, Ave $1.4 * 10^{14} W/cm^2$, Argon, 31 bar, 22 ms, 6 mm, 70 mm, 8 mm, XUV diode 1], [2022-02-10, Shots 62-66, 2 J, 800 fs^2, Missing Data, Assumed $1.6 * 10^{14} W/cm^2$, Argon, 31 bar, 22 ms, 6 mm, 70 mm, 8 mm, XUV diode 3], [2022-02-10, Shots 72-76, 4 J, 800 fs^2, Missing Data, Assumed $3.4 * 10^{14} W/cm^2$, Argon, 31 bar, 22 ms, 6 mm, 70 mm, 8 mm, XUV diode 3], [2022-02-11, Shots 259-262, 268-272, 12 J, 1000 fs^2, 91 fs, Ave $8.7 * 10^{13} W/cm^2$, Argon, 46 bar, 22 ms, 10 mm, 160 mm, 8 mm, XUV diode 3], [2022-02-17, Shots 141-145, 8 J, 1000 fs^2, 66 fs, Ave $1.4 * 10^{14} W/cm^2$, Argon, 46 bar, 22 ms, 8 mm, 130 mm, 8 mm, XUV diode 3], [2022-02-17, Shots 156-165, 8 J, 1000 fs^2, 54 fs, Ave $1.5 * 10^{14} W/cm^2$, Argon, 46 bar, 22 ms, 8 mm, 130 mm, 8 mm, XUV diode 1]

Appendix 6 - Intensity Sample Calculation

A sample calculation showing the method by which intensity of the beam was calculated. Starting with the recorded motor position of the nozzle $x_{motor} = 120mm$, the laser energy E = 8J, and the laser pulse-length $L_{pulse} = 60fs$. Other known values are the beam radius before focus $r_{unfocused} = 110$mm, the focal length F = 2500mm, and the maximum motor distance from the nozzle $x_{max} = 250$mm.

Convert pulse-length from fs to s by multiplying by 10^{-15}.

$$L_{pulse} = 60fs * 10^{-15}\frac{s}{fs} = 6 * 10^{-14}s$$

Determine the beam focusing half angle.

$$\phi = tan^{-1}(\frac{r_{unfocused}}{F}) = tan^{-1}(\frac{110mm}{2500mm}) = 0.044radians = 2.52^{\circ}$$

Use the angle to find the beam radius at the nozzle.

$$r_{nozzle} = tan(\phi) * (x_{max} - x_{motor}) = tan(2.52^{\circ}) * (250mm - 120mm) = 5.72mm$$

Calculate the power using the energy and the pulse-length.

$$P = \frac{E}{L_{pulse}} = \frac{8J}{6 * 10^{-14}s} = 1.3 * 10^{14}W$$

Using the power and the beam radius the intensity at the nozzle can be found.

$$I_{nozzle} = \frac{P}{(\pi r_{nozzle}^2)} = \frac{1.3 * 10^{14}W}{(\pi(0.572cm)^2)} = 1.2 * 10^{14}\frac{W}{cm^2}$$

Appendix 7 - XUV Diode Conversion Efficiency Sample Calculation

For a test shot the The average reading with background subtraction is 3.8 mV, the photodiode connection to the oscilloscope is terminated with a 1 MΩ resistor, the RC time constant is 6 ms, the Al filter thickness is 1.6um, the shot energy is 4J, and the active area of the photodiode is 1 cm^2.

First the voltage reading is converted to current by dividing by the 1 MΩ resistance.

$$I = \frac{V}{R} = \frac{3.8mV}{1M\Omega} = 3.8 * 10^{-9}A$$

Current is converted to charge by multiplying by the RC time constant.

$$Q = I * \tau = 3.8 * 10^{-9}A * 6ms = 2.28 * 10^{-11}C$$

The charge per unit area is found by dividing the charge by the active area of 1 cm^2.

$$\frac{Q}{cm^2} = \frac{Q}{A} = \frac{2.28 * 10^{-11}C}{1cm^2} = 2.28 * 10^{-11}\frac{C}{cm^2}$$

With this the attenuation due to the Al filter of thickness d_{Al} can be accounted for.

$$\frac{Q}{cm^2} = \frac{Q}{cm^2} * 10^{d_{Al}} = 2.28 * 10^{-11}\frac{C}{cm^2} * 10^{1.6um} = 9.08 * 10^{-10}\frac{C}{cm^2}$$

The energy per unit area is then found from charge by using the conversion factor of $3.6\frac{J}{C}$.

$$\frac{J}{cm^2} = \frac{Q}{cm^2} * 3.6\frac{J}{C} = 9.08 * 10^{-10}\frac{C}{cm^2} * 3.6\frac{J}{C} = 3.27 * 10^{-9}\frac{J}{cm^2}$$

The energy per unit area for the full laser at the XUV diode (217 cm from laser focus) is found by:

$$\text{Beam energy per unit area} = \frac{4J}{(\pi * (tan(11cm/250cm) * 217cm)^2)} = 0.01384\frac{J}{cm^2}$$

The conversion efficiency is then: $3.27 * 10^{-9}\frac{\frac{J}{cm^2}}{0.01384\frac{J}{cm^2}} = 2.36 * 10^{-7}$

Appendix 8 - CCD Conversion Efficiency Sample Calculation

For a total count number of $1.455 * 10^7$ (with an assumed plasma contribution of 0.5 per pixel subtracted) achieved over an area on the CCD of $2.37cm^2$ and using a quantum efficiency of 0.6921, a gain of 0.7275 eh / count, and a total filter thickness of 3.6 um the calculation of conversion efficiency is as follows.

First counts are multiplied by the gain factor to give the number of electron hole pairs created.

$$e-h_{gain} = \text{counts * gain} = 1.455 * 10^7 * 0.7275\frac{e-h}{count} = 1.05 * 10^7 e-h$$

This result is then divided by the CCD area to obtain e-h pairs per area

$$\frac{e-h}{cm^2} = e-h_{gain} \text{ / CCD Area} = \frac{1.05 * 10^7 e-h}{2.37cm^2} = 4.47 * 10^6 \frac{e-h}{cm^2}$$

Electron hole pairs are then converted to Coulombs using the known value of $6.24 * 10^{18}\frac{e-h}{C}$

$$\text{Charge per unit area} = \frac{\frac{e-h}{cm^2}}{6.24 * 10^{18}\frac{e-h}{C}} = \frac{4.47 * 10^6 \frac{e-h}{cm^2}}{6.24 * 10^{18}\frac{e-h}{C}} = 7.16 * 10^{-13}\frac{C}{cm^2}$$

Silicon, the material used in the CCD, typically requires 3.6 eV to create an electron hole pair. This relates the energy of the laser to the charge on the CCD allowing a conversion from Coulombs to Joules. The quantum efficiency will affect this conversion of energy to electron holes so to account for it the 3.6 $\frac{eV}{e-h}$ is divided by the quantum efficiency.

$$\text{Conversion} = \frac{3.6\frac{eV}{e-h}}{QE} = \frac{3.6\frac{eV}{e-h}}{0.6921} = 5.20\frac{eV}{e-h} = 5.20\frac{J}{C}$$

The charge per unit area is then converted to energy per unit area.

$$\text{Energy per unit area} = \text{Charge per unit area * Conversion} = 7.16 * 10^{-13}\frac{C}{cm^2} * 5.20\frac{J}{C} = 3.72 * 10^{-12}\frac{J}{cm^2}$$

Scaling due to the presence of filters can then be applied (d_{Al} is the combined thickness of all aluminum filters between the beam and CCD in terms of μm.):

$$\text{Filter corrected energy per unit area} = \text{Energy per unit area * } 10^{d_{Al}} = (3.72 * 10^{-12}\frac{J}{cm^2}) *$$

$$10^{3.6} = 1.48 * 10^{-8} \frac{J}{cm^2}$$

The energy of the full beam at the CCD is determined from the beam geometry seen in figure 4.2 and the known distance from laser focus to the CCD of 3 m.

$$\text{Beam energy per unit area} = \frac{4J}{(\pi * (tan(11cm/250cm) * 300cm)^2)} = 0.0073 \frac{J}{cm^2}$$

Conversion efficiency is then the ratio of XUV to the full beam.

Conversion efficiency = Filter corrected energy per unit area / Beam energy per unit area

$$= \frac{1.48 * 10^{-8} \frac{J}{cm^2}}{0.0073 \frac{J}{cm^2}} = 2.03 * 10^{-6}$$

Appendix 9 - Knife Edge Wavelength Sample Calculation

Lineouts across the knife edge provide the distance in microns and the intensity at the position. An estimate for I_u is taken and the intensity scaled to this value. The distance is then adjusted so that the lineout crosses the y-axis at 25% of the value of I_u. The distance from this point to the initial peak (d_{peak}) is then found, for this example it is 188 um. The distance from the source to the knife edge is a = 1.79 m and the distance from the knife edge to the CCD is b = 1.21 m.

$$\lambda = \frac{(d_{peak})^2}{(1.2)^2} / \frac{b*(a+b)}{2*a} = \frac{(188um)^2}{(1.2)^2} / \frac{1.21*(1.79+1.21)}{2*1.79} = 24nm$$

Appendix 10 - Shadowgraphic Mesh Sample Calculation

The distance to light source is calculated by first measuring the distance between the centroid of two holes (distant from eachother when possible). For this example the measured distance is taken to be 19582 um and the number of holes between these two is 9. Mesh 2 is used which is 92.5 cm (925000 um) from the CCD.

The actual distance can be found based on the number of holes between the two measured holes and the separation of 1.67 mm between each hole.

$(N_{holes} - 1) * 1.67mm = (9 - 1) * 1.67mm = 13.36mm = 13360um$

The difference between the measured and actual separation is then found.

Diff = Measured - Actual = 19582 um - 13360 um = 6232 um

The angle of the XUV beam is then found using the known distance from mesh 2 to the CCD.

$$\phi = tan^{-1}(\frac{Diff/2}{d_{CCD}}) = tan^{-1}(\frac{6232um/2}{925000um}) = 0.0034radians = 0.193^{\circ}$$

The measured distance between the holes is then used alongside this angle to calculate the distance to the light source.

$$\frac{D_{measured}/2}{tan(\phi)} = \frac{19582um/2}{tan(0.193^{\circ})} = 2.9m$$

Appendix 11 - Simulated 3D Integrated Isothermal Pressure Calculations

2D slices of the 3D simulation are taken from the Fluent simulation and used to reconstruct the 3D model for density (ρ) in Matlab. While the density data from Fluent is initially in terms of kg/m^3 it is transformed into $molecules/cm^3$ upon import into Matlab. When integrating through the 3D gas jet the integrated density is found using the trapezoidal rule as outlined below:

$$\text{Integrated density} = (x_2 - x_1) * \frac{\rho_2 + \rho_1}{2}$$

The integrated density can then be transformed to integrated isothermal pressure. This is done using the ideal gas law and Avogadros number (6.022×10^{23} molecules/mol) to convert the density in terms of molecules/cm^3 into pressure. An temperature of 300 K is assumed for this calculation. The process for converting 1 mm*molecules/cm^3 of integrated density into integrated isothermal pressure is shown below:

$$1mm * \frac{molecules}{cm^3} * (\frac{1}{6.022 \times 10^{23} \frac{molecules}{mol}}) = 1.6 \times 10^{-24} mm * \frac{mol}{cm^3}$$

$$1.6 \times 10^{-24} mm * \frac{mol}{cm^3} * (1 \times 10^6 \frac{cm^3}{m^3}) = 1.6 \times 10^{-18} mm * \frac{mol}{m^3}$$

$$1.6 \times 10^{-18} mm * \frac{mol}{m^3} * 8.314 \frac{J}{molK} * 300K = 4.14 \times 10^{-15} mm * \frac{J}{m^3}$$

$$4.14 \times 10^{-15} mm * \frac{J}{m^3} = 4.14 \times 10^{-15} mm * Pa$$

$$4.14 \times 10^{-15} mm * Pa * 0.01 \frac{mbar}{Pa} = 4.14 \times 10^{-17} mm * mbar$$

$$4.14 \times 10^{-17} mm * mbar$$